Hybrid Aerial and Terrestrial Locomotion, and Implications for Avian Flight Evolution

Kevin Peterson

Electrical Engineering and Computer Sciences
University of California at Berkeley

Technical Report No. UCB/EECS-2013-195
http://www.eecs.berkeley.edu/Pubs/TechRpts/2013/EECS-2013-195.html

December 1, 2013

Hybrid Aerial and Terrestrial Locomotion, and Implications for Avian Flight Evolution

by

Kevin C. Peterson

A dissertation submitted in partial satisfaction of the
requirements for the degree of
Doctor of Philosophy

in

Electrical Engineering and Computer Sciences

in the

Graduate Division

of the

University of California, Berkeley

Committee in charge:

Professor Ronald S. Fearing, Chair
Professor Robert Dudley
Professor Claire Tomlin

Spring 2013

Hybrid Aerial and Terrestrial Locomotion, and Implications for Avian Flight Evolution

Abstract

Hybrid Aerial and Terrestrial Locomotion, and Implications for Avian Flight Evolution

by

Kevin C. Peterson

Doctor of Philosophy in Electrical Engineering and Computer Sciences

University of California, Berkeley

Professor Ronald S. Fearing, Chair

Recent advances in the development of meso-scale legged robots have enabled high performance over a variety of terrains. However, there are still many environments where terrestrial legged robots are limited. The addition of aerodynamic capabilities provides a method of further extending the performance of small mobile robots towards all-terrain mobility.

This dissertation presents the development of DASH+Wings and BOLT, two small hybrid legged and winged robots. DASH+Wings is a six-legged, two-winged robot capable of wing-assisted terrestrial running and controlled aerial descent. BOLT is a two-legged, four-winged robot capable of high-speed terrestrial running and sustained flight. While the dynamics of legged locomotion have been extensively studied, the interaction between legs and flapping wings during terrestrial locomotion is poorly understood. WingSLIP, an extension to the canonical SLIP model for understanding wing-assisted terrestrial locomotion, is introduced. Analysis of the leg/wing phasing and leg stiffnesses elucidates the interaction between the legs and wings. The model suggests the presence of passively stable gaits for high-speed wing-assisted terrestrial running. The dynamics of wing-assisted terrestrial locomotion for a quasi-static and dynamic gait are examined using BOLT with the addition of an on-board accelerometer and rate gyroscope. The flapping wings enable BOLT to run at over two ms^{-1} and take off in as little as one meter of space. In addition to flapping wings, the passive effects of aerodynamics on a high-speed legged robot (VelociRoACH) are also examined. Passive aerodynamic stabilization is shown to improve the performance and stability of the system. An examination of avian flight evolution is performed using DASH+Wings to examine the consequences of adding wings to a cursorial locomotor. We note that current support for the diverse theories of avian flight origins derive from limited fossil evidence, the adult behavior of extant flying birds, and developmental stages of already volant taxa. The addition of flapping wings increased the maximum horizontal running speed and the maximum terrestrial incline angle of ascent, along with decreasing the aerial descent angle. To better examine avian flight evolution, a scaled model of *Archaeopteryx* is developed, and the effects of flapping frequency and amplitude are examined through the use of wind tunnel measurements. The findings are discussed in the context of existing hypotheses for the origins of flapping flight in vertebrates.

To my parents,
for getting me here.

And to my grandparents,
for their love and support along the way.

Contents

List of Figures

List of Tables

Acknowledgments

This dissertation would not have been possible without the help of many people over the last six years. First and foremost, I would like to thank my advisor, Professor Ron Fearing. His constant support, encouragement, and stream of interesting ideas was truly remarkable. I am truly grateful to have had the opportunity to work and learn under his mentorship.

I was fortunate to join a great group in the Biomimetic Millisystems Lab – and am proud to call them both colleagues and friends. I was amazed when I first joined the lab at how Erik Steltz and Aaron Hoover always seemed to have a suggestion for or solution to every problem, regardless of the applicability to their own work. Along with Stan Baek and Jongho Lee, Erik and Aaron were also instrumental in the development of my ping pong skills. A great debt is owed to Paul Birkmeyer, whose DASH design enabled much of my research, and who was always willing to discuss ideas with me. I would be remiss if I didn't also thank Paul as a faithful doubles partner and bitter singles opponent in some epic ping pong series. Many thanks also go to Stan, Aaron, Fernando Garcia Bermudez and Andrew Pullin for all of their efforts making the ImageProc board such a useful platform. To Andrew Gillies and Brian Schubert, your patience for and willingness to help with topics that had no relation to your own work was always appreciated. Thanks to Nick Kohut for making sure my understanding of dynamics was passable, and providing some company during all of the late lab dinners these last months. I am grateful to Duncan Haldane for enabling me to work on such a remarkable platform as the VelociRoACH, and develop some truly interesting ideas with it. Finally to the other members of the lab: Austin Buchan, Jaakko Karras, Cameron Rose, and Ethan Schaler; I look forward to seeing the direction the lab takes with you in the future.

I am especially thankful for the assistance of Professor Robert Dudley, whose ideas on using robots to study flight evolution were truly transformative, and opened up a whole new area of research that I could never have predicted when I first began my studies. I would also like to thank Professor Claire Tomlin, whose comments both as a committee member and my qualifying examination chair provided a valuable outside view on this research. I'd like to thank Dennis Evangelista for helping me track down biology references and making my wind tunnel time efficient.

I would like to thank all of the friends I have made during my time here. Their willingness to grab a few beers after those long days made all the difference. In particular, I'd like to thank my roommates over my time here: Brandon Bunker, Cameron Noland, Matt Carlberg, Sarah Bird, Scott Beamer, Amit Lakhani, Selina Pan, Katherine Smith, and Ginger Smith.

Finally, I would like to thank my family. To my cousin Ryan, thank you for always being there on the other end of the phone, and for being my oldest friend. I am grateful to my uncle Greg for getting me started in engineering, and to him and Marilyn for being my "summer parents." To Stephen and Chris, some of my fondest memories have been my visits and conversations with you, and I look forward to many more. I am thankful for the constant support of my sisters, Megan and Michelle, who continually make me proud with their own accomplishments. And lastly, I'd like to thank my parents, Charlie and Sally. To my dad – for being a constant role model, for acting as a voice of reason, and for teaching me true integrity; and to my mom – for always being there, for the cumulative hours upon hours of phone calls during my walks to campus, and for making me the person I have become — thank you both.

Chapter 1

Introduction

> *The desire to fly is an idea handed down to us by our ancestors who, in their grueling travels across trackless lands in prehistoric times, looked enviously on the birds soaring freely through space, at full speed, above all obstacles, on the infinite highway of the air.*
>
> –Wilbur Wright

Despite the incredible variety and expanse of environments in nature, animals have evolved to inhabit nearly every possible location. Biologists often marvel at the specialized features developed in response to environmental pressures that allow animals to succeed across the many, and often harsh, terrains. However, focus on a single capability hides the realization that most animals are not specialists, but generalists. Using a common set of features, namely skeletal muscles, animals have not only developed specialized capabilities for aerial, terrestrial, and aquatic environments [61], they repeatedly adapt their current features for highly capable locomotion in all the environments they encounter.

The gecko has amazed scientists with its climbing and adhesive abilities since they were first reported on by Aristotle in the 4th century B.C. However, geckos are quite capable at terrestrial running, and recent research has shown the remarkable use of their tails for aerial maneuverability [30]. In fact, geckos, and lizards in general, use their tails for a variety of maneuvers when navigat-

Figure 1.1: *Periplaneta americana* using its wings for added stability when encountering an obstacle. Courtesy of T. Libby.

ing unexpected obstacles [38]. The desert dwelling sandfish lizard is capable of running across the surface with its limbs, and "swimming" underneath the sand with an undulatory body motion [42]. A variety of birds are not only capable of aerial flight, but use their wings for efficient underwater swimming [40]. Precocial birds use their wings to augment their ability to run up steep inclines [10, 65]. Figure 1.1 shows the american cockroach (*Periplaneta americana*) using its wings for stability when encountering an obstacle. Environmental uncertainty repeatedly forces animals into unknown situations, and the ability to use multifunctional locomotion modes is a strong natural selector for those that survive.

This same principle can be applied to the design of small mobile robots. While navigating complex three dimensional environments is an ability that is seemingly trivial for small animals such as the gecko, it provides significant challenges for robots today. The majority of current robots focus on a single locomotion capability. This dissertation proposes that the ability for multiple forms of locomotion as seen throughout the animal kingdom is a mandatory condition for exploring unstructured environments. Towards this proposal, we discuss the advantages of a robot capable of both terrestrial and aerial methods of locomotion.

While there are many robots capable of advanced terrestrial or aerial locomotion, they are also fundamentally limited. Obstacles much larger than the robot present a significant challenge in legged locomotion, and even robots with the ability to climb up obstacles would be impeded when confronted with an aquatic obstacle. Legged robots are also very dependent on their foot-ground interaction dynamics, which can be greatly affected by the environment. In confined spaces, aerial robots are often unable to navigate, and unsteady airflows can cause catastrophic crashes of small aerial robots. Flying also requires a large amount of energy, and no robot can stay aloft indefinitely. Terrestrial locomotion may be more energy efficient for shorter distances, and allows for locomotion even if the energy for flight is spent. By being capable of both aerial and terrestrial locomotion, a hybrid robot could choose the best mode of locomotion given the obstacles confronting it.

Small, mobile robots (mass on the order of grams, linear dimensions on the order of centimeters) provide many advantages when exploring an environment, and are capable of operating in the small spaces unreachable by larger robots. In addition, their small size allows multiple robots to be transported and deployed, greatly increasing the amount of area they can cover. The ability of many small robots to enter the small spaces left in a collapsed building could prove invaluable in searching for survivors after a natural disaster such as an earthquake. With the continuing decrease in cost and size of radios and sensors, small robots can also be used to set up a mobile sensor network for environmental or industrial monitoring in dangerous or hard to access areas.

Many challenges still exist before such small scale robots can reach their promised potential. At small scales, traditional methods of design and manufacturing become difficult. Mechanisms such as pin joints become very inefficient due to the increased friction that results from the higher surface area to volume ratio at small scales. In addition, the small size leads to very high tolerance requirements on all components. To address this issue, the UC Berkeley Biomimetic Millisystems Lab has pioneered the use of Smart Composite Microstructures (SCM, [67, 26]). SCM mechanisms consist of a rigid link (Carbon Fiber or Cardboard) integrated with a compliant polymer (PET) to form two-dimensional structures that can be folded into complex three-dimensional mechanisms. This technique allows the creation of complex, many jointed mechanisms at small scales that both move efficiently due to flexure joints, and are simpler to build due to a significantly reduced part count. The 2.5 dimensional fold-up design also leads to lightweight structures compared to traditional 3-dimensional designs. The SCM process is a critical underlying technology for the work presented in this dissertation, enabling the creation of complex, multifunctional robots at the small scale.

A further challenge in designing meso-scale hybrid robots is maintaining high power density, an important consideration for enabling aerial performance. At the meso-scale, small, brushed DC motors provide the best performance capabilities in comparison to other actuator technologies currently available. However, to maintain high power density, the number of actuators must be limited, leading to uncontrolled degrees of freedom. The proper use and tuning of available actuators is an important aspect for designing efficient, high performing robots. Towards this end, reduced order locomotion models can provide key insights, and allow the investigation of the effect of various tuning parameters on performance.

In addition to studying biology to inform the design of robots, a robotic platform can also be used to investigate biological theories. One such example is the contentious debate surrounding avian flight evolution. Current support for the diverse theories of avian flight origins derives from limited fossil evidence, the adult behavior of extant flying birds, and developmental stages of already volant taxa. We propose that through the investigation of robotic models, theories on the evolution of avian flight can be directly tested and evaluated.

1.1 Contributions and Outline

This work makes the following contributions:

- **Design of two hybrid legged/winged robots** - DASH+Wings (Dynamic Autonomous Sprawled Hexapod plus Wings) and BOLT (Bipedal Ornithopter for Locomotion Transitioning) are two meso-scale robots capable of hybrid aerial and terrestrial locomotion. DASH+Wings is a six-legged, two-winged robot capable of wing-assisted terrestrial running, and controlled aerial descent. BOLT is a two-legged, four-winged robot capable of both crawling and sustained flight. Chapter 3 presents the key insights that enabled the design of these small, but highly capable systems, and discuss the methods used in their design and construction.

- **Development and analysis of a sagittal plane reduced order model for wing-assisted locomotion** - Sagittal plane models have been used frequently in the literature to understand the complicated dynamics of terrestrial locomotion. In Chapter 4, we develop a reduced order hybrid model for wing-assisted locomotion. Numerical simulations are used to elucidate the interactions between the legs and the wings as various parameters in the model are adjusted.

- **Characterization of flapping wing aerodynamically assisted running of a bipedal robot** - In Chapter 5, we investigate the effects of flapping wings on the terrestrial locomotion of a hybrid robot (BOLT). The difference in dynamics at different stride frequencies is examined and the effect on cost of transport is measured. The ability of the robot to takeoff and fly as well as climb walls and traverse obstacles is also discussed.

- **Characterization of the effects of passive aerodynamic stabilization on a high-speed running robot** - The addition of passive aerodynamic roll stabilization increased the performance of VelociRoACH, a 10 cm long running robot. VelociRoACH is capable of running at 2.7 m/s, or 27 bl/s, making it the fastest legged robot relative to scale known to the author. In Chapter 6, aerodynamic stabilization is shown to reduce the total rotational energy, allowing the robot to run in a more stable trajectory. The ability of the robot to reject disturbances is also improved.
- **Analysis of a hybrid aerial/terrestrial robot in the context of avian flight evolution** - The origin of avian flight is a hotly contested issue, and one that is difficult to resolve. We present a discussion of the issue in Chapter 7, and analyze the performance characteristics of DASH+Wings and the implications its performance has for understanding avian flight evolution. We also examine a new morphologically correct flapping model and further explore the origins of avian flight.

Chapter 2

Background

In recent years, the capabilities of legged robots has advanced very rapidly. This advancement was spurred in part by insights from biologists and mathematicians, and better understanding of how animals locomote so well. The locomotion dynamics of these robots is characterized by the spring loaded inverted pendulum model (SLIP) [24], a pattern exhibited by nearly all legged organisms despite widely varying leg numbers [7].

2.1 Locomotion Models

Animals exhibit an extensive variety of incredibly robust methods of locomotion. The study of the capabilities found in nature has great implications for the design of similarly robust and capable robots. However, animals are very complex, high degree of freedom systems subject to many different constraints, of which locomotion is only one. To advance the understanding of locomotion, Full and Koditschek introduced the concept of templates, or lower dimensional representations of a system, to explain the underlying dynamics of both animals and legged robots [20]. Through the creation of representative models, much can be learned about the principles of legged locomotion.

Perhaps the most well known representative model is the spring-loaded inverted pendulum model for legged locomotion. This model has been studied extensively [24], and the passive dynamics of the SLIP have been shown to accurately explain the underlying sagittal plane dynamics of legged locomotion across a range of animals [7]. The basic SLIP model is a conservative model, and shows passive stability properties for a range of parameters. However, for many parameters corresponding to the real-world properties of both animals and robots, the model is unstable and does not accurately explain the dynamics. To address this, additional complexity has been added to the model, allowing a better understanding of how the model can inform the design and analysis of legged locomotion. A common extension to the model is the introduction of actuation into the model, such as linear leg extension actuators [60] or hip torques [62]. The addition of hip torques and a simple, clock-based control scheme allows the model to explain the dynamic stability of legged locomotion with physically relevant parameters. In extending the sagittal plane model to three dimensions, Seipel and Holmes showed that the model is no longer passively stable, and feedback control is necessary for stable running [63]. Along with informing our understanding of legged locomotion in animals, the underlying principles of dynamic locomotion models have been used in the mechanical design and control of fast and robust legged robots

2.2 Hybrid Robots

The first robots to take advantage of this understanding included Sprawlita [13] and RHex [59], both of which used carefully tuned compliant legs to achieve efficient dynamic locomotion. Sprawlita used pneumatic actuators to achieve exceptional performance for its time, although the actuators required an external air source. RHex achieved full power autonomy, and fully integrated the notion of preflexes [9] to simplify the control and design of the robot while still maintaining high performance. Building upon the success of these larger robots, iSprawl [31] and Mini-Whegs [45] represent the next generation of terrestrial robots. These robots are power autonomous, while also being smaller in size and faster (as measured in body lengths per second) than previous robots. Most recently, the use of the Smart Composite Microstructures [67, 26] construction process has enabled the design of several lightweight, high performance terrestrial robots, including DASH [6], DynaRoACH [25], and VelociRoACH [22]. DASH achieved similar running performance to iSprawl, while weighing over an order of magnitude less, leading to a lower energetic cost of locomotion. DASH also proved to be extremely durable, capable of surviving falls at terminal velocity. DynaRoACH examined maneuverability and showed that altering leg stiffnesses can lead to dynamic turning maneuvers. The VelociRoACH built upon the designs of DASH and DynaRoACH to become the fastest legged robot relative to scale built to date, with a maximum forward speed of 2.7 m/s (27 bl/s). As the abilities of legged robots have advanced, robots have started to incorporate additional appendages to advance their capabilities. As an example, TAYLRoACH [33] incorporates an active tail to enable extremely rapid dynamic turning.

With the exception of Mini-Whegs, these robots all use six legs arranged in an alternating tripod configuration for passive stability when running. In contrast, dynamic bipedal running has generally required a complex controller and multiple actuators to maintain stability. Dynamic bipedal running has been previously demonstrated by RHex [46], along with an extensive list of larger bipedal robots. At the very small scale, dynamic bipedal running can be seen in the cockroach *Periplaneta americana* when it is running at its fastest speeds [19].

Similar to the improvement seen in terrestrial robot, the performance of meso-scale ornithopters has also dramatically increased recently. The well-known DelFly II [37] is a 28 cm wingspan ornithopter capable of hovering flight in an indoor environment. At the smaller scale, the Micro Delfly exhibits high performance while only weighing 3 grams and still being capable of carrying a camera. The Aerovironment Nano Hummingbird [1] is a true large hummingbird-sized robot, capable of hovering flight.

While the fields of terrestrial and aerial locomotion have advanced rapidly in recent years, hybrid locomotion capabilities are relatively new. One of the first small hybrid robots was the Micro Air Land Vehicle (MALV) [4], a combination of Whegs$^{\text{TM}}$ with a fixed wing and propeller for flight. Capable of both aerial and terrestrial locomotion, MALV requires a 3-5 meter runway or a 6 meter vertical drop in order to take off. Its descendant, MMALV [8], is capable of folding its wings when on the ground for a reduced profile. The Skyhopper$^{\text{TM}}$ by WowWee$^{\text{TM}}$, is an ornithopter capable of rudimentary hopping when on the ground. The EPFL microglider [34] is not capable of powered flight, but seeks to combine aerodynamic gliding with terrestrial jumping to maximize performance. Work has also been done on aerial-terrestrial transitions, with [35] and [41] both capable of wall perching.

Hybrid robots are not limited to only an aerial-terrestrial combination. Others which have been developed primarily focus on terrestrial and aquatic locomotion such as Boxybot [36] and AQUA, a waterproof version of RHex [21].

Chapter 3

Design of Hybrid Running/Flying Robots

This chapter presents the design of two hybrid legged/winged robots. DASH+Wings [55] is a six legged/two winged robot derived from DASH [6], the Dynamic Autonomous Sprawled Hexapod. As DASH was designed as a terrestrial running robot, it is more capable on the ground compared with in the air. While not capable of sustained flight, DASH+Wings is capable of controlled aerial descent. Its flapping wings also increase its terrestrial capabilities beyond the original robot.

Whereas DASH+Wings shows many aspects of improved performance, a fully functional flying and crawling robot requires a more integrative design that focuses equally on aerial and terrestrial locomotion. Because of DASH+Wings' origin as a terrestrial robot, it has a more anterior center of mass location to reduce pitching during acceleration, yield better climbing abilities, and generate more stable and predictable gaits. By contrast, enhanced gliding performance would derive from a more posterior center of mass not presently feasible given its transmission design. DASH+Wings' mass was also too high given the performance capabilities of its wings.

BOLT [56], the Bipedal Ornithopter for Locomotion Transitioning, was designed based on the key insights learned from DASH+Wings. The primary design goal for BOLT was the development of a platform capable of both terrestrial and aerial locomotion. To accomplish this goal, we combine the gearbox and wings from a commercial ornithopter (Air Hogs$^{\text{TM}}$ V-wing Avenger$^{\text{TM}}$) with a custom airframe, leg design, and electronics package. Because of the desire for stable hovering flight, weight and weight distribution are a key consideration in all design decisions. In reducing the number of legs on BOLT to two, some terrestrial performance is sacrificed. However, the ability of the flapping wings to aid performance when running along the ground minimizes the decrease in performance. The decision to reduce the number of legs was made based on this insight from DASH+Wings. Reducing the number of legs reduced the overall mass of the system and simplified the design, allowing BOLT to meet the design goal of sustained flight.

3.1 Design of DASH+Wings

DASH (Fig. 3.1a) and DASH+Wings (Fig. 3.1b) are both constructed using the scaled Smart Composite Manufacturing (SCM) process [26]. The SCM process allows the implementation of com-

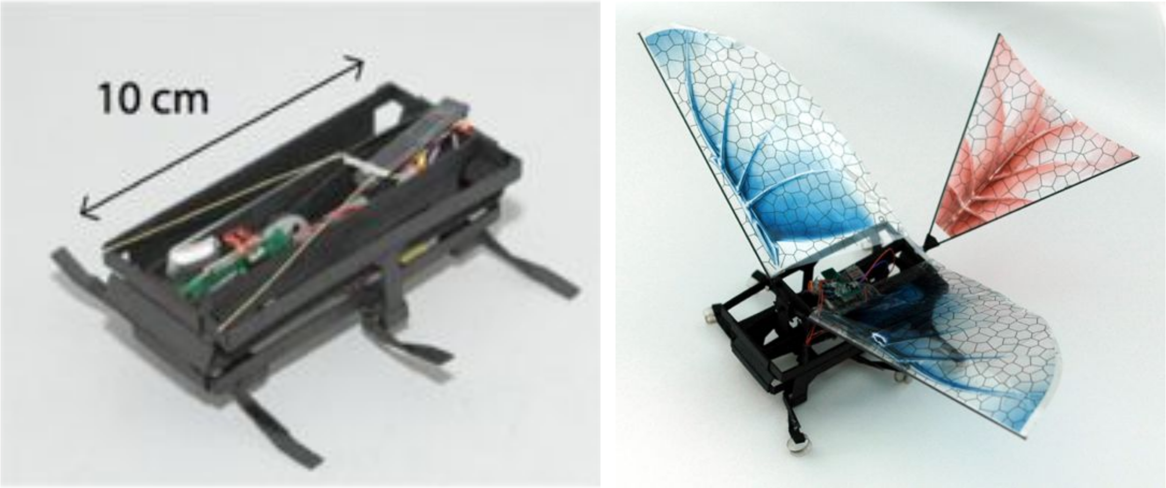

(a) DASH [6]

(b) DASH+Wings

Figure 3.1: DASH and DASH+Wings, two palm sized hexapedal running robots.

plicated kinematics while keeping the overall weight of the robot low. Additionally, design changes can be made quickly, allowing the integration of the wings with the original crawling platform.

DASH+Wings has a 14 Hz stride and flapping frequency. The robot runs with an alternating tripod gait, and each tripod contacts the ground once per stride. The stroke of the wings lies in the transverse plane, and distends an angle from 32° above horizontal to 2° above horizontal, yielding a flapping amplitude of 30°. The wings and tail derive from the design of the VAMP RC ornithopter (Interactive Toy Concepts). The wings consist of a stiff leading edge spar with a thin plastic membrane anchored to the body at the rear inside corner (Fig. 3.1b). The wing is 0.124 m long with an average chord of 0.064 m, giving an aspect ratio of 1.94. The total area of each wing is 0.0079 m^2. The membrane is biased to have a positive camber of 0.0626 (calculated as the maximum vertical displacement from the planform divided by the average chord length) when the wing is at rest at the lower position of the stroke plane. The total mass of the inertial leading edge spar alone is 0.17 g, and the mass of the wing membrane is 0.36 g, for a total mass of 0.54 g per wing. The tail consists also of stiff spars supporting a thin membrane with a length of 0.085 m and a total area of 0.00419 m^2, mounted at an angle of 40.5°with respect to the body. It functions to provide passive pitch stability to the robot while in flight.

The original DASH robot used a single motor to actuate two plates in relative circular motion that drives six legs in an alternating tripod gait. The transmission mechanism uses a differential drive design, causing significant motion of the center of mass (COM) within the robot. In addition, the compliant design of DASH precludes using the rigid-body kinematics to predict the COM location, as the center of mass does not follow its prescribed path exactly. These artifacts of DASH's design make measuring the accelerations on the center of mass more challenging than on a robot where the COM can be assumed stationary.

In order to examine the effects of wings on ground locomotion, several changes were made to

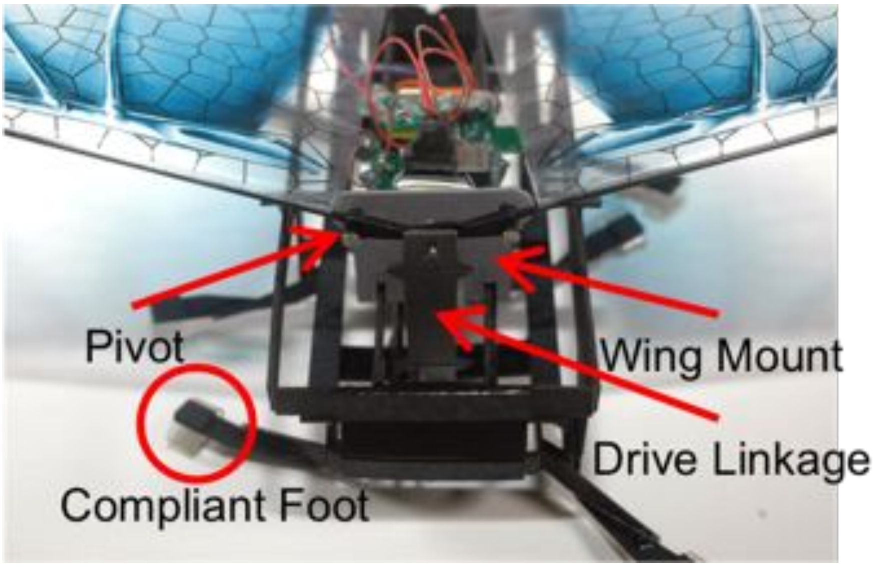

Figure 3.2: Mechanical design of DASH+Wings, showing the wing mount and compliant feet. The wings are mounted to the top plate of DASH, with the drive linkage connected to the bottom plate. Compliant feet are added to the legs to maintain the appropriate stiffness for stable running.

the original DASH robot. To drive the flapping motion of the wings, an additional linkage was added that couples the vertical motion of the two drive plates to the wing mechanism (Figure 3.2); the same motor that drives the legs thus also drives the flapping wings. The leg-to-wing phasing was chosen due to the simplicity of integration of the wing mechanism with the already present leg transmission. The kinematics of the system set the wing to be at the top of its stroke when the first tripod is mid-stance and at the bottom of its stroke when the second tripod is mid-stance. The actual position of the wings with respect to the legs changes when the robot is dynamically running because of compliance present in the mechanism and the high inertia of the wing. High-speed video shows that the extremes of the wing stroke correspond to the end of the stance phases instead of the middle of the stance. The wings are easily removed, allowing the same robot to be tested both with and without wings, and thus minimizing differences in performance due to construction variability.

Whereas the original DASH robot could run at a stride frequency of 17 Hz, this modified DASH has a maximum stride frequency of 14 Hz because of the additional power the motor requires to drive the wings in addition to the legs. We therefore implemented a PID controller on the motor to ensure that stride frequency remained constant over all trials and experimental configurations. The controller runs on a small (2.7 g) electronics package (GINA mote; [44]) containing a Texas Instruments MSP430 processor, a Kionix KXSD9-1026 triaxial accelerometer, and an Atmel AT86RF231 radio. Addition of wings, tail, and wing linkages to DASH, along with the electronics controller package, resulted in a total weight of 25 g compared with 16 g for the unmodified DASH.

Adding these components also resulted in stiffening the compliance present in the body of the robot. This distributed compliance was critical for the original DASH robot to maintain a stable dynamic gait. The GINA mote is also a significant portion of the total mass of the robot, and its position on the top plate of the robot raises the overall center of mass, further destabilizing the robot. To compensate for these changes, we added compliant feet to each of the six legs to properly tune leg stiffness for stable running in all of the test configurations. The feet were required to meet the following constraints: integrable with the SCM process, lightweight, and easily tunable. The foot design that met all of these criteria is a basic polyester loop added to the end of a rigid cardboard leg (Figure 3.2). This is directly integrable with the cardboard process, and the addition of the polymer loop adds only 40 milligrams to the leg. We adjusted the stiffness of the feet experimentally by varying the width and loop diameter until the robot ran stably in all configurations.

A more detailed treatment of the mechanical design of DASH+Wings can be found in [6] and [57]. The performance of DASH+Wings is discussed in Chapter 7.

3.2 Design of BOLT

The Bipedal Ornithopter for Locomotion Transitioning, or BOLT (Figure 3.3), is a small lightweight robot capable of both aerial and terrestrial locomotion modes. The integration of an electronics package allows two-way communication and the investigation of the robot dynamics with a six-axis inertial measurement unit (IMU). BOLT has a total weight of 11.4 grams, with a wingspan of 28 cm and a length of 17.5 cm. The robot is capable of dynamic high-speed bipedal locomotion by exploiting its aerodynamic properties for stability. The use of aerodynamics during bipedal locomotion has been previously seen in some birds [10], although generally only in inclined running. The Smart Composite Microstructures (SCM) [67] process allows the integration of a lightweight leg structure with the rest of the body, comprised mainly of carbon fiber spars.

3.2.1 Airframe Design

BOLT's airframe uses carbon fiber spars for structural rigidity. The lightweight properties of carbon fiber make it ideal for use in a flying platform. A rigid airframe is critical in preventing serial compliance from reducing the wing thrust. To create the lightweight tail, carbon fiber spars are placed in a cardboard pattern and a 12.7 μm film of polyethylene terephthalate (PET) is overlaid and attached to the spars with cyanoacrylate (Fig. 3.4a). The construction materials of the tail are similar to those used in [37], a successful ornithopter on the same size scale as BOLT.

The center of mass location of the robot is important for determining the posture of the robot when it is in the air. We place the battery at the very posterior of the robot on the tail, while the controller board is placed within the airframe. This gives the robot a vertical posture, with the majority of the wing thrust directed downward. By adjusting the position of the controller board, the robot can be set to either hover in place or fly forward at a slow rate. The airframe of the robot also protects the controller board during operation.

Figure 3.3: BOLT: a bipedal ornithopter capable of both aerial and terrestrial locomotion.

Directly mounting the controller board to the rigid carbon fiber airframe overwhelms the accelerometer due to the high frequency vibrations produced by the motor transmission. To accurately study the dynamics of the robot, the board is moved forward and placed on foam mounts (Fig. 3.4b) to dampen the vibration noise and improve the quality of the acceleration measurements.

A critical feature enabling ground-to-air transitions of the robot is the angle of attack of the wings. The clap-and-peel design of the wings produces force directed perpendicularly to the stroke plane. On the initial iterations of BOLT, the wings had a low angle of attack, directing propulsive force horizontally when running along the ground. This robot was capable of flight, but could only takeoff by running from a one meter or higher ledge. Once in the air, the center of mass location caused the tail to swing under the robot and it entered a stable flight posture. Increasing the wing angle of attack allows the robot to build lift as the forward speed increases, eventually causing the robot to pitch upwards, directing the main flapping force downwards. This leads to takeoff from the ground and the robot entering a stable flight posture due to the center of mass location with respect to the center of lift. On BOLT, the angle of attack is set to 28 degrees. This value was chosen experimentally to provide a balance between the robot's maximum terrestrial speed, and the distance required for takeoff.

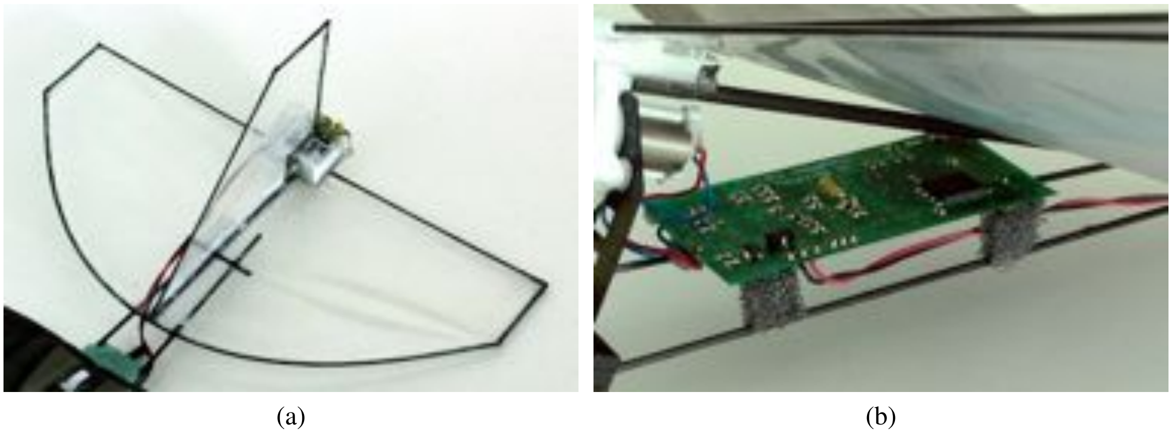
(a) (b)

Figure 3.4: (a) shows the tail of BOLT, constructed from carbon fiber spars and 12.7 micron thick PET film. The battery is placed at the back of the tail to maintain proper weight distribution. (b) shows the controller board mounted on small foam offsets. The foam offsets are critical for dampening the high frequency vibrations of the body.

3.2.2 Leg Design

BOLT has a bipedal leg design, with each leg going through a symmetrical motion 180 degrees out of phase with the opposite. A single motor drives both the leg and the wings, allowing sufficiently high power density to maintain hovering flight. The legs are built using the SCM process [67], which allows the implementation of a lightweight structure that transforms the output of the motor to the desired leg trajectory. Four layers of unidirectional carbon fiber pre-preg are sandwiched around 50.8 μm PET to create the leg structure. The layers of the unidirectional carbon fiber are arranged crosswise to provide stiffness in two directions, and are mirrored across the flexure layer. The structure is designed to provide protection to the hips in case of high velocity impacts, while allowing the legs to still extend in front and below the body.

Figure 3.5 shows a simplified version of the mechanisms that transform the rotation of the motor in the transverse plane of the robot to the desired leg trajectories. A set of parallel four-bars drives the vertical motion of the legs (Fig. 3.5a), while a crank-slider mechanism drives the fore-aft motion of the legs (Fig. 3.5b). One revolution of the motor output gear (hereafter referred to as a single motor cycle) corresponds to a full left and right leg stride, and a single complete wing beat (opening stroke and closing stroke). In implementing the mechanisms shown in Figure 3.5, several implementation details are necessary due to the properties of the SCM process. The structure is designed such that each of the flexures is in a straight default configuration, reducing the effect of off-axis forces and minimizing the strain of the PET (Fig. 3.6a). The motion of the legs is shown in Figure 3.6.

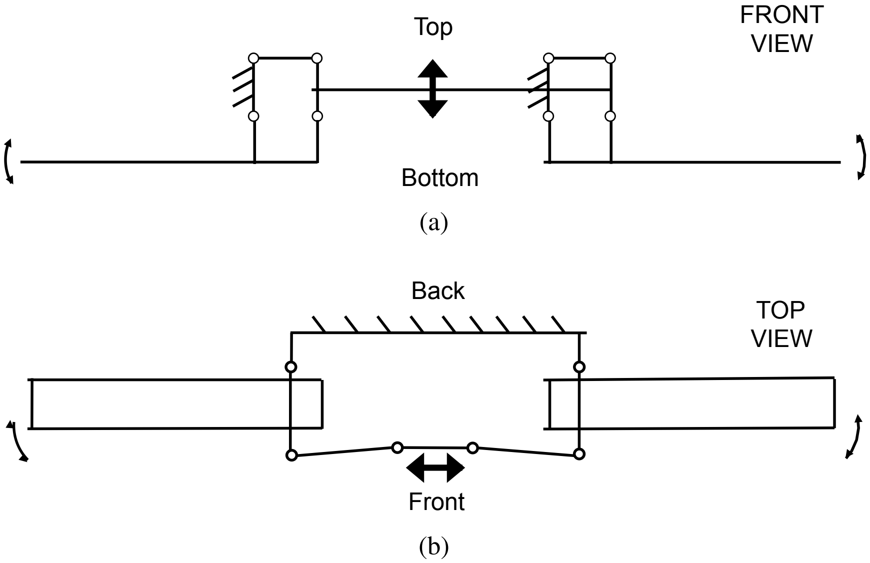

(a)

(b)

Figure 3.5: Simplified representation of the mechanisms that enable the (a) vertical motion and (b) fore-aft motion of BOLT's legs.

Table 3.1: Physical properties and components of BOLT

Total Mass	11.4 grams
Body Size	17.5 x 28 x 15 cm
Battery	Full River 60 mAh lithium polymer
Micro-controller	Microchip dsPIC33F
Communications	Atmel AT86RF231
Accelerometer	Analog Devices ADXL345
Gyroscope	Invensense ITG-3200

3.2.3 Power, Communications, and Control

BOLT uses a custom electronics package (ImageProc 2.2) that incorporates a 40 MHz dsPIC processor with a motor driver, six-axis IMU, and 1 MB of Flash memory (Table 3.1) [5]. In addition, the board has an Atmel 802.15.4 radio for communication with a laptop. A Python interface sends commands to the robot and receives data from the board's sensors. A 60 mAh battery powers the electronics board and motor.

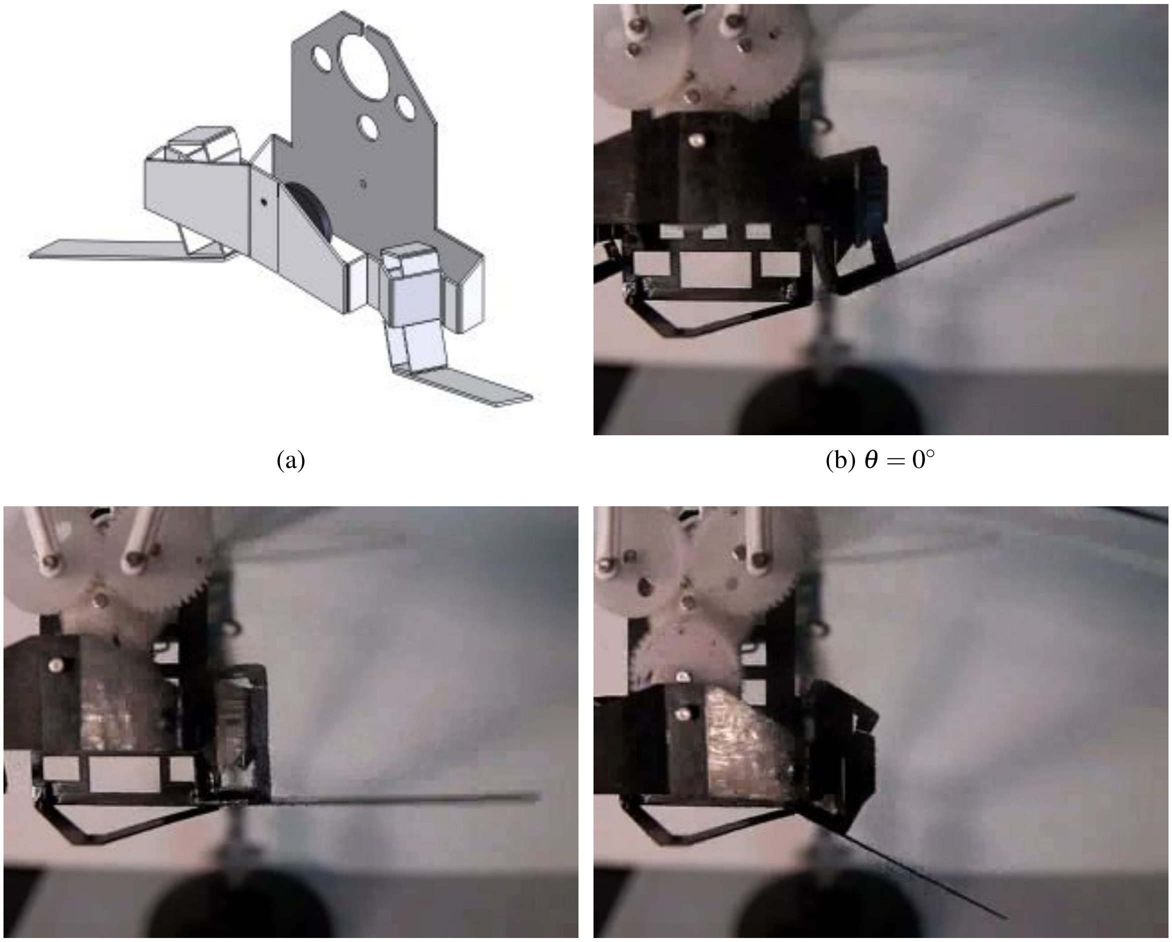

(a)

(b) $\theta = 0^\circ$

(c) $\theta = 135^\circ$

(d) $\theta = 205^\circ$

Figure 3.6: The implementation of the mechanism described in Figure 3.5 is shown by (a). Here, the movable flexures have been straightened, reducing the strain and the effect of off-axis forces. (b)-(d) show frames from high-speed video of the left leg moving through its stride. The right leg exhibits similar motion in anti-phase with the left.

Chapter 4

A Sagittal Plane Model for Wing-Assisted Locomotion

This chapter presents a dynamic model for wing-assisted running based on the design of BOLT. The experimental results presented in Chapter 5 suggest that there are important differences between the traditional SLIP-like gait found in pure legged robots and animals and the locomotion of BOLT due to the influence of the flapping wings. The effects of parameters such as leg stiffness and wingbeat phasing is poorly understood for wing-assisted terrestrial locomotion, and the use of a dynamic model allows more extensive examination of the parameters effects than can be implemented in a physical system. Our model combines the classical SLIP model with the effects of flapping wings, and examines the interaction between the periodic leg and wing forces present in the system across a range of possible design parameters.

4.1 Description of the Hybrid Dynamic Model

To examine wing-assisted terrestrial locomotion, we develop a reduced order model capable of qualitatively reproducing the sagittal plane dynamics of a wing-assisted running robot (WingSLIP). The model consists of a three degree of freedom rigid body, shown in detail in Figure 4.1. A local coordinate frame, given by $\mathbf{e_1}$ and $\mathbf{e_2}$, is fixed to the CG of the model with $\mathbf{e_1}$ aligned parallel to the vector between the tail and hip location. The global coordinate frame is represented by $\mathbf{E_1}$ (horizontal) and $\mathbf{E_2}$ (vertical). The dynamics of the system are described by the position ($\mathbf{r} = [\mathbf{r}\cdot\mathbf{E_1}, \mathbf{r}\cdot\mathbf{E_2}]^T = [r_1, r_2]^T$) and velocity ($\dot{\mathbf{r}} = [\dot{\mathbf{r}}\cdot\mathbf{E_1}, \dot{\mathbf{r}}\cdot\mathbf{E_2}]^T = [\dot{r}_1, \dot{r}_2]^T$) of the center of gravity (CG), as well as the pitch rotation and angular velocity of the body ($\psi, \dot{\psi}$). Table 4.1 lists the physical dimensions of the model, based on the design detailed in section 3.2.

4.1.1 Foot, Leg, and Hip Model

The leg model consists of two legs in anti-phase rotating about the hip. Each leg is modeled as a linear spring, and is attached at the hip to the motor through a torsional spring. We make

(a) Side view of BOLT, described in section 3.2.

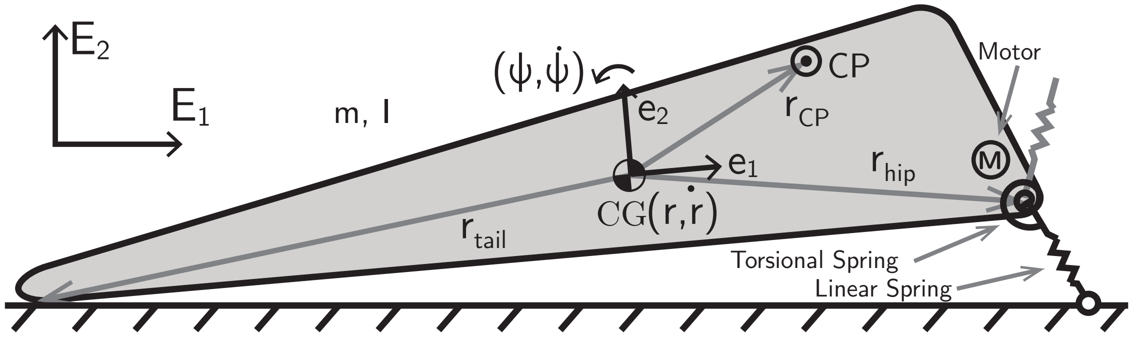

(b) Reduced-order sagittal plane model.

Figure 4.1: WingSLIP, a hybrid dynamic model for investigating wing-assisted locomotion.

Table 4.1: Physical properties of the WingSLIP model

m, mass	$0.012\,\mathrm{kg}$
I, inertia	$30.5\times10^{-6}\,\mathrm{kg}\cdot\mathrm{m}^2$
ζ_0, Nominal Leg Length	$0.02\,\mathrm{m}$
$\mathbf{r}_{CP}$, CP Location	$[0.03\,\mathrm{m}, 0.017\,\mathrm{m}]$
$\mathbf{r}_{Hip}$, Hip Location	$[0.065\,\mathrm{m}, -0.01\,\mathrm{m}]$
$\mathbf{r}_{Tail}$, Tail Location	$[-0.1\,\mathrm{m}, -0.01\,\mathrm{m}]$

several common assumptions found in prior studies of reduced order models [62, 73]. The mass of the legs/feet is neglected, as they are generally a very small portion of the total mass. The leg is assumed to be rigid to bending, allowing the forces from the linear and torsional spring to be decoupled. Since the legs and feet are massless, we assume that the legs follow the reference trajectory exactly when not on the ground.

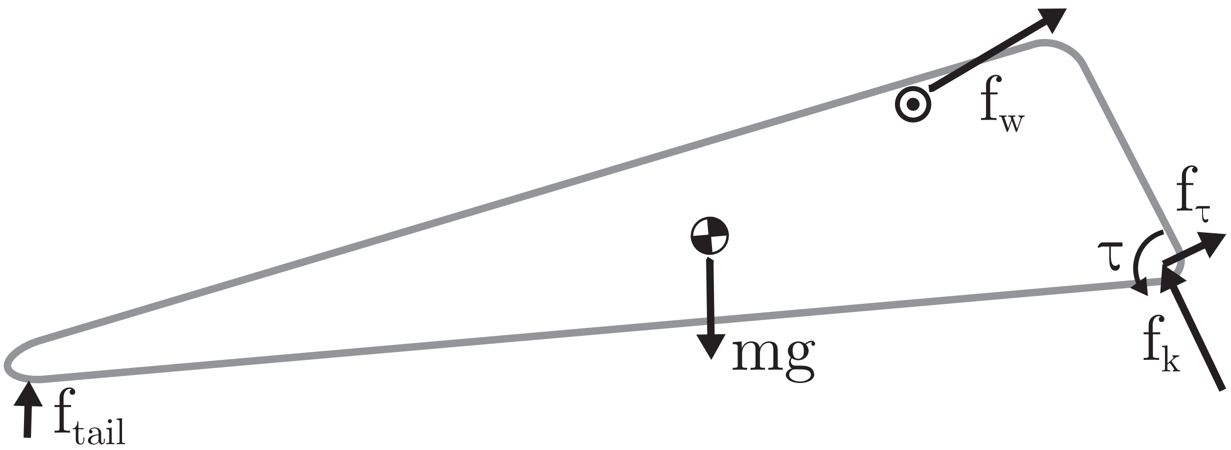

Figure 4.2: A free body diagram showing all of the forces acting on the WingSLIP model during the single-stance phase.

Due to the discontinuous nature of the foot contact, the leg dynamics are described by a hybrid model with four states corresponding to the aerial phase, foot 1 or 2 on the ground, and double stance. The touchdown condition for each foot is given by

$$g_{(i)}^{TD} := (\mathbf{h} + \zeta_0 R(\psi)[-\sin\theta_{(i)}, -\cos\theta_{(i)}]^T) \cdot \mathbf{E}_2 = 0, \tag{4.1}$$

where $\mathbf{h}$ is the position of the hip, $R(\psi)$ is the rotation matrix from $\mathbf{e}$ to $\mathbf{E}$, and $\theta_{(i)}$ is the reference angle of leg i. A free body diagram of the robot in single stance phase is shown in Figure 4.2. The force at the hip due to the linear leg spring is given by

$$\mathbf{F}_{Ks} = k_s(\zeta_0 - \zeta)(-\sin\phi\ \mathbf{E}_1 + \cos\phi\ \mathbf{E}_2), \tag{4.2}$$

where k_s is the linear spring constant. The leg angle ϕ is found from the hip position $\mathbf{h}$ and the foot position $\mathbf{p}$:

$$\phi = -(\frac{\pi}{2} + \arctan\frac{-\mathbf{h}\cdot\mathbf{E}_2}{(\mathbf{p}-\mathbf{h})\cdot\mathbf{E}_1}). \tag{4.3}$$

The leg length ζ is found from:

$$\zeta = \frac{\mathbf{h}\cdot\mathbf{E}_2}{\cos\phi}. \tag{4.4}$$

The torque on the body at the hip from the torsional spring is given by

$$\tau = k_\tau(\theta_{(i)} - \phi), \tag{4.5}$$

and the force due to the hip torque is given by

$$\mathbf{F}_{K\tau} = \frac{\tau}{\zeta}(\cos\phi\ \mathbf{E}_1 + \sin\phi\ \mathbf{E}_2). \tag{4.6}$$

Table 4.2: Parameters of the WingSLIP model

Parameter	**Description**	**BOLT value**
k_s	Linear Leg Stiffness	4.9 N/m
k_τ	Torsional Leg Stiffness	0.0039 Nm/rad
f	Motor/Wingbeat Frequency	9, 12.5 Hz
f_{ratio}	Leg/Wing Effective Gear Ratio	1
θ_{offset}	Leg/Wing Phase Offset	1.75 rad

During stance phase, the foot contact is assumed to act like a pin joint. No adhesion is allowed by the model, and so the liftoff condition is given by

$$g_{(i)}^{LO} := (\mathbf{F}_{(i)} \cdot \mathbf{E_2}) < 0. \tag{4.7}$$

As the robot is designed to run on carpet, where the foot often snags on the loops, a pin joint, non-sliding contact is a valid assumption.

During the aerial phase, the force from both legs is zero, while in double stance phase, the force from both legs must be considered.

4.1.2 Wing Model

We use an empirically derived model for the wing forces based on experiments performed using a wind tunnel (Aerovent, Inc.). The robot was mounted on an ATI Nano-17 6-axis force-torque transducer, and the lift and drag forces were measured across a range of flapping frequencies and horizontal airspeeds. At each flapping frequency and horizontal airspeed, we extract the components of the force signal by taking the Fourier decomposition of the measured data. The amplitude and phase coefficients of the Fourier series are then parameterized as a function of the flapping frequency and airspeed.

$$\mathbf{F}_w = \mathbf{A}_0 + \sum_{k=1}^{n} \mathbf{A}_k \cos(2\pi f k\, t + k\, \theta_{\text{offset}}) \tag{4.8}$$

Because of the clap and fling wing motion, the thrust and lift force from the opening and closing stroke are nearly equivalent–leading to a large second harmonic term in the wing force. Therefore, for simplicity, we only consider the DC term and dominate second harmonic term in our wing force model. Nonlinear regression was used to find the best least squares fit for the amplitude coefficients as functions of the flapping frequency and airspeed.

$$\begin{aligned} \mathbf{A}_0 = \quad & (0.00492f - 0.02853v + 0.00150v^2)\mathbf{e}_1 + \\ & (0.00106f - 0.00337v + 0.00208fv + 0.00476v^2)\mathbf{e}_2 \end{aligned} \tag{4.9}$$

$$\begin{aligned} \mathbf{A}_2 = \quad & (-4.8086 \times 10^{-7} f^{4.278})\mathbf{e}_1 + \\ & (0.00210fv + 7.34 \times 10^{-5} f^2)\mathbf{e}_2 \end{aligned} \tag{4.10}$$

4.1.3 Tail Contact Model

In addition to the leg and wing forces, a ground contact force is also imposed at the tail of the model. Because of the location of the hips well forward of the CG location, this constraint force is necessary for the stability of the model. The ground contact force is modeled as a simple spring-damper,

$$F_{\mathbf{t}} = \begin{cases} 0 & \text{if } \mathbf{t} \cdot \mathbf{E_2} \geq 0 \\ -k_g \, \mathbf{t} \cdot \mathbf{E_2} - b_g \, \dot{\mathbf{t}} \cdot \mathbf{E_2} & \text{if } \mathbf{t} \cdot \mathbf{E_2} < 0 \end{cases} \tag{4.11}$$

where **t** represents the location of the tail. The spring (k_g) and damping (b_g) constants were chosen empirically to be 10000 N/m and 100 N/(m/s), respectively. For simplicity we only consider the vertical force on the tail, and neglect any friction force on the tail. The effect of this assumption is discussed further in subsection 4.2.5.

4.1.4 Motor Model

The high periodic loading of the wings leads to a periodic oscillation of the velocity of the motor. Since the same motor is used to drive both the wings and the legs, this oscillation is transmitted to the legs. The motor is running at the limits of its capability when flapping the wings at higher frequencies, and has limited bandwidth the alter this signal. This oscillation functions essentially as a passive Buehler clock [59], with no active control necessary to implement. However, a drawback is the lack of ability to adjust the parameters.

The motor model was determined in the same way as the wing model, and as with the wing model, only the DC term and second harmonic is necessary to capture the motor dynamics:

$$\theta = 2\pi f t + \theta_0 + \frac{-4.2184 + 2.7328 f}{4\pi f} \sin(4\pi f \, t + \frac{\pi}{2} + \theta_{\text{offset}}) \tag{4.12}$$

$$\dot{\theta} = 2\pi f + (-4.2184 + 2.7328 f) \cos(4\pi f \, t + \frac{\pi}{2} + \theta_{\text{offset}}) \tag{4.13}$$

4.1.5 Numerical Analysis

Overall, the forces acting on the rigid body are

$$\mathbf{F} = \mathbf{F}_{\text{w}} + \mathbf{F}_{\text{t}} + \sum_{i=1}^{2} \mathbf{F}_{k_s}^{(i)} + \mathbf{F}_{k_\tau}^{(i)} - g \mathbf{E}_2. \tag{4.14}$$

In addition, we also compute the moments about the CG

$$\begin{aligned} M = \quad & \tau + \mathbf{F}_{\text{w}} \times R(\psi) \mathbf{r}_{wing} \\ & + \mathbf{F}_{\text{t}} \times R(\psi) \mathbf{r}_{tail} \\ & + (\textstyle\sum_{i=1}^{2} \mathbf{F}_{k_s}^{(i)} + \mathbf{F}_{k_\tau}^{(i)}) \times R(\psi) \mathbf{r}_{hip}. \end{aligned} \tag{4.15}$$

The equations of motion can then be described by

$$\ddot{\mathbf{r}} = \frac{\mathbf{F}}{m} \tag{4.16}$$

$$\ddot{\psi} = \frac{M}{I} \tag{4.17}$$

The inclusion of hip torques and wing forces into the model preclude solving the dynamics of the system analytically, and as such a numerical solver is employed. The `ode45` solver in Matlab was used to compute the solutions. In our simulations, we allow for a settling period, after which any stumble of the robot (defined as the hips contacting the ground) is considered a failure. We also constrain the rotation angle to $-\frac{\pi}{2} < \psi < \frac{\pi}{2}$ to prevent the robot from flipping over. The simulation ends when the robot either reaches a stable limit cycle, violates a failure condition, or exceeds the maximum simulation time. To determine if the robot has reached a stable limit cycle, we define a Poincaré section at the touchdown of leg 1 as

$$S := g_{(1)}^{TD}, \tag{4.18}$$

and define the state of the system on this section to be:

$$\mathbf{x}_{TD}(n) = [r_2(n), \dot{r}_1(n), \dot{r}_2(n), \psi(n), \dot{\psi}(n)]^T. \tag{4.19}$$

Next, we examine the norm of the states from touchdown to touchdown:

$$\varepsilon_{TD}(n) = ||\mathbf{x}_{TD}(n) - \mathbf{x}_{TD}(n-1)||. \tag{4.20}$$

To determine if a stable limit cycle is reached at step n, we require that the norm be less than our threshold for the 4 previous consecutive strides to differentiate stable limit cycles from chaotic gaits:

$$\varepsilon_{TD}(n-i) < 1 \times 10^{-4} \quad \forall i \in [0,3]. \tag{4.21}$$

In addition, we define a chaotic gait to be one in which the robot reaches the maximum simulation time (corresponding to approximately 1000 strides) without reaching a stable limit cycle or violating a failure condition.

4.2 Simulation Results

There are three key parameters for wing-assisted locomotion: linear leg stiffness, torsional leg stiffness, and leg/wing phasing. All of these parameters show a complex interaction in enabling fast and stable locomotion. To examine the effects of each parameter in detail, we vary a single parameter while holding the remaining parameters constant at the nominal values given in Table 4.2. The parameters in Table 4.2 were determined by measuring the leg stiffnesses and leg/wing phase offset for BOLT (as shown in section 3.2), and are highlighted with a solid gray bar in each figure. Examining the effects of each parameter can provide insights towards improving the design of BOLT in future iterations.

We also look at two control cases: legs-only and constant-wings. In the legs-only case we set the wing force to zero. For the constant-wing case, the wing force is equal to the DC component of the wing model. This allows the investigation of any benefits or drawbacks from using flapping wings as compared to a propeller-type propulsive force paired with an airplane wing.

4.2.1 Independent Parameter Analysis

To examine the effect of different parameters on the performance, we examine four different metrics. First, we look at a bifurcation diagram of the touchdown angle, providing a visual representation of the periodicity and stability of the gait. The second metric we examine is the mean translational velocity over four strides. The velocity is taken over multiple strides to account for chaotic gaits that may have slightly different velocities from stride to stride.

The third indicator of performance we consider is the magnitudes of the eigenvalues of the linearized Poincaré return map. The Poincaré map is defined as

$$\mathbf{P} : S \rightarrow S, \tag{4.22}$$

where S is the section defined in Equation 4.18. We compute the Jacobian of the map

$$J_{\mathbf{x}}\mathbf{P}(\mathbf{x}) = \frac{\partial \mathbf{P}(\mathbf{x})}{\partial \mathbf{x}} \tag{4.23}$$

using a central finite-difference method. This gives the k^{th} column of the Jacobian to be

$$\frac{\partial \mathbf{P}(\mathbf{x})}{\partial x_k} = \frac{\mathbf{P}(\mathbf{x} + \delta \mathbf{x_k}) - \mathbf{P}(\mathbf{x} - \delta x_k)}{2\delta x_k}, \tag{4.24}$$

where $\mathbf{x_k}$ is a column vector with the value of the k^{th} state at foot 1 touchdown at row k and zero elsewhere, and δ is a small number. For our calculation, we set $\delta = 0.05$

Finally, a traditional metric for SLIP-like systems is the nondimensionalized relative leg stiffness,

$$k_{rel} = \frac{\frac{F_{vert}}{mg}}{\frac{\Delta l}{l}}, \tag{4.25}$$

where F_{vert} is the maximum normal force due to the legs, mg is the weight of the model, Δl is the maximum change in COM height, and l is the nominal leg length. It is important to note that this stiffness value does not correspond to an actual structural spring in the model (such as the torsional and linear leg springs). The relative leg stiffness represents a virtual spring value that relates the vertical oscillations of the COM to the ground reaction forces. It effectively seeks to collapse all of the forces acting on the system to a single spring value that can explain the motion and ground reaction forces of the system. This value has been found to be $\sim$10 for a wide range of both legged robots and animals [7], and may represent a key metric of stable legged locomotion.

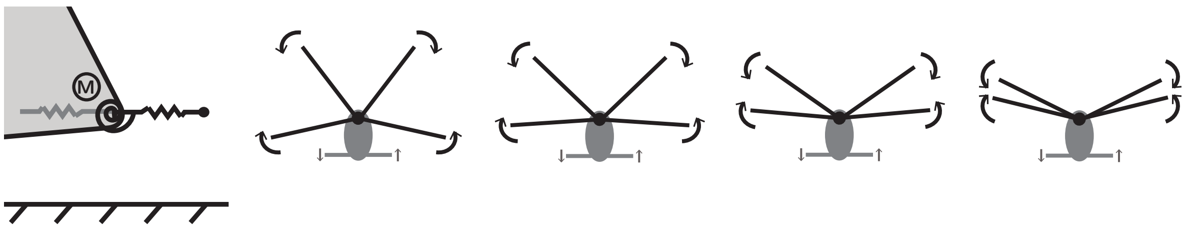

(a) $\theta = -\frac{pi}{2}$ (b) $\theta_{\text{offset}} = 0$ (c) $\theta_{\text{offset}} = \frac{\pi}{4}$ (d) $\theta_{\text{offset}} = \frac{\pi}{2}$ (e) $\theta_{\text{offset}} = \frac{3\pi}{4}$

Figure 4.3: The offset phase (θ_{offset}) between the legs and the wings. By changing the offset phase, the position of the leg within the cycle remains the same (a), while the position of the wings is shifted with respect to the legs (b) - (e).

Leg/Wing Phasing

The first model parameter we investigate is the phase offset between the legs and the wings (θ_{offset}). This parameter determines the relationship between the commanded leg angle and commanded wing stroke position. Figure 4.3 shows the robot at several different phase offset angles. In each image, the leg is pointed directly forward ($\theta = -\frac{\pi}{2}$), while the position of the wing stroke is varied from the beginning of the closing stroke to the end of the closing stroke. Since we model the opening and closing stroke of the wing as equivalent, and the robot has two identical legs, $\theta_{\text{offset}} = \theta_{\text{offset}} + \pi$.

Figure 4.4 shows the results of varying the leg/wing phase offset from 0 to π radians for leg frequencies of 9 Hz and 12.5 Hz. From Figure 4.4, it is clear that the model performs significantly better at 12.5 Hz compared with 9 Hz. At 12.5 Hz, a stable limit cycle exists for 0.44 rad $\leq \theta_{\text{offset}} \leq$ 2.36 rad. Chaotic gaits are found at the edges of the stable region, with unstable gaits outside of 0.35 rad $< \theta_{\text{offset}} <$ 2.62 rad. The range of phases for which stable period-1 gaits can be found at 9 Hz ranges from 1.05 rad $\leq \theta_{\text{offset}} \leq$ 1.92 rad. As in the 12.5 Hz case, at the edges of the stable region the model exhibits chaotic or higher period gaits before becoming unstable.

Using the average translational velocity as a metric, the optimal leg/wing phase offset is found at 0.96 rad for a frequency of 12.5 Hz. At this phase offset, the translational velocity is nearly 2 ms^{-1} at the 12.5 Hz motor frequency. While this is the best phase for a 12.5 Hz motor frequency, it is at the edge of the stable regime for the 9 Hz frequency. At this point, the simulation exhibits a period-2 gait, with the right and left legs no longer symmetrical, as shown by the different touchdown angles in Figure 4.4.

Examining the eigenvalues of the system shows 3 different magnitudes for each simulation, corresponding to one real eigenvalue and 2 complex conjugate pairs. One conjugate pair remains at zero across all phase offset values, while the other conjugate pair is near the stability limit of 1. The second conjugate pair becomes more stable as the phasing is shifted towards the lower edge of the stable region for the phase offset before quickly increasing back towards 1 and becoming unstable. While this value becomes more stable as the phase offset is reduced, the real eigenvalue is increased towards the stability limit. The effect of this increase in response to a disturbance is discussed further in subsection 4.2.3.

Examining the relative leg stiffness (Equation 4.25) shows for a 12.5 Hz motor frequency at the optimal phase offset (as measured by maximum translational velocity), the relative leg stiffness is very near the value of 10 found across other SLIP systems. For example, at $\theta_{\text{offset}} = 1.05$ rad, the maximum vertical leg force, F_{vert}, is 0.0426 N, and the COM vertical displacement, Δl, is 5.75×10^{-4} m. After normalizing by the weight of the model ($mg = (0.012\text{ kg})(9.81\text{ ms}^{-2})$) and the leg length ($l = .020$ m), we find the relative leg stiffness, k_{rel}, has a value of 12.6. As the leg/wing phasing is varied from this value, the relative leg stiffness increases and the simulation eventually becomes unstable. At 9 Hz, the relative leg stiffness remains nearly constant over the stable range. The difference in variation in relative leg stiffness between frequencies is due to the increased wing forces at 12.5 Hz compared with 9 Hz. The higher wing forces at 12.5 Hz have a greater effect on the system, causing the phasing of the legs and wings to have a larger impact on the relative leg stiffness.

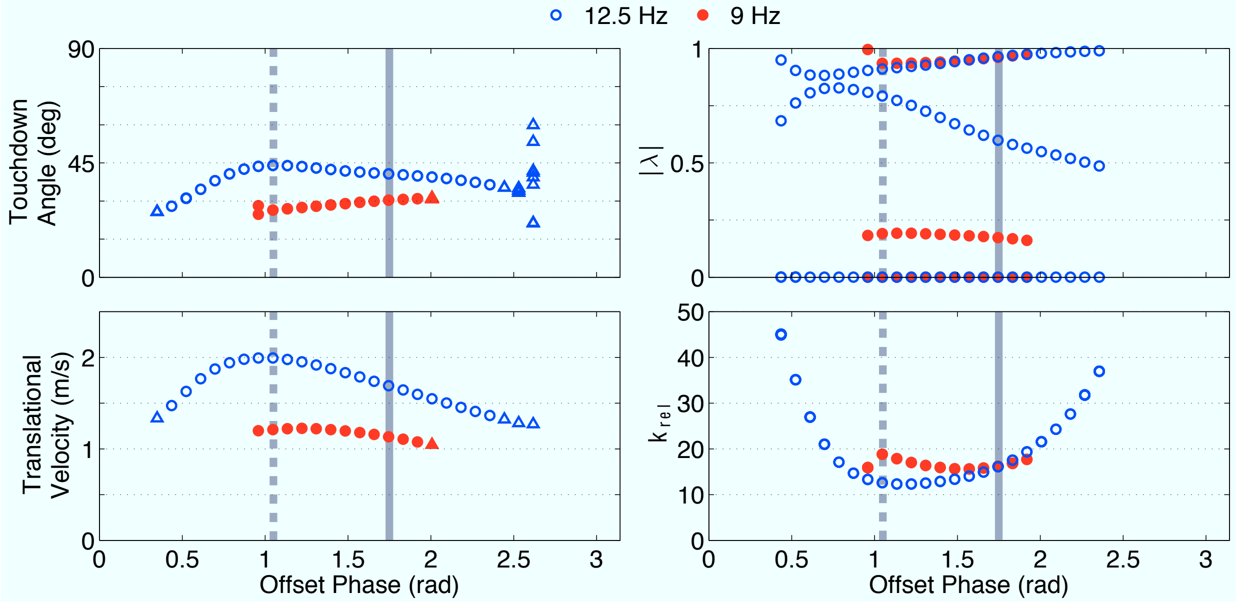

Figure 4.4: The effect of the leg/wing offset phase (θ_{offset}) on the simulation performance, with all other parameters equal to their value in Table 4.2. Circles represent simulations which converged to stable limit cycles, while the triangles represent chaotic trials. At the top left is a bifurcation diagram showing the phase between the leg and the ground at touchdown for four consecutive touchdown events of each foot. The average translational velocity is shown in the bottom left plot, with the magnitude of the eigenvalues of the linearized Poincaré return map for the stable simulations shown on the top right. The bottom right plot shows the value of the relative leg stiffness. The solid gray bar denotes the nominal value for θ_{offset} from Table 4.2. The performance of the simulation with the values marked by both the solid and dashed gray bar are shown in more detail in following sections.

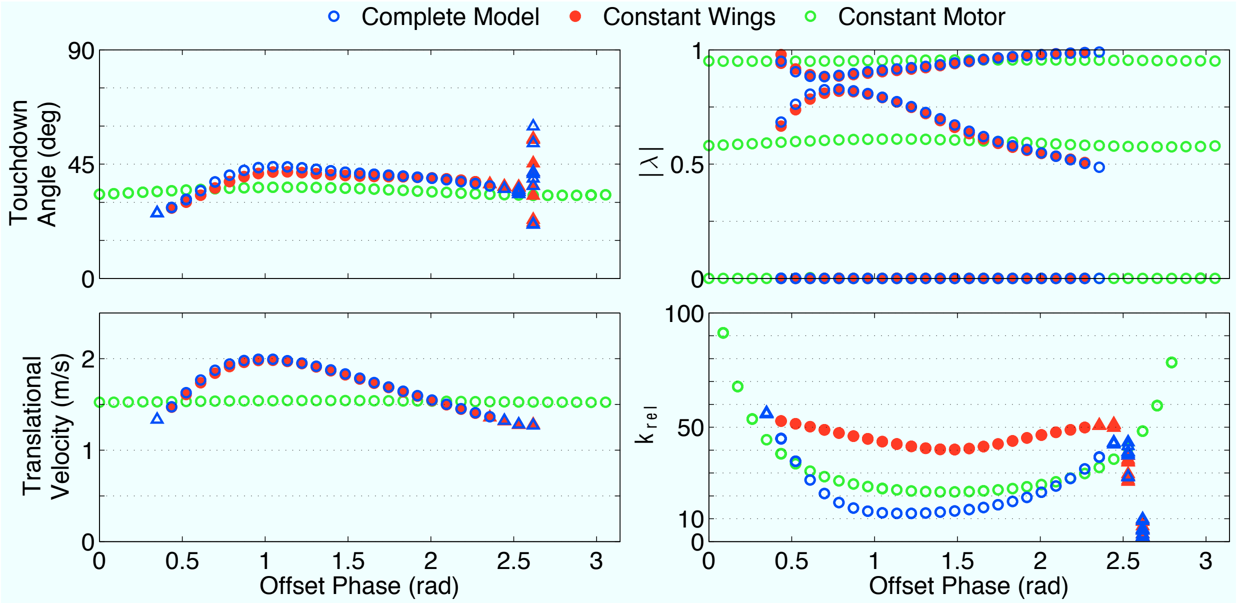

Figure 4.5: Effect of motor, wing, and leg phasing on performance. The complete WingSLIP model includes the induced oscillation of the motor velocity due to the wing loading. While intrinsically coupled in the physical system, in the simulation they can be artificially decoupled. The blue points represent the complete model, the red points represent the model with constant wing force and periodic motor velocity, and the green points represent the model with periodic wing forces and constant motor velocity. Circles represent simulations which converged to stable limit cycles, while the triangles represent chaotic trials. At the top left is a bifurcation diagram showing the phase between the leg and the ground at touchdown for four consecutive touchdown events of each foot. The average translational velocity is shown in the bottom left plot, with the magnitude of the eigenvalues of the linearized Poincaré return map for the stable simulations shown on the top right. The bottom right plot shows the value of the relative leg stiffness. The solid gray bar denotes the nominal value for θ_{offset} from Table 4.2.

Motor Oscillation Effect

Changing the offset phase between the legs and the wings not only changes the phase of the wing force with respect to the legs, it also affects the phase of the oscillation in motor velocity. As discussed in subsection 4.1.4, the loading from the wings on the motor causes the velocity of the motor to oscillate with the wings. While this effect is coupled in the physical system due to actuator limits, it is possible to decouple the effect in simulation and examine the performance. Figure 4.5 shows three different cases: the complete model, with both wing and motor oscillations; a constant wing model, with constant wing forces and periodic motor velocity; and a constant motor model, with periodic wing forces and constant motor velocity.

Examining the constant motor model shows that the periodic wing forces have very little effect on both the stability and translational velocity of the system, suggesting that their effect on these metrics is filtered out by the dynamics of the system. It is clear that the phasing effect seen in the complete model is caused primarily by the periodic motor velocity. As mentioned in subsection 4.1.4, the periodic motor velocity functions as a Buehler clock [59], a feature which was found to be key to the stability of RHex. An important difference is found between the Beuhler clock implemented on RHex and the WingSLIP model. On RHex, the leg is moved quickly through its swing phase, and moved more slowly when on the ground. By contrast, the WingSLIP model performs best when the motor is moved quickly through the stance phase, and moved more slowly though the swing phase. This difference is due to the added force on the system provided by the wings. The wing force propels the robot faster than the leg forces alone. Due to the faster translational velocity of the model, the performance is best when the leg is moving faster during the stance phase, so as to prevent the legs from slowing the motion of the robot.

An effect due to the periodic wing forces is seen in the relative leg stiffness. With the constant wing forces, the relative leg stiffness is fairly high, with a value near 50 across all stable values for the offset phase. The addition of the wing forces with the proper phasing reduces the forces due to the legs, correspondingly reducing the relative leg stiffness.

Leg Stiffness

In addition to the leg/wing phasing, the linear and torsional leg stiffness also have a large effect on the performance of the simulation, and designing and tuning these values correctly is critical to an efficient, high-performance system. The performance of the model as the linear stiffness is varied is shown in Figure 4.6. As with the leg/wing phase, the system is stable over a narrower range for a motor frequency of 9 Hz compared to 12.5 Hz. At 12.5 Hz, the simulation converges to a stable limit cycle for 1.3 N/m $\leq k_s \leq$ 66 N/m. Below $k_s = 1.3$ N/m, the system exhibits chaotic behavior, with the variation in touchdown angle slowly growing until the system becomes unstable at $k_s < 0.2$ N/m. At 9 Hz, a stable limit cycle is found for a significantly smaller range of values, 4 N/m $\leq k_s \leq$ 20 N/m. Figure 4.6 shows that the translational velocity of the model is moderately improved by increasing the leg stiffness for 12.5 Hz running, while the speed remains nearly constant (only changing by 0.1 ms^{-1}) for a motor frequency of 9 Hz.

While increasing the linear stiffness can increase the translational velocity of the system, it is accompanied by an increase in one of the system eigenvalues. As with the leg/wing offset phase, increasing the velocity of the system also reduces the stability of one eigenvalue of the system. Examining the relative leg stiffness, we see that for linear stiffness values that lead to stable limit cycles, the relative leg stiffness varies from $\sim$15 to $\sim$20, increasing as the linear stiffness is moved closer to the edge of the stable region.

The torsional stiffness also has a significant impact on the model's performance, as shown by Figure 4.7. At 12.5 Hz, a stable limit cycle is reached for 0.0006 Nm/rad $\leq k_\tau \leq$ 0.005 Nm/rad. At a motor frequency of 9 Hz, the stable range is only slightly smaller, 0.001 Nm/rad $\leq k_\tau \leq$ 0.004 Nm/rad. At 9 Hz, the system only has a very small region of chaotic behavior before becoming unstable. However, at 12.5 Hz, the simulation shows large regions of chaotic behavior between the stable and unstable boundaries. While variation in the leg/wing phase and linear leg stiffness exhibited chaotic regions, the stride-to-stride variation was fairly small. However, as the

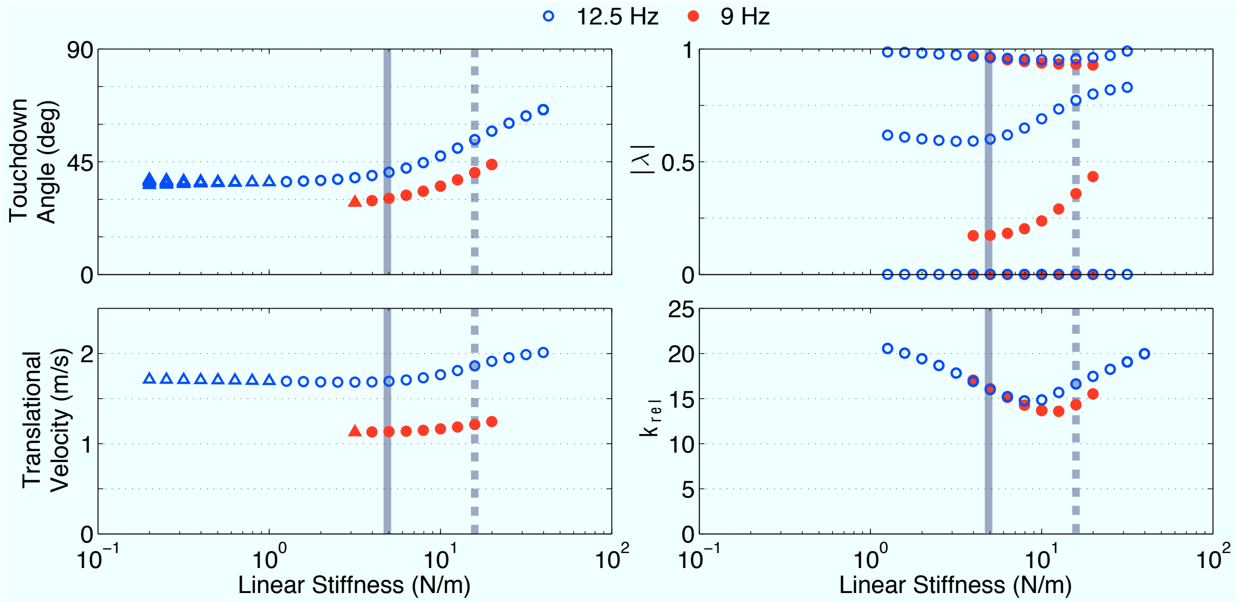

Figure 4.6: The effect of the linear leg stiffness (k_s) on the simulation performance, with all other parameters equal to their value in Table 4.2. Circles represent simulations which converged to stable limit cycles, while the triangles represent chaotic trials. At the top left is a bifurcation diagram showing the phase between the leg and the ground at touchdown for four consecutive touchdown events of each foot. The average translational velocity is shown in the bottom left plot, with the magnitude of the eigenvalues of the linearized Poincaré return map for the stable simulations shown on the top right. The bottom right plot shows the value of the relative leg stiffness. The solid gray bar denotes the nominal value for k_s from Table 4.2. The performance of the simulation with the values marked by both the solid and dashed gray bar are shown in more detail in following sections.

torsional stiffness is varied outside of the stable region, large changes in the touchdown angle of the leg are observed. For higher torsional stiffnesses, the translational velocity is decreased, as the torsional spring is impeding the motion of the robot. Despite the chaotic nature of the gait for torsional stiffnesses below 0.0006 Nm/rad, the translational velocity of the robot does not decrease. This suggests that the legs are providing little propulsive force, with the wings doing the majority of the work. This is also supported by the trend shown by the relative leg stiffness for 12.5 Hz. The relative leg stiffness is proportional to the vertical force from the legs (Equation 4.25). As the torsional stiffness decreases, the relative leg stiffness decreases along with the force from the legs. Conversely, as the torsional stiffness increases, the force from the legs (and relative leg stiffness) also increases.

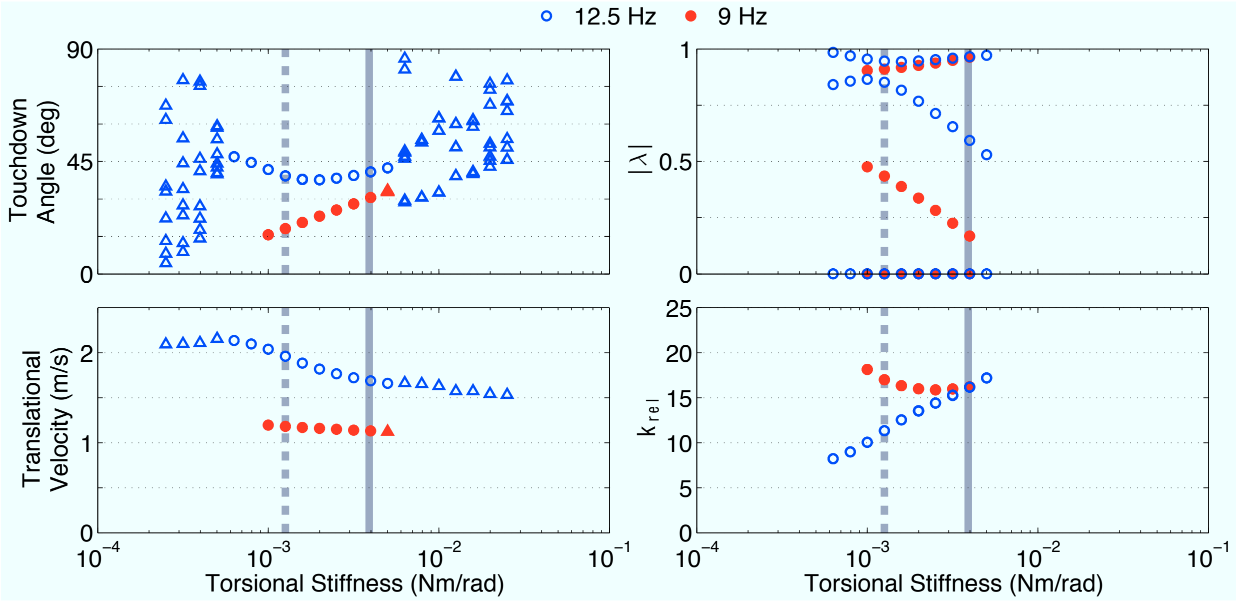

Figure 4.7: The effect of the torsional leg stiffness (k_τ) on the simulation performance, with all other parameters equal to their value in Table 4.2. Circles represent simulations which converged to stable limit cycles, while the triangles represent chaotic trials. At the top left is a bifurcation diagram showing the phase between the leg and the ground at touchdown for four consecutive touchdown events of each foot. The average translational velocity is shown in the bottom left plot, with the magnitude of the eigenvalues of the linearized Poincaré return map for the stable simulations shown on the top right. The bottom right plot shows the value of the relative leg stiffness. The solid gray bar denotes the nominal value for k_τ from Table 4.2. The performance of the simulation with the values marked by both the solid and dashed gray bar are shown in more detail in following sections.

4.2.2 Parameter Interaction and Control Experiments

While studying the effect of each parameter individually can illuminate the effect of that parameter on the performance, the parameters also interact with each other. To investigate this effect, we look at the performance of the WingSLIP model at 12.5 Hz across a grid of leg stiffness values at four different leg/wing offset phase values in Figure 4.8. The simulations clearly elucidate an interaction between the leg/wing offset phase and the torsional leg stiffness. As the torsional leg stiffness is decreased, the effect of the leg/wing offset phase is decreased. With a soft torsional leg spring, the majority of the performance is due to the wing forces, and the phasing with the leg forces does not affect the system. However, as the torsional stiffness is increased, the leg/wing phasing becomes important as the forces from the legs are increased.

Figure 4.8 also shows the performance of two control cases, legs-only and constant-wings. The simulation with leg forces only shows significantly slower translational velocity, as the simulation no longer includes the high propulsive wing forces. In addition, the range of leg stiffnesses over which the simulation is stable is decreased in the legs-only case. When adding wing forces to the simulation, the leg forces become less important and the WingSLIP model can better handle legs that may not be optimally tuned. Investigation of the constant wing simulation shows the effects of the periodic wing forces as compared to a constant force on the model. Much of the benefit due to wings can be achieved by adding a constant propulsive and lift force to the system. However, with the constant wing force, the performance shows significant variation due to leg stiffness (Fig. 4.8b). With properly phased legs and wings, this variation across leg stiffnesses can be reduced with flapping wings (Fig. 4.8d).

4.2.3 Perturbation Response

For each simulation, the eigenvalues consisted of one real value and two conjugate pairs. The lack of damping in the system leads to eigenvalues with a magnitude close to one for each case, as the effect of disturbances can often take an extended period of time to decay. To better understand how the eigenvalues relate to the performance of the system, we look at the COM trajectory of the model for two different disturbances at both 9 and 12.5 Hz across four combinations of model parameters.

Figure 4.9 and Figure 4.10 show the performance of the system when subjected to a 1 mm vertical step at touchdown. In each figure, the nominal case based on the parameters from Table 4.2 is shown at the top, with the following three plots varying the leg/wing offset phase, linear leg stiffness, and torsional leg stiffness, respectively. For the 9 Hz case, we clearly see the effect of the eigenvalues that have magnitude near 1, with the perturbation of the trajectory from the disturbance decaying very slowly. Compared to the nominal case, we see that reducing the torsional stiffness causes the system to stumble and become unstable when subjected to this disturbance. The best performance is seen by increasing the linear stiffness. While reducing the phase offset improves the velocity of the robot, we see here that the lower phase offset exhibits higher oscillations to a step input.

At 12.5 Hz, the performance of the robot is markedly different. All parameter sets are stable for this frequency. However, there is a clear lower frequency oscillation present that decays fairly slowly. Comparing the eigenvalues at 12.5 Hz and 9 Hz in Figure 4.4, Figure 4.6, and Figure 4.7, we see that the model has an eigenvalue near zero and an eigenvalue near 1 at both frequencies. However, the intermediate eigenvalue is significantly greater at 12.5 Hz compared to 9 Hz, leading to the increased low frequency oscillation observed in the step response. At 12.5 Hz, the best performance is achieved by reducing the phase offset to 1.05 rad from 1.75 rad. Increasing the torsional leg stiffness also improves performance at 12.5 Hz, in contrast to its destabilizing effects at 9 Hz. This effect is likely due to the increased influence of the wings at the higher frequency, and correspondingly decreased influence of the leg torsional stiffness.

The second perturbation that is considered is a 20% instantaneous reduction in the translational velocity of the model. This is analogous to an impulse force on the physical system. At 9 Hz, this has very little effect on the system across all parameter combinations. With reduced torsional stiffness, the disturbance is nearly completely rejected, with no change in performance. The system with increased linear stiffness performs nearly as well, with the reduced phase system

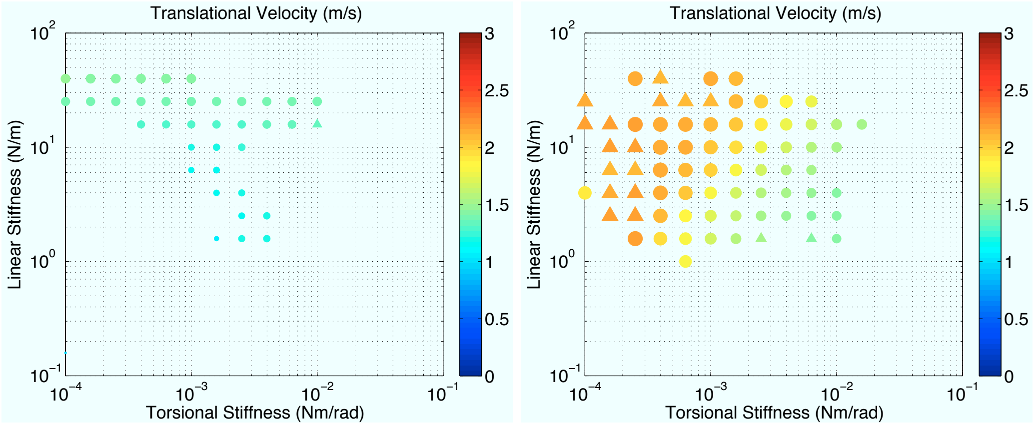

(a) Legs-Only

(b) Constant Wing and Motor

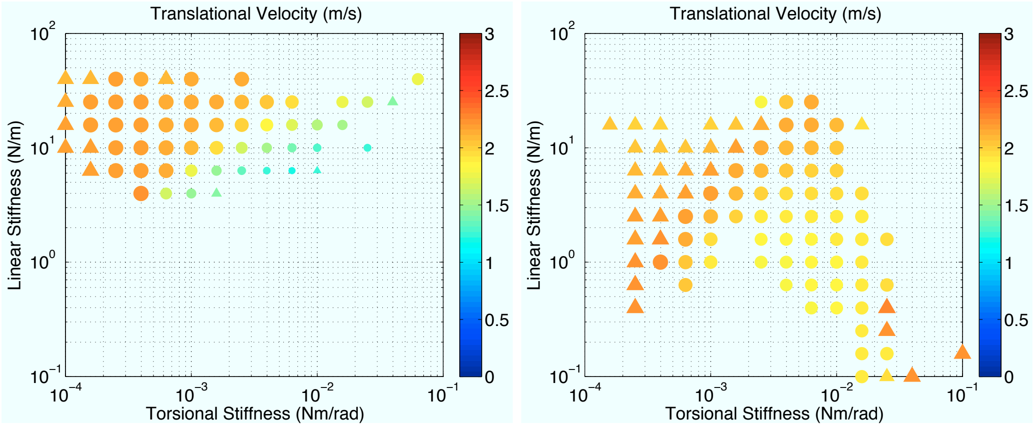

(c) $\theta_{\text{offset}} = 0.17\text{rad}$

(d) $\theta_{\text{offset}} = 0.96\text{rad}$

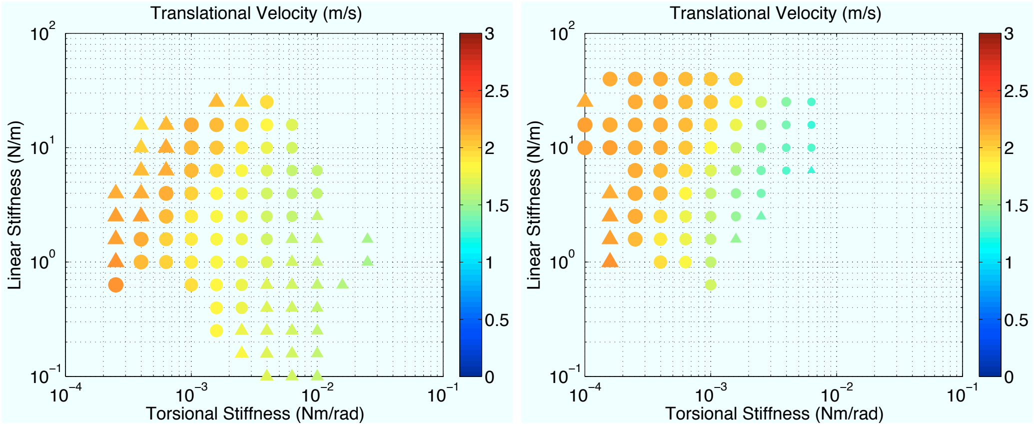

(e) $\theta_{\text{offset}} = 1.75\text{rad}$

(f) $\theta_{\text{offset}} = 2.53\text{rad}$

Figure 4.8: Multi-parameter variation of the parameters of the WingSLIP model and two control cases. (a) shows the performance with leg forces only, while (b) shows the performance with constant wing forces. (c) – (f) shows the performance of the WingSLIP model across a grid of leg stiffnesses for four different leg/wing phase offset values.

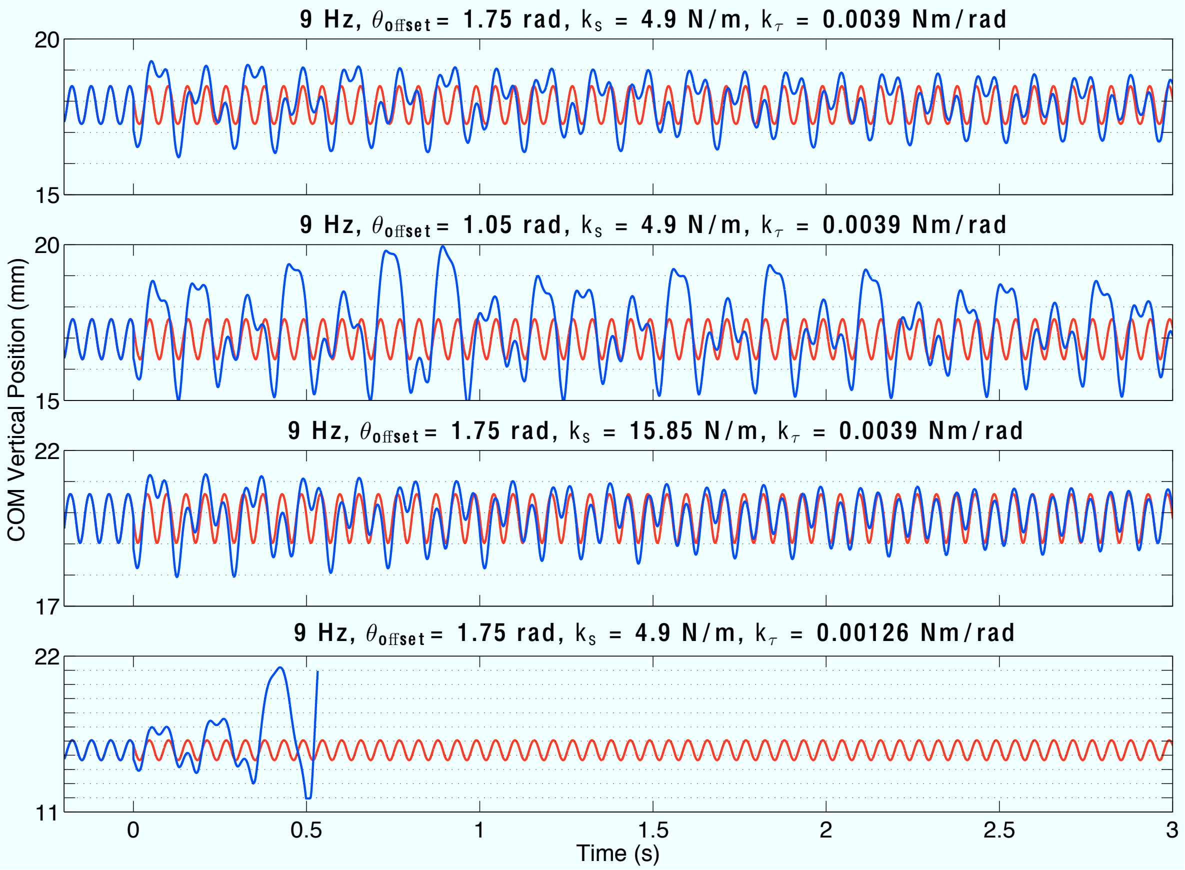

Figure 4.9: COM height for 3 seconds after being subjected to a 1 mm vertical step at $t = 0$ when running at 9 Hz. The red lines show the steady state (limit cycle) trajectory, with the blue lines showing the perturbed trajectory. The results are shown for simulations using four different parameter combinations.

again performing the worst for the 9 Hz motor frequency.

At 12.5 Hz a significantly greater effect is observed. The horizontal velocity of the system is greater at this frequency, and the wing forces depend on the square of the velocity. This leads to a greater observed effect compared to the 9 Hz frequency. For this case, increased linear stiffness shows the best performance, followed by the nominal case. Decreasing the torsional stiffness or the phase offset leads to a higher initial effect from the disturbance and a longer recovery time. Again, the effects of the higher intermediate eigenvalue can be seen in the low frequency oscillations that are not present when running at 9 Hz.

4.2.4 Steady State Performance

In addition to the perturbation response of the system, we are interested in the COM trajectory and forces on the system when it has reached a stable limit cycle. As the parameters of the system are

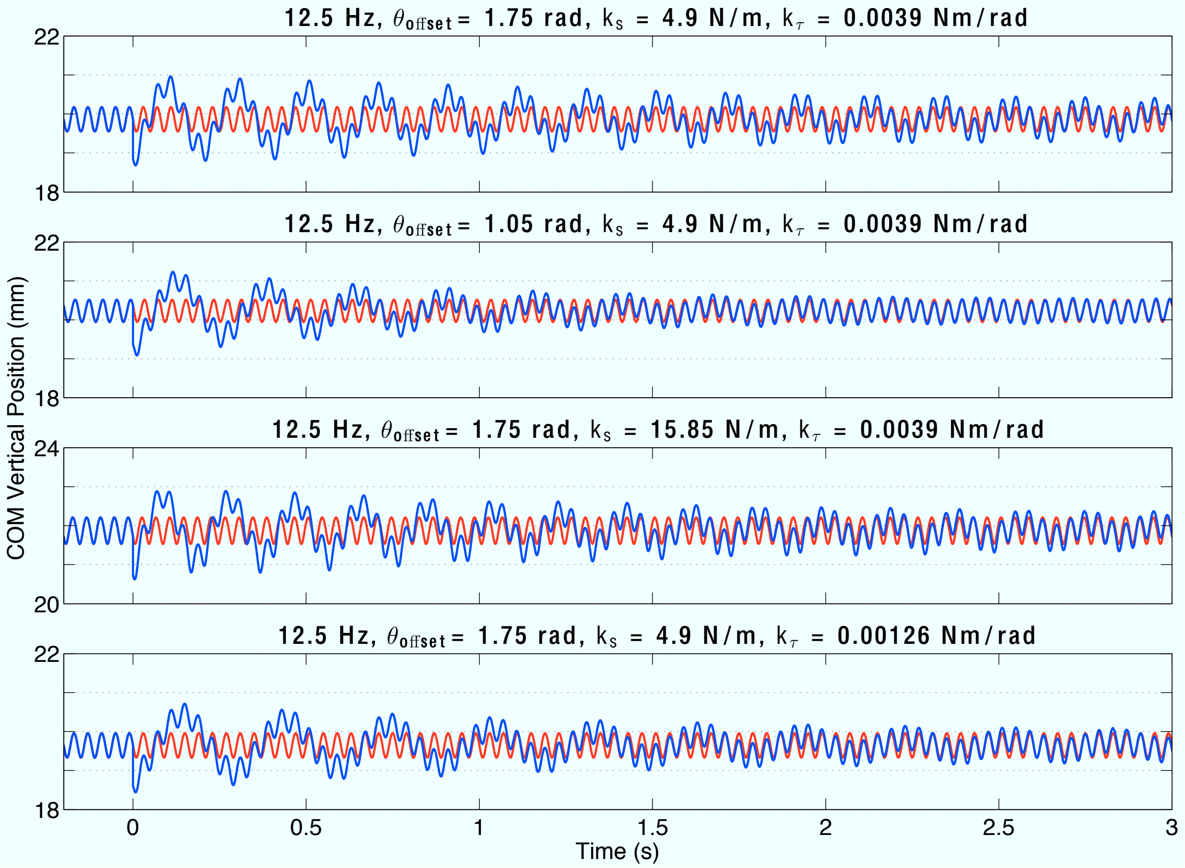

Figure 4.10: COM height for 3 seconds after being subjected to a 1 mm vertical step at $t = 0$ when running at 12.5 Hz. The red lines show the steady state (limit cycle) trajectory, with the blue lines showing the perturbed trajectory. The results are shown for simulations using four different parameter combinations.

varied, the trajectory of the robot in the state space converges to different limit cycles. Analysis of the trajectory and leg forces can suggest the specific effects different parameters have on the system.

The simulation shows that once the model has reached a stable limit cycle, the COM follows a smooth sinusoidal trajectory, similar to the characteristic pattern exhibited by classical SLIP like motion. However, the addition of wing forces introduces several important differences between this model and the standard leg-only models. The fore-aft leg forces for the classical SLIP model have a characteristic sinusoidal shape, with the leg braking the COM forward velocity for the first half of the stride, and accelerating it through the second half of the stride. Due to the additional force provided by the wings, the WingSLIP model runs at a higher velocity than the leg frequency alone would allow. This causes the leg to primarily provide a braking force when on the ground, as the actual leg angle often leads the commanded leg angle.

Figure 4.13 shows several interesting features of WingSLIP locomotion for the parameters from

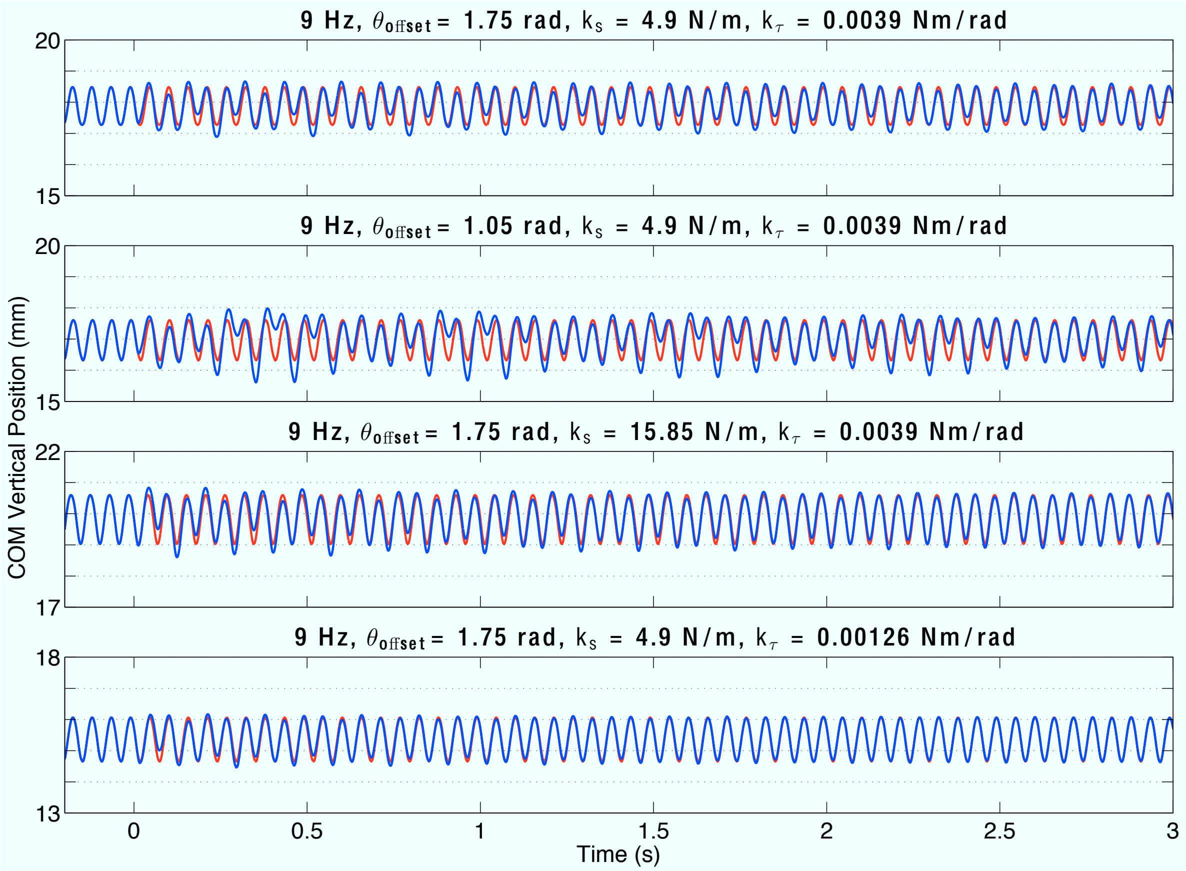

Figure 4.11: COM height for 3 seconds after being subjected to a 20% instantaneous reduction in the translational velocity at $t = 0$ when running at 9 Hz. The red lines show the steady state (limit cycle) trajectory, with the blue lines showing the perturbed trajectory. The results are shown for simulations using four different parameter combinations.

Table 4.2. In SLIP systems, the magnitude of the ground reaction forces generally increases with the stride frequency and translational velocity. However, due to the increase in wing forces with increasing motor frequency, the WingSLIP model shows a reduction in the ground reaction forces. This effect is due to the higher lift force provided by the wings, effectively reducing the mass of the model. An additional effect of the reduced effective mass from wing forces is increased average COM height at higher frequencies, as less leg compression is necessary to support the weight of the system. The COM height also exhibits lower oscillation in the 12.5 Hz case, despite the higher wing forces on the system. This effect is beneficial for mounting obstacles, as seen in Figure 4.10.

Comparing with the nominal case, Figure 4.14 shows the advantage of aligning the wing and leg phase correctly. When aligned such that the leg is moving fastest when in stance phase, the negative horizontal leg force on the system is reduced. While the commanded leg phase still lags the actual leg phase, the difference is reduced and the torsional spring is no longer attempting to slow down the leg as significantly. This leads to the clear improvement in velocity seen in

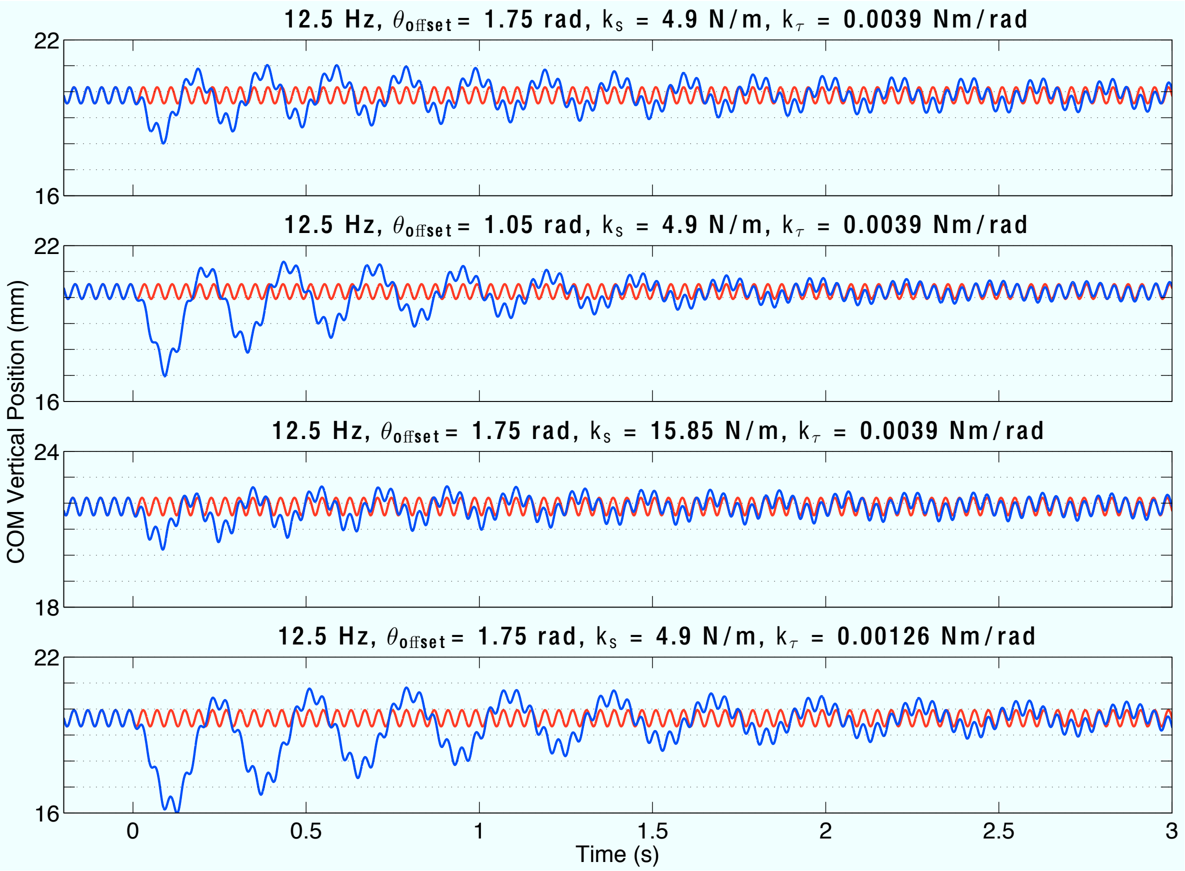

Figure 4.12: COM height for 3 seconds after being subjected to a 20% instantaneous reduction in the translational velocity at $t = 0$ when running at 12.5 Hz. The red lines show the steady state (limit cycle) trajectory, with the blue lines showing the perturbed trajectory. The results are shown for simulations using four different parameter combinations.

Figure 4.4.

Increasing the linear leg stiffness, as Figure 4.15 shows, increases further the COM height during steady state running. It also has the effect of smoothing out the leg forces when compared to the softer leg spring seen in Figure 4.13. The normal leg force exhibits a smooth half-sinusoid during stance, very similar to the characteristic SLIP model. While the fore-aft leg forces still differ from the traditional SLIP model, the more upright posture and reduced stance time minimizes the negative force from the legs. Here, the wings provide the majority of the fore-aft force, with the legs only providing periodic normal force to keep the robot off the ground.

Figure 4.16 shows an alternate way of reducing the fore-aft force from the legs - reducing the torsional leg stiffness. Lowering this stiffness reduces the ability of the motor to transmit forces to the ground through the leg, allowing the wings to accelerate the system without the legs impeding the motion. However, when subjected to a disturbance, the lack of force production from the legs can be catastrophic, and cause the robot to stumble as Figure 4.9 shows.

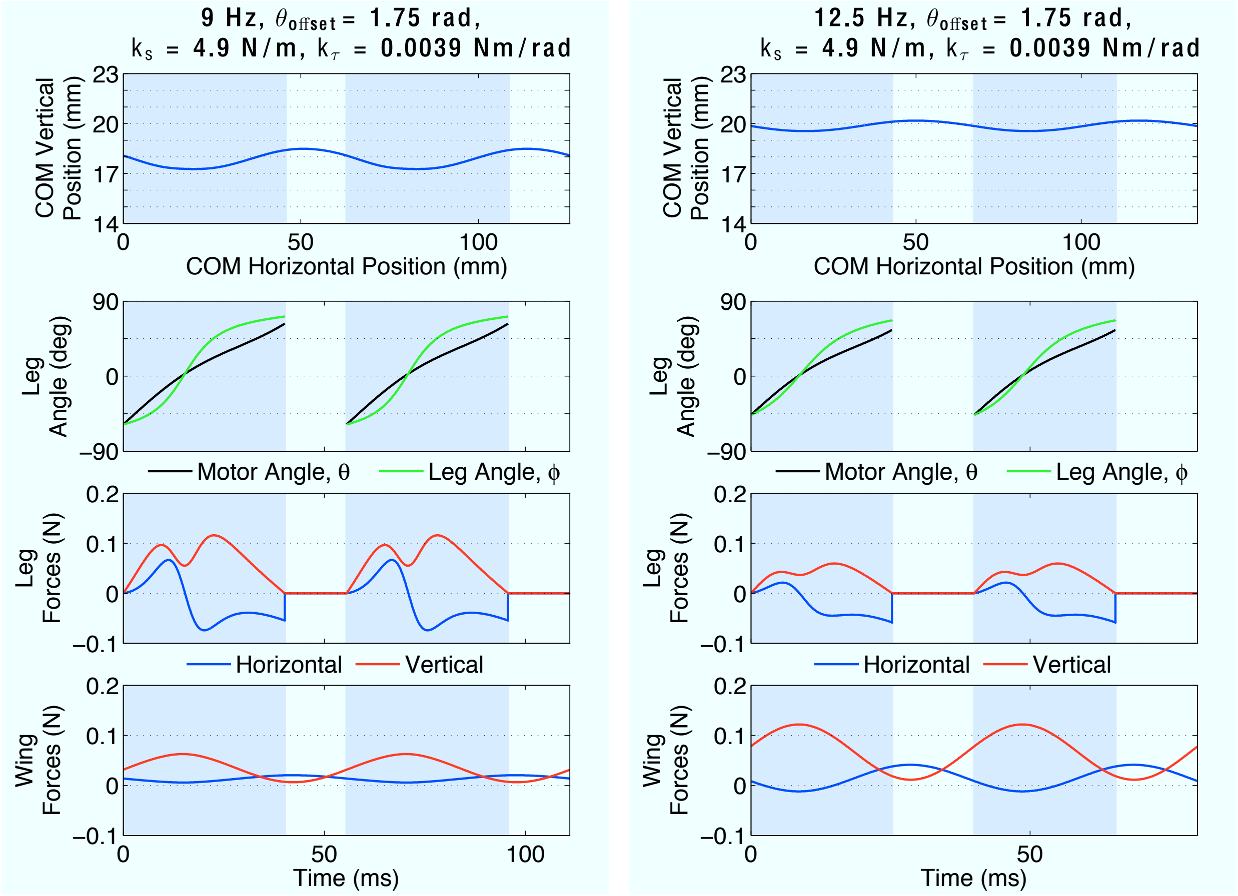

(a) (b)

Figure 4.13: Steady state trajectory and forces for one complete stride of the simulation with the nominal parameter values from Table 4.2. The gray bars denote the stance phase.

4.2.5 Effect of Assumptions and Physical Implications

By definition, all dynamic models are a simplification of the physical system. The canonical SLIP model, while informative about the underlying dynamics of complex systems, is unstable for many actual physical parameters found in both animals and robots [62]. To address this, additional complexity is added to the simple SLIP model through the addition of a clock-torqued control scheme. The goal of the WingSLIP model is to capture enough of the system complexity to inform the effect of different system parameters on the dynamics of the system. Examining the performance of the model at the measured parameter values from the robot, we see that the WingSLIP predicts stable locomotion for these values. This initial test suggests that a reasonable degree of complexity has been included, however more detailed experimental results are necessary to fully validate the model.

While reduced order models sacrifice some accuracy, they allow the effect of the included

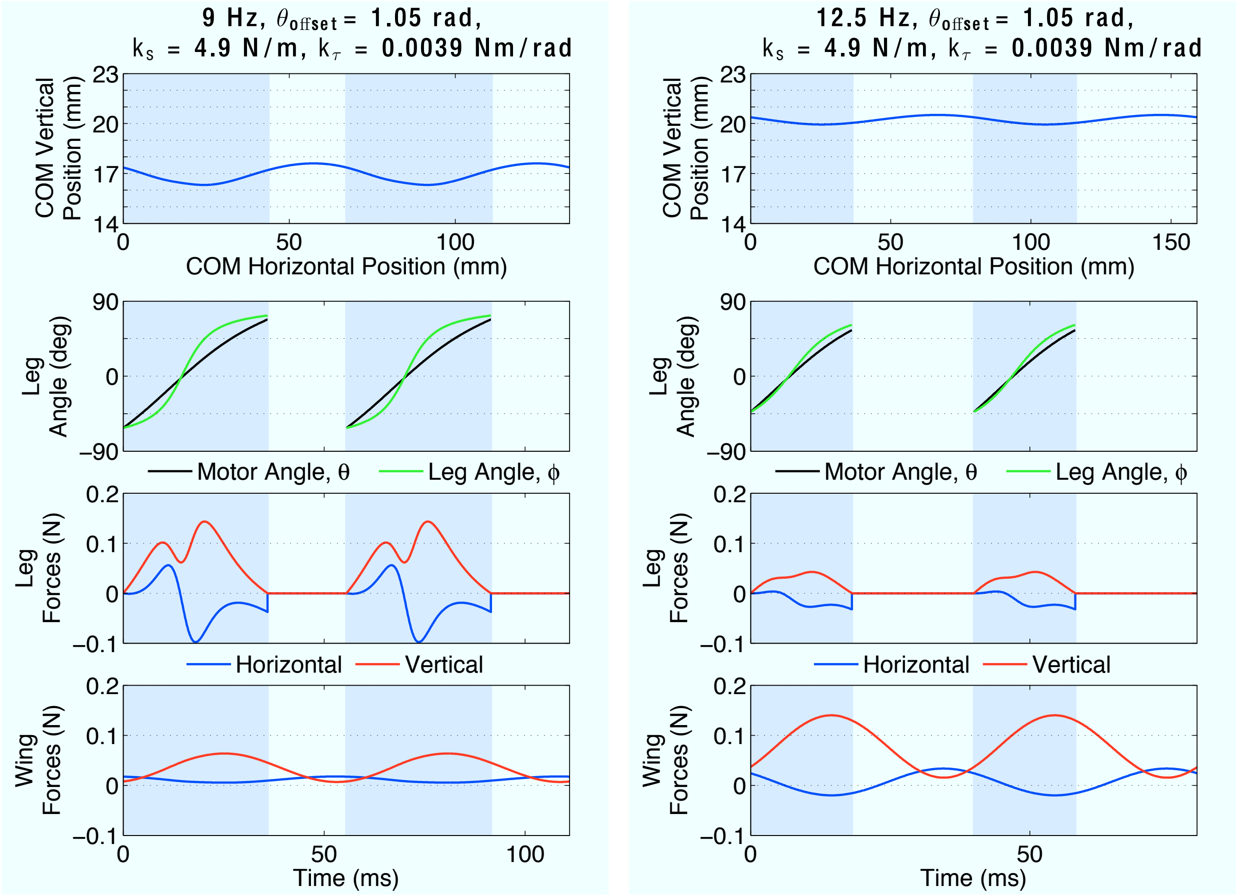

(a) (b)

Figure 4.14: Steady state trajectory and forces for one complete stride of the simulation with a phase offset of 1.05 rad, with the other parameters at their nominal values. The gray bars denote the stance phase.

parameters to be more easily investigated and understood. Higher order models quickly become intractable in the number of parameters included. The WingSLIP model makes several assumptions in order to simplify the understanding of wing assisted locomotion. Both linear and torsional damping are neglected from the leg model. In addition, rotational aerodynamic damping due to the wings is also neglected. The lack of damping in the system is evident by the eigenvalues with a magnitude near one found for all parameter combinations. The addition of damping to the system would likely decrease the eigenvalues of the system, providing a mechanism to remove the energy imparted by a disturbance.

The WingSLIP model also over-predicts the translational velocity of the robot compared with the experimental performance presented in Table 5.2. This is likely due to the effect of friction on the system, which has been neglected in the WingSLIP model. There are two sources of friction

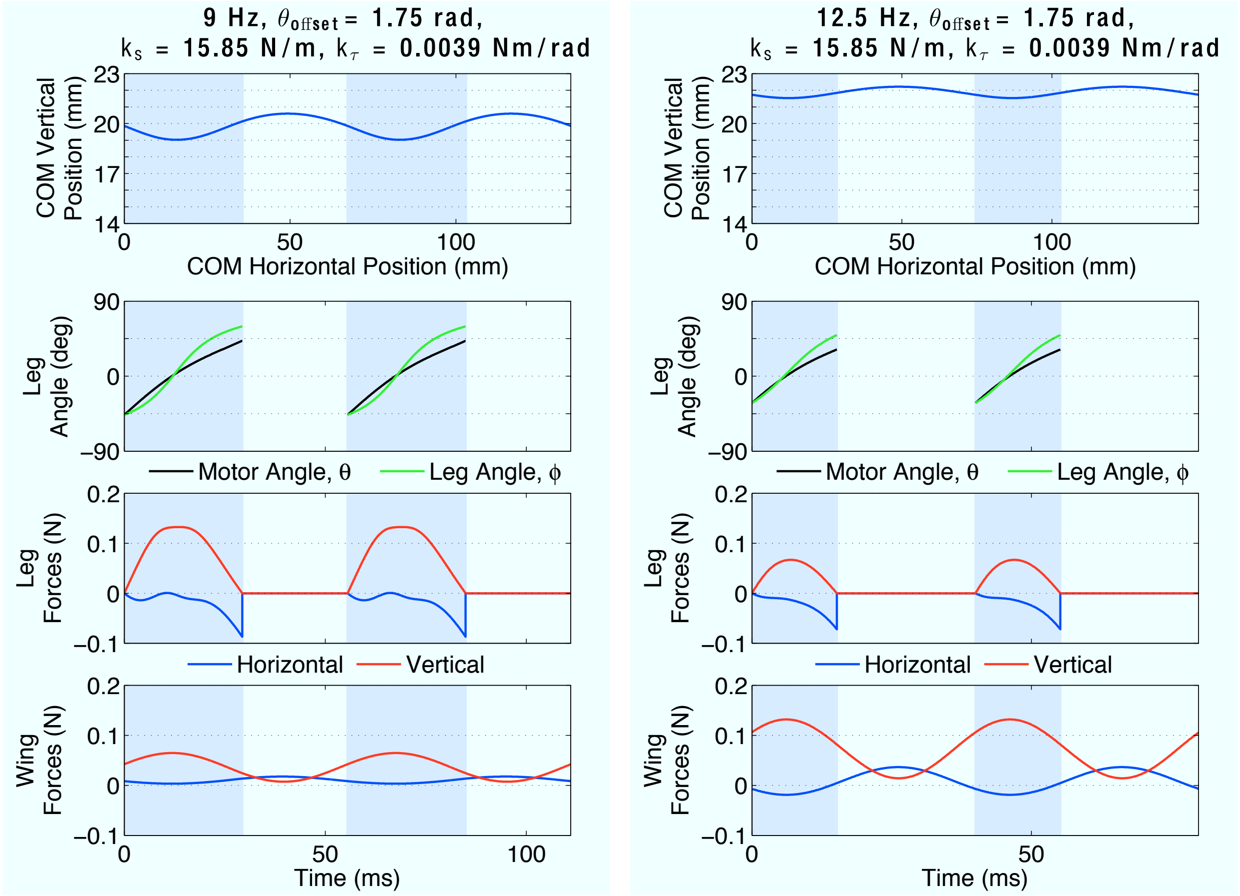

(a) (b)

Figure 4.15: Steady state trajectory and forces for one complete stride of the simulation with an increased linear leg stiffness of 15.85 N/m, with the other parameters at their nominal values. The gray bars denote the stance phase.

in the model, at the foot contact and the tail contact. Inclusion of both static and kinetic friction at the foot would lead to reduced propulsive force from the legs and slower performance. However, the largest effect is likely due to the tail friction. Observations of the performance of BOLT show a complex interaction between the airflow from the flapping wings and the tail. At low flapping frequencies, the tail drags on the ground and significant friction is present. However, at higher frequencies, the airflow from the wings flows between the tail and the ground, effectively creating an air-bearing and reducing the sliding friction on the tail. This leads to the small discrepancy in predicted translational velocity at 12.5 Hz, and the much larger discrepancy at 9 Hz.

The results presented in this section can provide guidelines for increasing the performance of the BOLT platform, however physical constraints must also be considered. While the modeling results suggest that increasing the linear stiffness and decreasing the torsional stiffness would im-

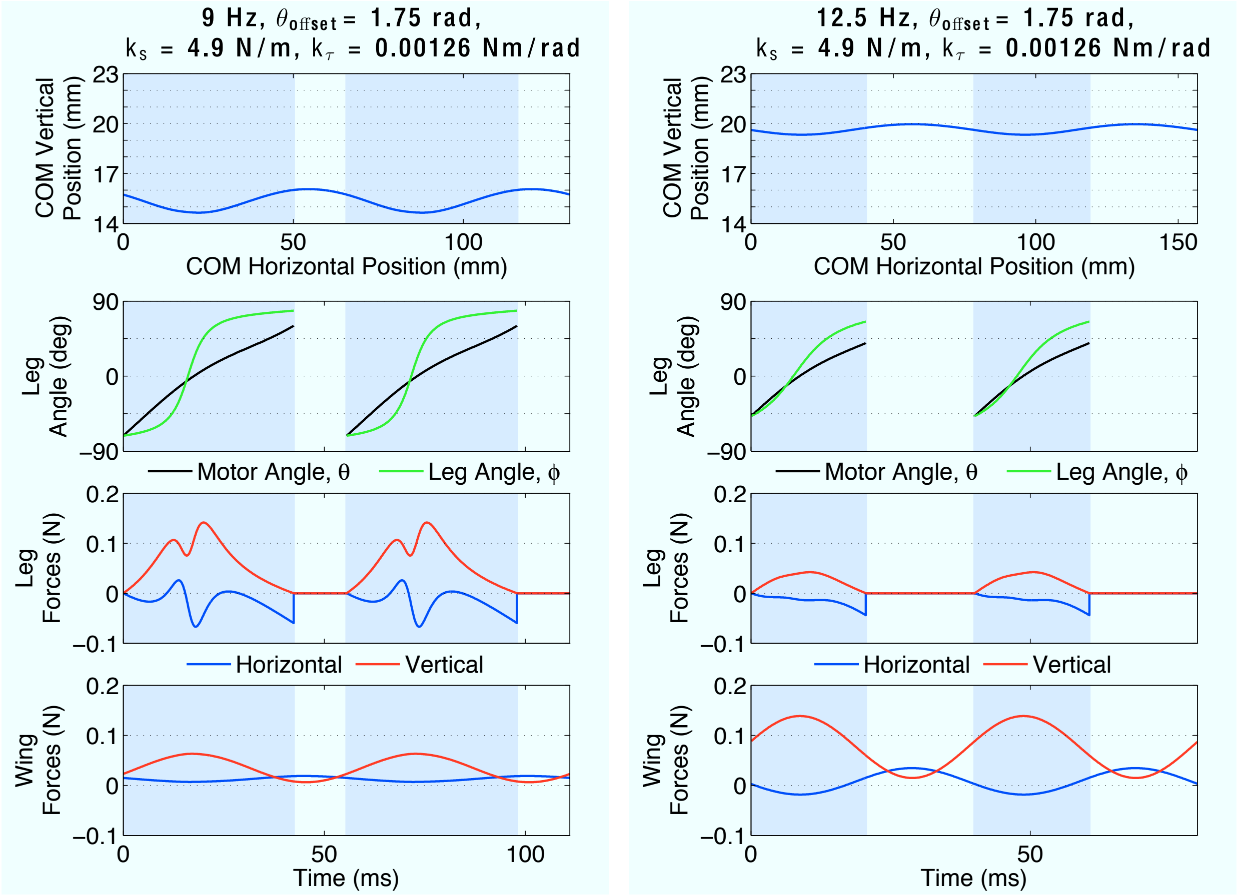

(a) (b)

Figure 4.16: Steady state trajectory and forces for one complete stride of the simulation with a softer torsional leg stiffness of 0.00126 Nm/rad, with the other parameters at their nominal values. The gray bars denote the stance phase.

prove performance, this is difficult to do in reality. The leg stiffnesses are coupled through the complex hip mechanism in the physical system, and it is difficult to increase one stiffness while decreasing the other. Future designs that include a decoupled hip mechanism may greatly benefit from this insight however, leading to improved hybrid performance.

Chapter 5

Experimental Characterization of Flapping Wing Aerodynamically Assisted Bipedal Running

5.1 Experimental Dynamics of BOLT

BOLT [56] has two regimes of operation when locomoting terrestrially, a quasi-static gait (9 Hz) and a dynamic gait (12.5 Hz). To study the dynamics in each of these modes, we use the accelerometer to examine the intra-stride forces at steady-state velocity. The rate gyroscope allows the acceleration data to be corrected for the pitch and roll of the body, aligning the acceleration components in the horizontal and vertical directions. We use the maximum velocity obtained by the robot as a relative measure of the maximum effective locomotive force on the robot. The data are parameterized by the output gear phase, obtained by integrating the highly periodic back EMF signal. By performing the tests on carpet, we ensure the legs have good traction with the ground during the trials.

We consider two control cases to distinguish between the force contributions of the flapping wings and the legs when running along the ground. We replace the legs on BOLT with lightweight wheels (Fig. 5.1a) to isolate the effects of the flapping wings (wings-only, WO). In this configuration, the flapping wings supply all of the locomotive force. Removing the linkage driving the wings (Fig. 5.1b) reduces the wings to a passive element with the locomotive force coming entirely from the legs, (wings-passive, WP). This configuration also allows the differentiation between the effects of flapping the wings and the passive properties of the airfoil.

5.1.1 Quasi-static Terrestrial Locomotion

BOLT exhibits a quasi-static walking gait when running at a flapping frequency of 9 Hz. The aerodynamic effects of the flapping wings are minimal in this gait, with the WO robot reaching a maximum velocity of 0.17 ms^{-1}. In contrast, the legs of the WP robot propel it at 0.33 ms^{-1}.

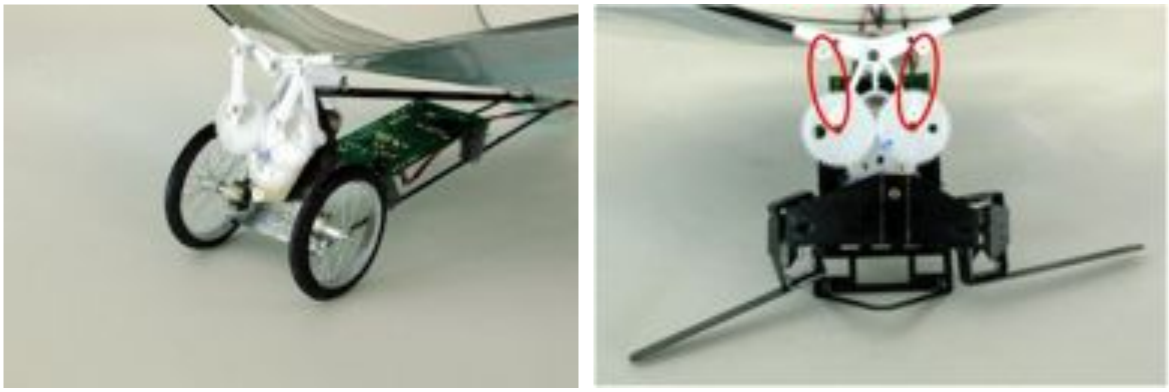

(a) Wings-Only (WO) (b) Wings-Passive (WP)

Figure 5.1: (a) shows the first control case, the robot with wheels instead of legs, allowing the investigation of the wing effects alone. For the second control case (b), we disconnect the linkage driving the wings, removing any active effects from flapping.

Overall, the hybrid robot reaches 0.5 ms^{-1}, suggesting a superposition of the leg and wing thrust components may explain the hybrid gait.

Figure 5.2 shows the fore-aft and vertical accelerations of the robot over a representative cycle. We show the accelerations for the WO robot, the WP robot, the superposition of the WO and WP robots, and the hybrid robot. The accelerations of the hybrid robot are similar in both magnitude and shape to the superposition of the WO and WP robots, suggesting a lower degree of interaction between the leg and wing forces in this gait. An effect of leg/wing force coupling that can be seen is the smoother accelerations of the hybrid robot compared to those the WO+WP model predicts. The flapping wings provide a higher amount of damping on the impulsive leg forces the robot generates than the passive wings.

The motor velocity over a representative cycle of the quasi-static gait is shown in Figure 5.3. The robot uses constant PWM control for the motor, causing the motor velocity to vary depending upon load. Over a single cycle, the effect of the varying load due to the flapping wings or legs is seen clearly from the change in motor velocity. The variation in motor velocity for the hybrid robot and the WO robot is nearly identical, implying a similar load in the two cases. Thus, despite the wings' ineffectiveness in this gait they are responsible for the majority of the power consumption of the motor. Table 5.1 shows the WO robot consumes 80% more power than the WP robot despite traveling at only half the speed. This is reflected by the cost of transport: the WP robot is the most efficient while the WO robot is the least efficient. The hybrid robot has an efficiency between the two controls.

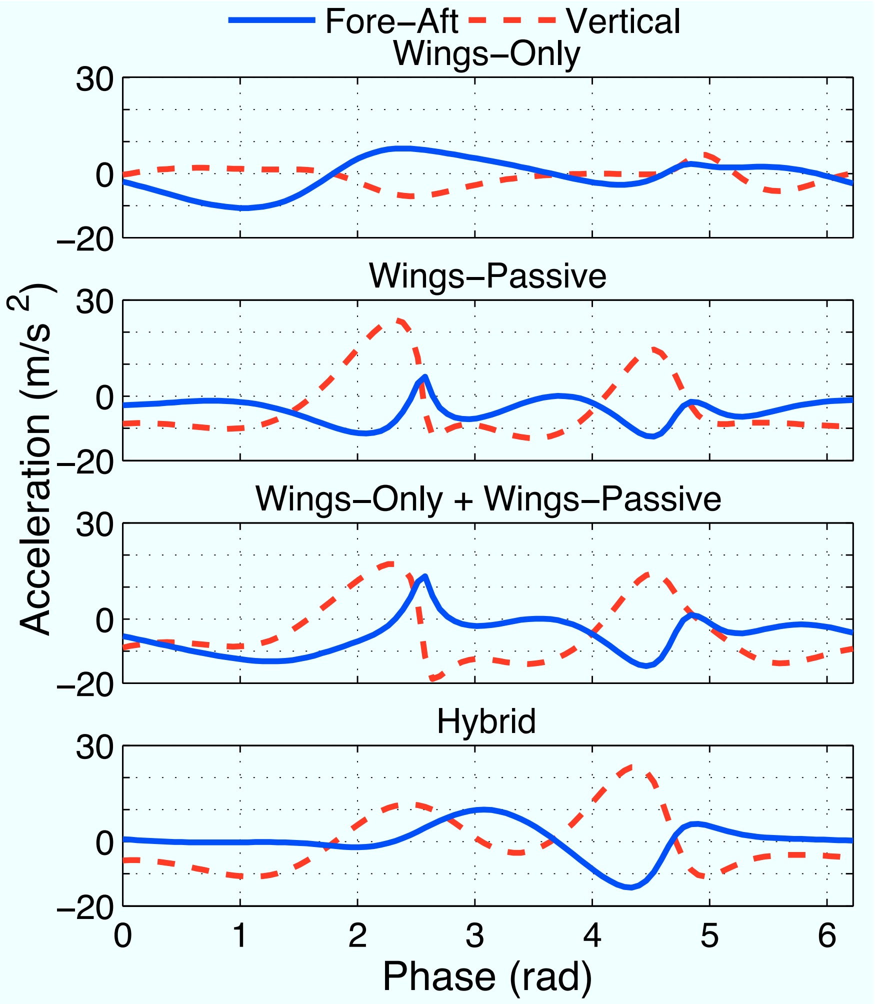

Figure 5.2: Fore-aft and vertical accelerations shown over a single representative cycle when running at 9 Hz at a steady state velocity. At slow frequencies the robot exhibits quasi-static motion. In this regime, the forces on the hybrid robot are consistent with the superposition model of the individual leg and wing forces.

Table 5.1: Forward velocity (ms^{-1}), motor input power (W), and specific resistance of different configurations and gaits for BOLT.

Gait (frequency)		Configuration		
		Wings-Passive	Wings-Only	Hybrid
Quasi-static (9 Hz)	Velocity	0.33	0.17	0.50
	Power	0.36	0.65	0.89
	SR	9.87	34.4	15.9
Dynamic (12.5 Hz)	Velocity	0.35	1.5	1.5
	Power	0.36	0.79	0.91
	SR	9.14	4.68	5.51

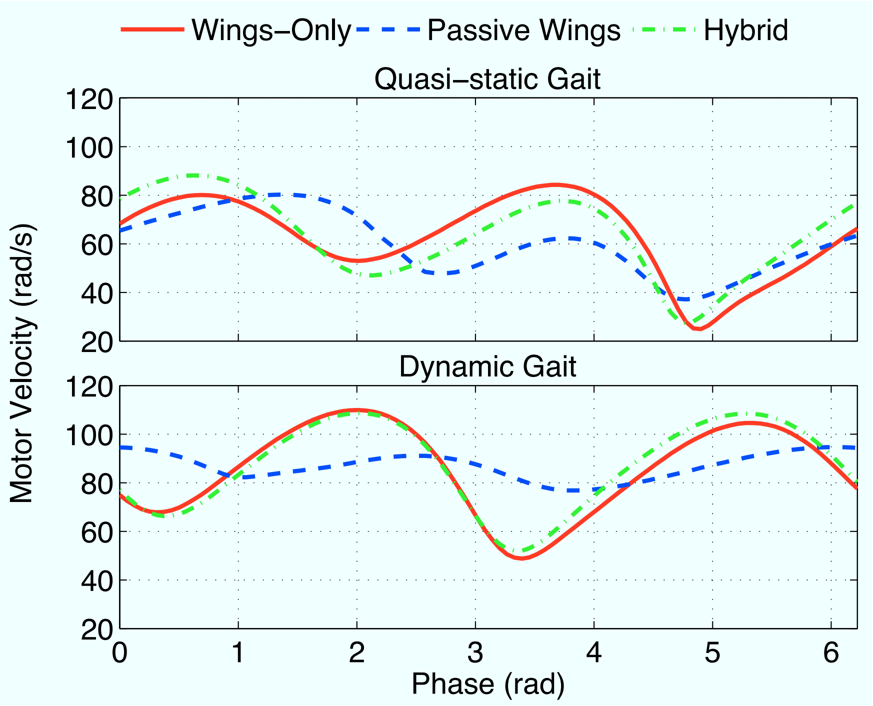

Figure 5.3: Motor velocity over a representative cycle for both a quasi-static gait (9 Hz) and a dynamic gait (12.5 Hz).

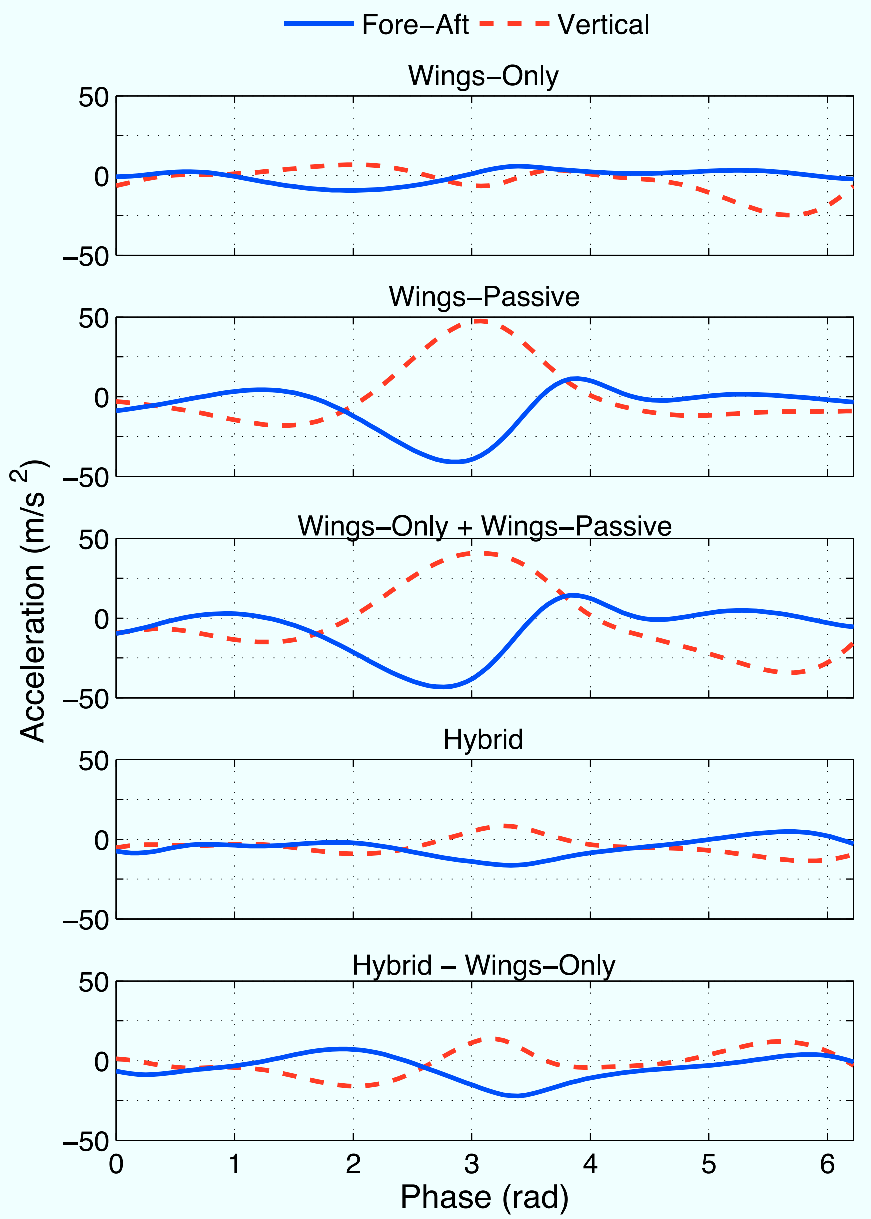

Figure 5.4: Fore-aft and vertical accelerations shown over a single representative cycle when running at 12.5 Hz. At high speeds, a simple superposition of the leg and wing forces does not accurately predict the overall force on BOLT. The interactions between the legs and the wings are an important component of the forces during dynamic locomotion, altering the range of leg stiffnesses that give stable locomotion.

5.1.2 Dynamic Locomotion

The second running gait of BOLT is dynamic bipedal locomotion, seen at a flapping frequency of 12.5 Hz. The aerodynamic force the flapping wings provide increases greatly, with the WO robot running at 1.5 ms^{-1}. The hybrid robot also runs at 1.5 ms^{-1}, while the WP robot is only capable of 0.35 ms^{-1}. In this gait, there is a strong interaction between the wing and leg dynamics.

The acceleration plots of Figure 5.4 show the same four cases as above (WO, WP, WO+WP, Hybrid), along with a fifth case: the WO case subtracted from the hybrid case. For this gait, the WO+WP model is a poor predictor of the hybrid accelerations, predicting magnitudes over double the measured values.

The WP case shows one overly large single acceleration caused by a footfall centered at a phase of π, propelling the robot into the air preventing the next footfall from generating the same amount of force. Between footfalls, the robot is in free-fall, with zero fore-aft acceleration, and a vertical acceleration of -9.8 $\mathrm{m/s}^2$. The high accelerations and gait asymmetry of the WP case are generally indicative of poor leg tuning on a robot with a traditional SLIP gait. The hybrid robot uses the same legs as the WP robot at the same frequency, but the accelerations experienced by the robot are much lower. We again see the effect of the flapping wings damping the leg impulses from the quasi-static case, but to a higher degree now. The hybrid robot does not have the free-fall state shown by the WP robot; stopping this free-fall leads to the high accelerations seen in the WP case. The hybrid robot is “flying between footfalls” instead of falling, greatly reducing the accelerations that must be affected by the legs.

The WO robot and the hybrid robot both run at the same forward velocity and motor frequency (see Figure 5.3). This leads to the assumption that the wing forces are nearly the same in both cases regardless of the ground contacts. Subtracting the WO case from the hybrid case shows the leg forces for the hybrid robot (Figure 5.4). While they still differ from a traditional SLIP gait due to the leg/wing interactions, the legs no longer appear poorly tuned. From this data, we conclude a flapping wing robot should use stiffer legs than would normally be expected for a robot running with legs alone.

The motor velocities, and thus the dynamic loading, are nearly identical between the hybrid robot and the WO robot during the dynamic gait (Figure 5.3). As in the quasi-static case, the WP robot uses the least amount of power, followed by the WO robot with the hybrid robot consuming the most power (see Table 5.1). Due to the differing forward speeds, the COT relationship is now markedly different, with the WO case the most efficient and the WP case the least efficient. Once again, the hybrid provides a compromise between the cases.

5.1.3 Rotational Energy Analysis

To further analyze the locomotion of the two gaits, we apply the analysis presented in section 6.1 and look at the mean rotational energy (Equation 6.5) and mean normalized variance in energy (Equation 6.6). The results are presented in Table 5.2. For both gaits, the WO case has the lowest energy, followed by the hybrid case, with the WP case having the highest rotational energy. The lack of hybrid dynamics in the WO case is the strongest contributor to its low energy state. The

Table 5.2: Mean rotational energy ($\bar{E}_{Rot}$ (J)) and mean normalized variance in energy ($\overline{\hat{\sigma}(E_{Rot})^2}$ (J)) for BOLT

Gait (frequency)		Configuration		
		Wings-Passive	Wings-Only	Hybrid
Quasi-static	Energy	0.5115	0.0449	0.2806
(9 Hz)	Variance	0.3235	0.0209	0.1358
Dynamic	Energy	0.9807	0.2376	0.4476
(12.5 Hz)	Variance	0.8345	0.0483	0.1407

hybrid case has lower rotational energy compared to the WP case, despite the higher power input to the system (Table 5.1). This is consistent with the conclusion that flapping wings provide important damping and stabilization to the system. The WP case has significantly higher mean rotational energy compared to the other two test conditions. This clearly demonstrates that this system is poorly suited for running without the wings. The mean normalized variance is also much higher for the WP case, implying more variability between strides and an inability of the WP robot to reach a stable limit cycle.

The dynamic gait shows higher energy in all configurations compared with the quasi-static gait. This result is due to the additional energy input into the system through the higher motor velocity: greater aerodynamic and inertial forces from the wings and higher leg velocities. The increase in energy from the WO case to the hybrid case is much more significant for the quasi-static gait (525%) compared to the dynamic gait (88%). At a higher flapping frequency and translational speed, the wing forces have a greater effect and provide damping of the discrete leg contact dynamics. This further reinforces the conclusion that the robot is best tuned to run at higher frequencies where the aerodynamic effects of the wings are significant.

5.1.4 Terrestrial to Aerial Transitions

By running along the ground at a high speed, BOLT can generate enough aerodynamic lift to take off. Depending upon the center of mass location, BOLT requires between one and two meters of runway space. Figure 5.5 shows the robot during a takeoff maneuver with the controller board mounted forward, causing a takeoff distance just under 2 meters when flapping at 18 Hz. The average acceleration for each stride is shown, along with the instantaneous velocity obtained by integrating the accelerometer data. BOLT accelerates very quickly from a standstill, reaching 1 ms^{-1} in 0.14 s and 2 ms^{-1} in 0.38 s. Upon reaching a velocity of 2.5 ms^{-1}, BOLT has taken off and is no longer touching the ground. The robot continues to accelerate until reaching 3 ms^{-1}. At this point the tail begins to swing under the robot and it enters a vertical flight posture. The vertical accelerations oscillate around zero throughout the maneuver as the robot bounces along the runway. The total vertical velocity stays very near zero however, as the accelerometer does not

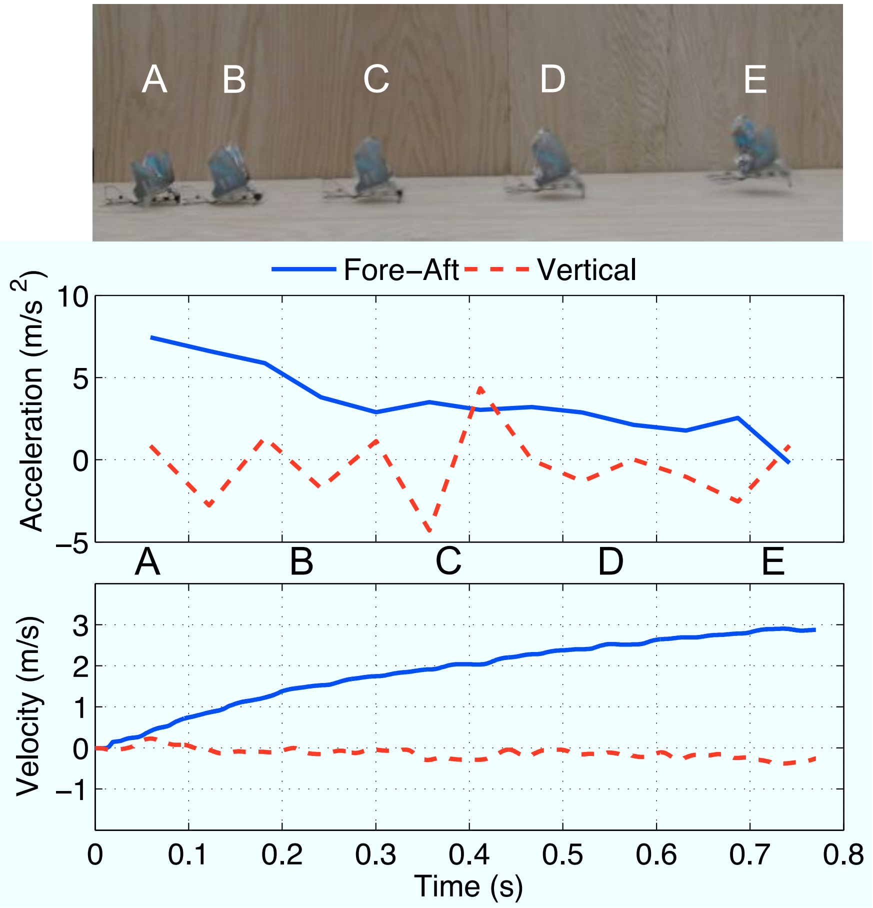

Figure 5.5: BOLT transitioning from terrestrial locomotion to aerial locomotion. The average acceleration of each stride/wingbeat is plotted, along with the velocity obtained by integrating the accelerometer data. The robot quickly builds speed (A-C), lifting off at 2.5 ms^{-1} (D) and continuing to accelerate until it reaches 3 ms^{-1} (E). The vertical acceleration oscillates around zero, giving near zero vertical velocity throughout the run.

pick up the slow movement upwards of the robot.

By moving the location of the controller board (and the center of mass), BOLT can be configured to have different transition properties. Moving the controller board forward increases the distance required for takeoff (∼2 m), but also increases the maximum terrestrial speed (2.5 ms^{-1}). Additionally, it allows the board to be placed on foam offsets, improving the IMU measurements. When the board is moved to the back of the airframe, the takeoff distance is reduced to 1 meter. The speed where takeoff occurs is also reduced to 1.75 ms^{-1}.

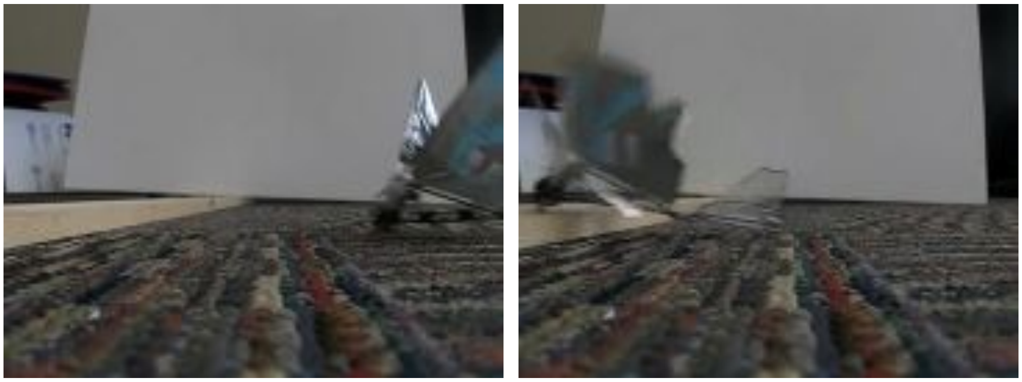

(a) BOLT (b) BOLT

(c) Wings-only (d) Wings-only

Figure 5.6: (a-b) show BOLT running at a 2 cm obstacle and easily clearing the top of it. By contrast, (c-d) show the wings-only robot incapable of getting over the barrier. The wings-passive robot is capable of clearing the barrier, but is not always successful.

5.2 Advantages of a Hybrid Aerial and Terrestrial Robot

The method BOLT uses to maintain stability when running differs between the quasi-static and dynamic gait. At low speeds, the tail of the robot remains in contact with the ground and provides an extra point of stability. At higher speeds, the airflow from the flapping wings passes underneath the tail, and it lifts off of the ground enabling truly bipedal locomotion. The aerodynamic forces from the flapping wings and the tail allow the robot to maintain passive stability despite its bipedal locomotion in the absence of any closed loop control. The sprawled posture of the legs and low-to-the-ground design help the robot maintain stability during both modes of locomotion.

By using the flapping wings to provide additional thrust, the terrestrial speed of the robot is significantly increased from a legged robot. With a quasi-static gait, the wings-passive robot has the best COT, while the wings-only robot performed best at a dynamic gait. The hybrid robot

(a) 30° incline, 0 s (b) 30° incline, 0.27 s (c) 30° incline, 0.54 s

(d) 30° incline, 0 s (e) 30° incline, 0.27 s (f) 30° incline, 0.54 s

Figure 5.7: BOLT running up 30° and 45° inclines with no special foot attachment mechanisms.

provides a compromise between the two, allowing more efficient locomotion when a range of speeds is necessary. At slow speeds legs provide more efficient thrust than wing flapping; at high speeds the wings allow the robot to “fly” along the ground, dramatically reducing the cost of transport.

BOLT also has the ability to self-right when inverted on the ground by flapping its wings. When upside down on the ground, the robot rests on its vertical tail stabilizer and its wing tips. The self-righting maneuver begins with the wing tips pushing the nose of the robot upwards and beginning the righting motion. From this position, the majority of the wing thrust is directed directly downwards, and the robot accelerates vertically. The passive aerial stability of the robot swings the tail underneath the robot and the robot can either continue flying or reduce the throttle and land, now properly oriented.

5.2.1 Obstacle Clearance

BOLT has also shown the ability to clear terrestrial obstacles, both with a running start and from standstill. Figure 5.6 shows BOLT clearing a 2 cm obstacle, the highest obstacle it can clear with a purely terrestrial gait. In the wings-only configuration the robot is unable to clear the 2 cm obstacle, clearly showing the necessity of the legs. The wings-passive robot can clear the obstacle, but does so inconsistently. BOLT has shown two methods of clearing this obstacle, depending on the initial condition when first encountering the obstacle. If the obstacle is encountered at the low point in the stride, the robot will run at the obstacle for a few strides until its legs are able to pull it over the top. During the high point of its stride, the robot simply leaps over the obstacle without stopping.

5.2.2 Wing-Assisted Climbing

Due to the high thrust provided by the wings, BOLT is capable of ascending both inclines and vertical walls. Wing-assisted incline running is a behavior utilized by many birds, and has been determined to require lower energy expenditure compared with aerial ascent at the same angle [29]. It is also a "safer" maneuver, as the robot is less likely to be affected by unsteady airflows. Finally, the robot is capable of ascending at a faster velocity when flap running compared to ascending aerially for comparable angles of ascent. Figure 5.7 shows BOLT ascending 30° and 45° inclines, using its standard carbon fiber legs.

To climb steeper inclines, specialized features are required. Carbon fiber spars are added to the tail to bias the angle of the robot, rotating the wing force angle to be forward and slightly towards the surface instead of away. While implemented with fixed spars currently, a similar effect could be obtained by added an elevator to the tail. In addition, Figure 5.8 shows two different foot designs, a micro-spine foot and a magnetic foot. Each of these feet has several critical design features to enable it to engage and release from the surface. The micro-spine foot (Fig. 5.8a) is attached to the leg through a compliant PET loop. This compliance allows the spines to rotate on the surface as the foot moves through its trajectory, reducing the impulse forces on the contact. The compliance also performs a critical force limiting function. At a critical load, the PET ankle will rotate such that the spines will disengage from the surface. This prevents high forces from being transmitted to the hip flexures, which can fail at high loads. With the micro-spine feet, BOLT is capable of climbing smooth (grade A) plywood at a 70° incline, with a speed of 0.2 ms^{-1}. Screenshots of the

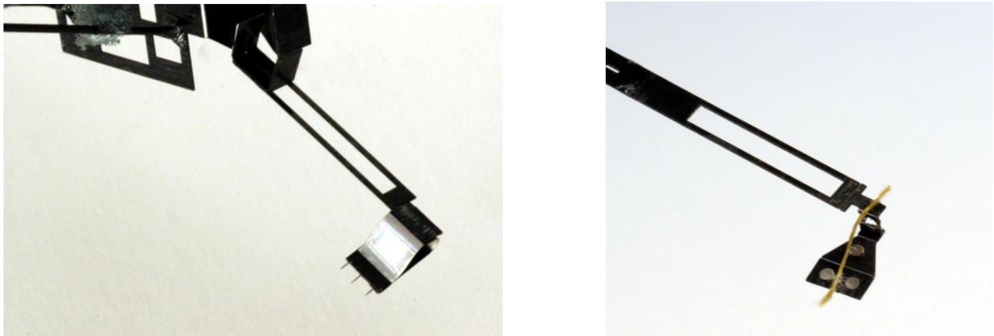
(a) Micro-spines (b) Magnetic

Figure 5.8: Different foot attachment mechanisms for wing-assisted climbing.


(a) 0 s (b) 0.3 s (c) 0.6 s (d) 0.9 s

Figure 5.9: Screenshots from high speed video showing BOLT climbing 70° plywood with the clawed feet shown in Fig. 5.8a at approximately 0.20 ms^{-1}.


(a) 0 s (b) 0.3 s (c) 0.6 s (d) 0.9 s

Figure 5.10: BOLT climbing 90° metal surface with the magnetic feet shown in Fig. 5.8b at approximately 0.6 ms^{-1}.

performance are shown in Figure 5.9

In addition to the micro-spine foot, we implemented a magnetic foot (Fig. 5.8b). This foot consisted of three segments, separated by PET flexures. The first segment attached to the leg through a very compliant ankle that was rigid in tension, but allowed the foot to rotate significantly otherwise. This allowed the foot to stick to the surface throughout the stroke. The second segment consists of a single magnet, with two magnets in the third segment. This foot design assists with disengagement. Instead of attempting to lift the magnets directly, a peeling moment is applied to the magnetic segment, allowing easier disengagement. By placing a single magnet next to the ankle and two magnets at the toe, a high attachment force is achieved with a smooth disengagement. A Kevlar string served to keep the toe and ankle aligned properly, preventing the compliant ankle from twisting too far. Figure 5.10 shows screenshots from a video of the robot climbing a vertical metal surface. The robot is capable of ascending the vertical surface at a speed of 0.6 ms^{-1}.

Chapter 6

Experimental Characterization of Passive Aerodynamic Stabilization of High Speed Running[1]

Animals tend to adjust their limb kinematics to increase speed while keeping their stride frequency relatively constant [19]. This adaptation allows the animal to operate in a single resonant regime, which is desirable for effective and robust locomotion across a range of speeds. For a minimally actuated system, adjustment of limb kinematics is often not possible due to the increased actuation complexity such an adjustment requires. Therefore, the stride frequency provides a useful way to change the locomotion speed of the robot, at the inertial expense of not running at a single tuned frequency.

The VelociRoACH (Figure 6.1) is a 10 cm long, 30 gram hexapedal robot capable of running at 2.7 ms^{-1}. The electronics of the robot controls an alternating tripod gait, and provide a six-axis inertial measurement unit for measuring the dynamics of the system. The electronics and mechanical design of the robot is discussed in detail by Haldane et. al. [22]. As previously discussed, running legged locomotion is characterized by periodic trajectories (limit cycles) of the system dynamics. As the scale of a robot is reduced, the rotational dynamics of the system have a larger effect on the motion of the robot: the moment of inertia, $I = mr^2$, scales with L^5. For a given, size-specific perturbation we expect a millirobot to rotate far more than a larger robot. For example: Edubot undergoes roll oscillations of 1° during steady state locomotion [11], whereas the 30 gram VelociRoACH can experience 25° roll rotations during stable locomotion. While some amount of rotational oscillation can stabilize the system [11], limit cycles with high rotational energy–coupled with low inertia–can increase the chance of a disturbance causing catastrophic failure. We therefore focused our dynamic tuning efforts on finding highly robust, passively stable limit cycles with minimal rotational energy.

---

[1] Based on joint work performed with D. Haldane and F. Garcia Bermudez [22]. This chapter represents K. Peterson's contribution to that work.

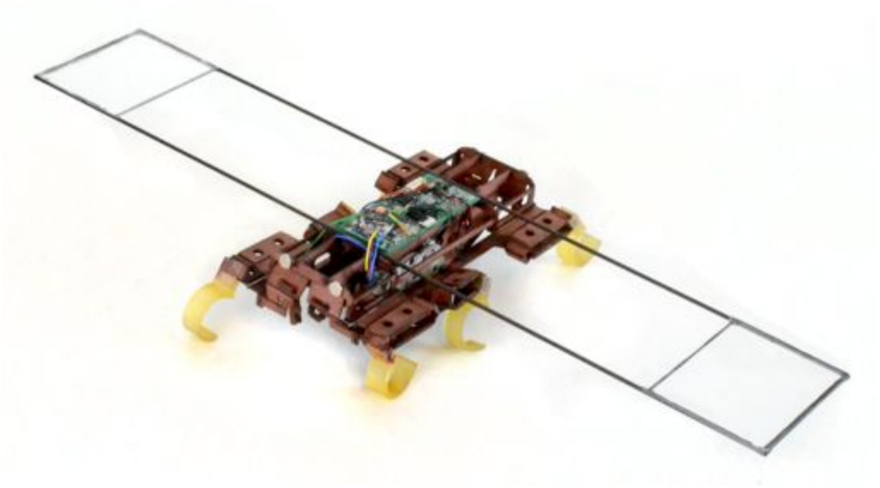

Figure 6.1: The VelociRoACH: a highly dynamic bio-inspired millirobot, shown equipped with an aerodynamic stabilizer. Figure courtesy D. Haldane [22].

6.1 Analysis of Low Rotational Energy Gaits

The gyroscope data can be used to determine the amount of total rotational energy the robot possesses in each stable limit cycle. To find the energy, we first parameterize the data by the accumulated stride phase, ϕ, which is the total angular rotation of the output link from the beginning of the trial. The rotational energy is calculated using the angular velocities measured from the on board gyroscope with

$$E_{Rot}(\phi) = \frac{1}{2}\omega(\phi)^T I \omega(\phi). \tag{6.1}$$

The energy is then divided into individual strides

$$E^n_{Rot}(\phi) = E_{Rot}(\phi) : 2\pi(n-1) \leq \phi < 2\pi n, \tag{6.2}$$

where n represents the stride number. The mean and variance among $k = 10$ successive strides is then computed from

$$\bar{E}_{Rot}(\phi) = \frac{1}{k}\sum_{n=1}^{k} \bar{E}^n_{Rot}(\phi) \tag{6.3}$$

and

$$\sigma(E_{Rot}(\phi))^2 = \frac{1}{k-1}\sum_{n=1}^{k}(E^n_{Rot}(\phi) - \bar{E}_{Rot}(\phi))^2. \tag{6.4}$$

As a metric of performance, we define the mean rotational energy during a stride to be

$$\bar{E}_{Rot} = \frac{1}{2\pi}\int_0^{2\pi} \bar{E}_{Rot}(\phi)\,\mathrm{d}\phi. \tag{6.5}$$

An additional metric, the mean normalized variance in energy over a stride is given by

$$\overline{\hat{\sigma}(E_{Rot})^2} = \frac{1}{2\pi}\int_0^{2\pi}[\sigma(E_{Rot}(\phi))^2/\bar{E}_{Rot}(\phi)]\,\mathrm{d}\phi. \tag{6.6}$$

6.2 Effect of Passive Roll Stabilizers on a High-Speed Running Robot.

During steady state running, the VelociRoACH has significant roll oscillations, as shown in Figure 6.2. These oscillations arise as a dynamic effect due to alternating tripod kinematics wherein one side of the robot has twice the effective stiffness of the other [11]. To reduce the roll oscillations, we add an aerodynamic stabilizer consisting of two rectangular sections, measuring 5 cm x 4 cm, of 50 μm PET oriented parallel to the direction of forward travel. These airfoils are rigidly constrained by a carbon fiber frame at a distance of 15 cm from the center of the robot (see Figure 6.1). As a control between the inertial and aerodynamic effects, we also examine the performance of the stabilizer with the PET airfoils removed. The aerodynamic stabilizer is specifically designed to damp roll oscillations, while being lightweight and having minimal drag in the forward direction. A significant aerodynamic force results when the robot rolls during high-speed running due to the high drag nature of a flat plate. We computed the differing inertias of the robot with and without the roll stabilizer using a CAD model of the robot and verified them in part using rigid body pendulum experiments. The form of the inertia tensors is given in (Equation 6.7), where x, y and z are the roll, pitch, and yaw axes, respectively. The standard robot has inertia, $\mathbf{I_0}$ (Equation 6.8); $\mathbf{I_S}$ (Equation 6.9) corresponds to the robot with the stabilizer.

$$\mathbf{I} = \begin{bmatrix} I_{xx} & I_{xy} & I_{xz} \\ I_{yx} & I_{yy} & I_{yz} \\ I_{zx} & I_{zy} & I_{zz} \end{bmatrix} \text{kg mm}^2 \tag{6.7}$$

$$\mathbf{I_0} = \begin{bmatrix} 9.29 & -0.12 & -0.22 \\ -0.12 & 21.51 & 0.007 \\ -0.22 & 0.007 & 21.97 \end{bmatrix} \text{kg mm}^2 \tag{6.8}$$

$$\mathbf{I_S} = \begin{bmatrix} 28.52 & -0.12 & -0.23 \\ -0.12 & 23.12 & 0.005 \\ -0.23 & 0.005 & 45.92 \end{bmatrix} \text{kg mm}^2 \tag{6.9}$$

6.2.1 Steady State Running

Telemetry data was captured for the VelociRoACH running on closed-loop pile carpet at stride frequencies in the $4-25$ Hz range. In particular, tri-axial gyroscope data was logged at 300 Hz during each run (repeated three times). We discarded the leading one second of each trial to remove any transient effects. To better understand the nature of the VelociRoACH oscillations as a function

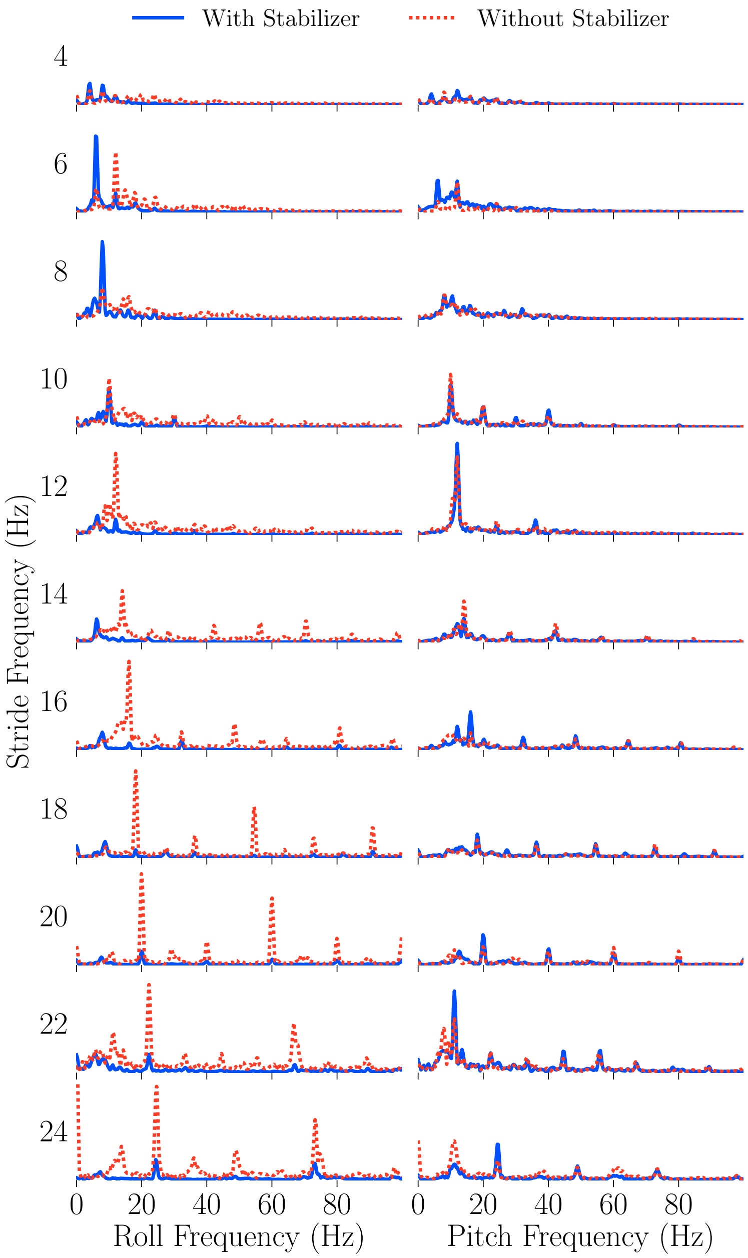

Figure 6.2: Frequency spectra of the robot's oscillations with and without the aerodynamic stabilizer plotted as a function of the commanded stride frequency. Components between 100–150 Hz have amplitude less than 30% of the fundamental frequency component and were truncated. Oscillatory energy in the roll axis was the highest of all the rotational components prior to the addition of the stabilizer. The stabilizer effectively filters this energy at higher stride frequencies. Yaw oscillations (not shown) are relatively unaffected by the stabilizer and have a peak magnitude of 904 °/s (harmonic components are less than 50% of the fundamental frequency maximum). Figure courtesy F. Garcia-Bermudez [22].

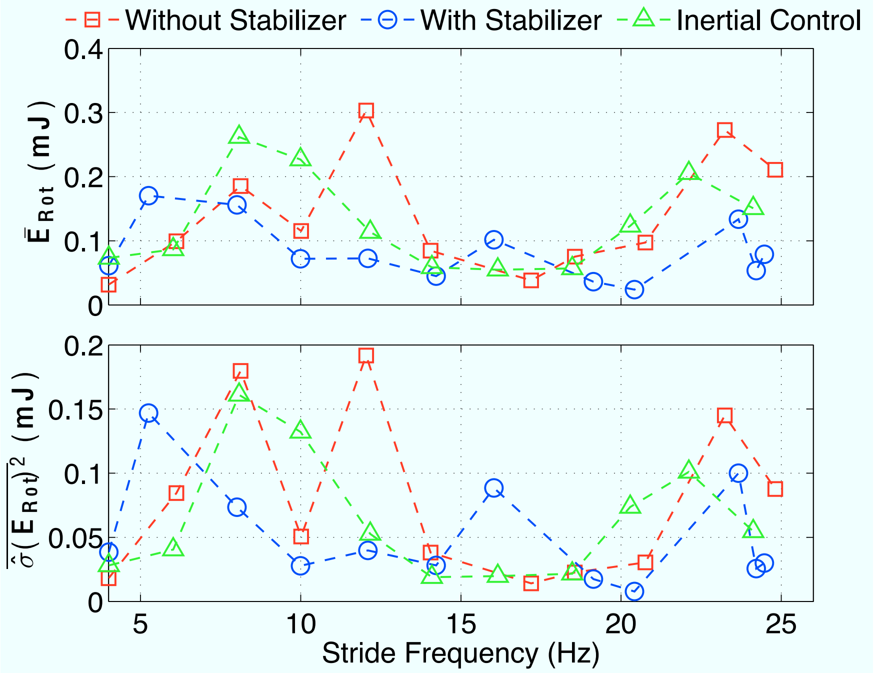

Figure 6.3: Lowest energy limit cycle for each treatment [Top] and average variation in the rotational energy over the course of a stride [Bottom].

of the stride frequency, we used Python[2] to compute the fast Fourier transform of each run, first passed through a Hann window, and then averaged across repeated trials. The resulting frequency spectra are plotted for pitch and roll in Figure 6.2. Roll shows a large degree of oscillation without the stabilizer, visible throughout the spectra and reaching up to the fifth harmonic of the commanded stride frequency. This motivated the addition of the stabilizer on the roll axis, and Figure 6.2 shows this approach was successful at reducing the degree of roll oscillations. Both pitch and yaw, which have less oscillations to begin with, are relatively unaffected by the added stabilizer.

Figure 6.3 shows the effect of both the aerodynamic stabilizer and the inertial control configuration on the system. At low frequencies, the higher inertias of the aerodynamic stabilizer and the inertial control increase the total energy. A local minimum in average frequency is found for the unmodified and inertial control case at 16 Hz, near the dynamically scaled frequency of the robot. By contrast, with the aerodynamic stabilizer equipped, the range of frequencies with low energy limit cycles is increased, reducing the robot's reliance on a single well-tuned frequency. We observe a clear decrease in the average energy over all frequencies ≥ 10 Hz for the aerodynamically stabilized robot when compared to the unmodified and inertial control cases. We also consider the robot's ability to passively maintain stable limit cycles while running in the presence of small perturbations, such as foot slip and ground contact variations. The variation in energy between

---

[2] Scientific Tools for Python: http://www.scipy.org/

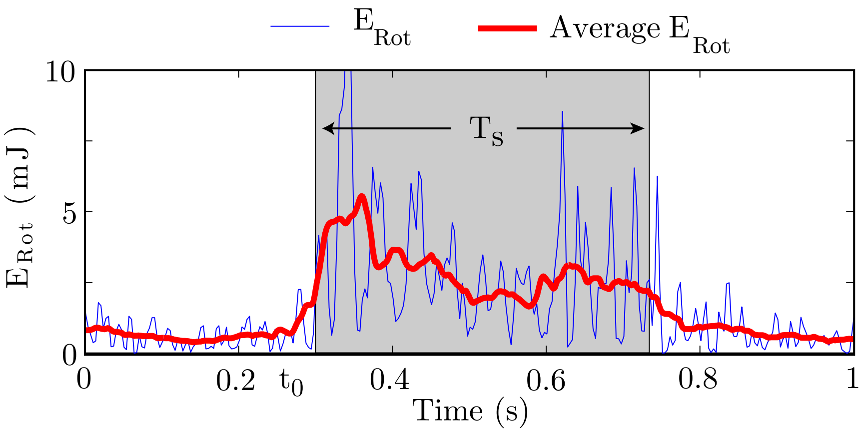

(a) Without Stabilizer

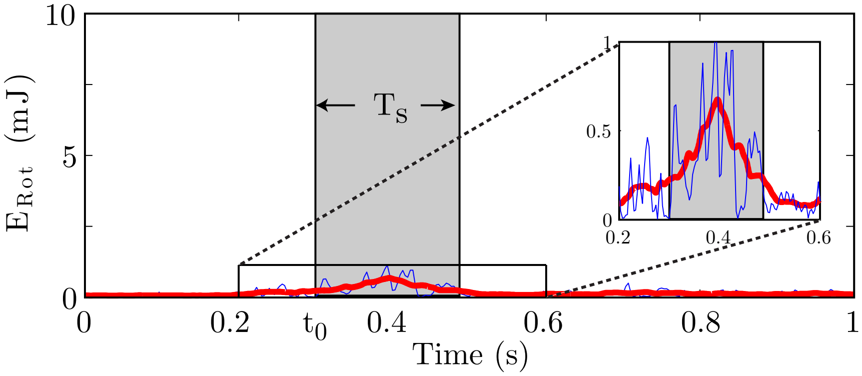

(b) With Stabilizer

Figure 6.4: Representative energetic disturbance and stabilization response to a step perturbation while running at 16 Hz. The average energy is computed using a moving average filter with a window size equivalent to the length of a single stride. T_s represents the duration of the transient response, which is shaded in gray.

successive strides shown in Figure 6.3 provides a measure of the periodicity of locomotion and of how robust the limit cycle is to small disturbances. Both the aerodynamic stabilizer and the inertial control show less variation in response to small perturbations. By contrast, the unmodified robot shows generally higher variation, and significantly higher variation at some frequencies. The lower inertia of the unmodified robot increases its susceptibility to small disturbances and correspondingly decreases the stability margin of the robot.

Table 6.1: Average disturbance response of VelociRoACH

Stride frequency		Configuration	
		Without Stabilizer	With Stabilizer
16 Hz	Ts	0.37 s	0.18 s
	$\bar{E}_{\text{Disturb}}$	1.15 mJ	0.37 mJ
	S_{Disturb}	435 $\mu J \cdot s$	66 $\mu J \cdot s$
20 Hz	Ts	0.29 s	0.24 s
	$\bar{E}_{\text{Disturb}}$	1.97 mJ	0.74 mJ
	S_{Disturb}	578 $\mu J \cdot s$	186 $\mu J \cdot s$

6.2.2 Disturbance Rejection

In addition to increasing robustness to small perturbations, we hypothesized that the aerodynamic damper would allow the robot to recover more quickly from large perturbations. To assess the validity of this hypothesis, we ran the robot over a known obstacle, in this case a vertical step equal to 35% of its hip height. We measured the departure of body-centric metrics away from the median state and their subsequent recovery. The robot is more prone to locomotion failures due to excessive body rotation, so we chose the body-centric parameter to be the rotational energy in the system. This was chosen over any individual component of rotation because the specific response of the robot is highly sensitive to when in the stride the disturbance was encountered, the robot's stride frequency, and whether or not the aerodynamic stabilizer was equipped. Therefore, the rotational energy of the system is a more robust indicator of the perturbed state of the robot. To account for the variations in the rotational energy due to the periodic motion of the robot, a moving average filter was applied with a window size equal to the length of a single stride. We selected the settling time of the robot, T_s, as a disturbance rejection metric. The settling time is defined as the time that it takes to dissipate 80% of the maximum energy increase due to the disturbance . We also calculated the average increase in rotational energy from the perturbation,

$$\bar{E}_{\text{Disturb}} = \frac{1}{T_s}\int_{t_0}^{t_0+T_s} (E(t) - \bar{E}_{\text{steadystate}})\,\mathrm{d}t, \tag{6.10}$$

and the action of the disturbance,

$$S_{\text{Disturb}} = T_s \cdot \bar{E}_{Disturb} \tag{6.11}$$

as additional figures of merit.

Representative step responses of the robot running at 16 Hz with and without the stabilizer are shown in Fig. 6.4a and Fig. 6.4b. The robot encounters the step at time t_0 and the transient response duration is shaded in gray. Table 6.1 summarizes the results of the disturbance rejection experiments (N≥3). The robot equipped with stabilizer shows increased performance across all metrics at both stride frequencies tested. Along with rejecting the disturbance more quickly, the aerodynamic stabilizer also reduced the amount of energy injected into the system by the disturbance. The action of the disturbance is reduced by a factor of six at 16 Hz and a factor of three at

20 Hz, demonstrating the success of the aerodynamically stabilized robot at initially rejecting and quickly recovering from the disturbance.

Chapter 7

Implications For the Evolution of Flight

7.1 Avian Flight Evolution: The Debate

There are four known independent cases of flight evolution: birds, bats, pterosaurs, and pterygote insects. The evolutionary path towards flight in all instances has been a subject of much academic debate for more than 100 years, and the theories on avian flight origins remain both paleontologically and biomechanically contentious. The debate has mainly centered around two opposing theories. The arboreal theory, originally proposed in [43] and extended by many others, posits that flight evolved through a gliding phase as animals climbed and leapt from tall objects. The cursorial theory, developed in [66, 48, 47], proposes that flight evolved from specialized forelimbs used for balance and extending leaps along the ground. Current support for the diverse theories of avian flight origins derive from limited fossil evidence, the adult behavior of extant flying birds, and developmental stages of already volant taxa.

Much of the debate around avian flight evolution centers on the capabilities and lifestyle of *Archaeopteryx*, an early bird that lived around 150 million years ago. *Archaeopteryx* is generally accepted as the earliest known bird and its origins are particularly relevant to answering the question of avian flight evolution [52]. Many different and conflicting arguments exist on the abilities of *Archaeopteryx*. In [18, 71, 72], the authors claim *Archaeopteryx* is adapted for an arboreal lifestyle on the basis of an analysis of morphological features such as claw and backbone shape. However, in [51, 54], the authors use the same features to claim a cursorial adaptation for *Archaeopteryx*.

The use of wings to augment cursorial locomotion has been shown in extant juvenile and adult birds [15, 28], and has been proposed as a alternative mechanism underlying the origin of avian flight. Increasingly abundant fossil evidence suggests that early birds passed through a four-winged stage prior to dedicated aerodynamic use of the forewings [69, 27, 2, 58], but the use of wings in cursorial behavior cannot necessarily be excluded given their aforementioned role in living birds. Nonetheless, the use of extant avian taxa to infer ancestral locomotor origins may not be entirely relevant given the high wing beat frequencies and amplitudes of modern forms [49]. Also, the most basal living birds are the already derived and mostly secondarily flightless palaeognaths [23], and modern avian taxa are thus unlikely to be representative of avian precursors in terms of morphology or biomechanical performance. Theoretical modeling suggests that an Archaeopteryx-type morphology could more than triple maximum running speed through wing flapping [12], but this conclusion neglected drag forces on the wings and body which would significantly reduce horizontal thrust. More generally, the mechanical consequences of adding wings to a pre-existing cursorial taxon may be multifaceted and require empirical analysis to avoid potential problems associated with modeling assumptions. Here, we use our robotic platform to evaluate the additive effects of wing flapping on both cursorial and aerial locomotor performance, and discuss its relation to early avian flight.

To examine the performance of the platform, we examine several different capabilities. Maximum running speed is a critical performance metric, as is the ability to rapidly move up inclines. In cursorial ascent, flapping wings can provide additional normal force to increase foot traction [10], or can provide additional thrust to propel the body up the incline. In free flight, flapping of wing precursors will tend to reduce the descent angle, enabling further travel and greater temporal opportunities to effect maneuvers [16]. This behavior has also been shown in extant juvenile birds with undeveloped wings [28]. Through the addition of wings to a cursorial robot, we determined the incremental mechanical advantages associated with wing flapping in contexts of both running and flying.

7.2 Examination of Avian Flight Evolution Using a Hybrid Robot

We examined the effects of simple flapping wings on locomotion using DASH+Wings (Fig. 7.1a, [55]), described in section 3.1. DASH+Wings is set apart from other hybrid robots by being a superior running robot without the wings, allowing direct examination of the effects of wing addition on a running platform.

7.2.1 Experimental methods

We tested running performance of the robot in four different mechanical configurations: legs alone, legs with flapping wings, legs with passive wings, and legs with flapping inertial spars (Figure 7.1). Passive wings are obtained by disconnecting the wing drive linkage, allowing the motor to drive the legs while the wings are extended laterally. The inertial spars consist of the plastic leading edge of the wings with the membrane removed, and flap in the same manner as the entire wings. The spars have a moment of inertia of 1.183×10^{-6} kg m^2, while the moment of inertia of the entire wing is 3.377×10^{-6} kg m^2. Spars with a moment of inertia similar to that of the wings were found to cause erratic running in the absence of the wing damping. Therefore, we use spars with lower moment of inertia to allow measurement of stable running performance. To measure maximum horizontal velocity, a high-speed camera (Casio EX-F1) was used to record the robot's motion across a smooth tile floor at 300 fps for multiple trials. Only trials where the robot reached a steady-state velocity while in the frame of the camera were considered; the remaining trials were

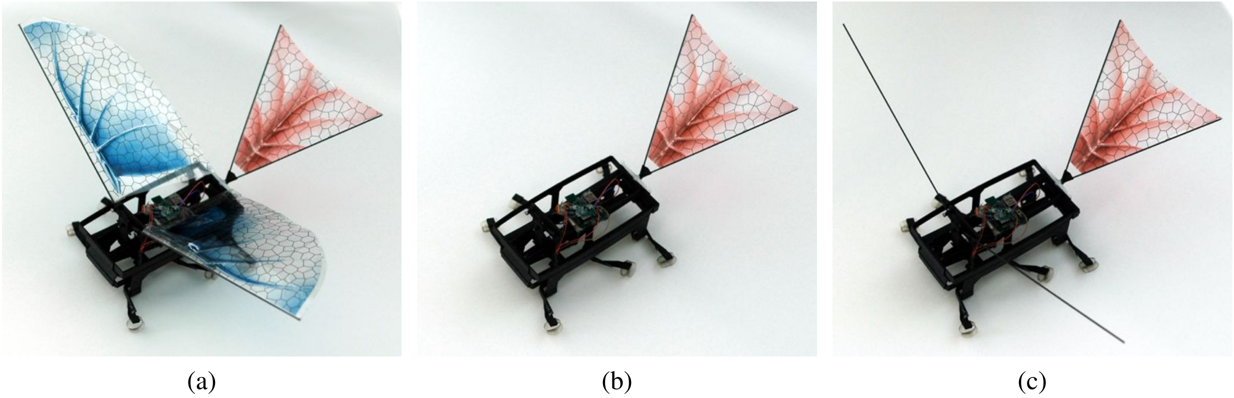
(a) (b) (c)

Figure 7.1: A dynamic hexapedal robot with flapping wings (DASH+Wings) for (a), flapping wings configuration; (b), legs-only configuration; and (c), inertial spars configuration. The fourth configuration (wings passive) is as in (a) but with the wing drive disconnected. Robot length (excluding the tail) is 10.0 cm; wingspan is 30.5 cm.

discarded. Average maximum running speed was determined by averaging the successful trials for each test configuration.

An incline oriented at varying angles to horizontal was used to determine the maximum incline that could be traversed for each experimental configuration of the robot; via incremental increases in angle, the final slope at which the robot was capable of forward progress could be determined (Figure 7.2). The incline is composed of smooth particleboard characterized by a static friction coefficient of 0.26 and a kinetic friction coefficient of 0.21 between the board and the feet of the robot. Acrylic guide rails on either side of the robot ensured rectilinear displacement directly up the slope; two trials were carried out at each slope and always yielded the same final angle.

Aerodynamic characteristics of the robot were measured in a wind tunnel (Aerovent, Inc.) with a square cross section for the working section of 0.61 m^2. The wingspan of the robot was 0.031 meters, giving a clearance of a half wingspan on either side. Particle Image Velocimetry was used to characterize the wind tunnel and determine the turbulence present. Measurements show 4.6, 1.2, 1.0, and 1.0 percent turbulence, for 1.5, 3, 6, and 9 ms^{-1} respectively. For the two conditions of flapping and passive wings, we varied the body angle of attack (0° to 45°) and wind speed (0 to 9 ms^{-1}), and measured the ensuing lift and drag using an ATI Nano 17 6-axis force transducer. The lift and drag coefficients were calculated using the total planform area of the robot (0.0256 m^2). The raw sampling frequency of the sensor is 10 kHz, with an averaging level of 16, giving the collected data a sampling rate of 625 Hz. Forces were averaged over 20 s to remove inertial influences of the drive mechanism, and each trial was repeated 5 times to remove the effects of sensor noise and air turbulence.

Gliding and flapping trajectories of the robot in free flight were measured using 2 Casio EX-F1 cameras in FHD mode (resolution of 1920x1080 pixels at 30 fps) positioned at an orthogonal

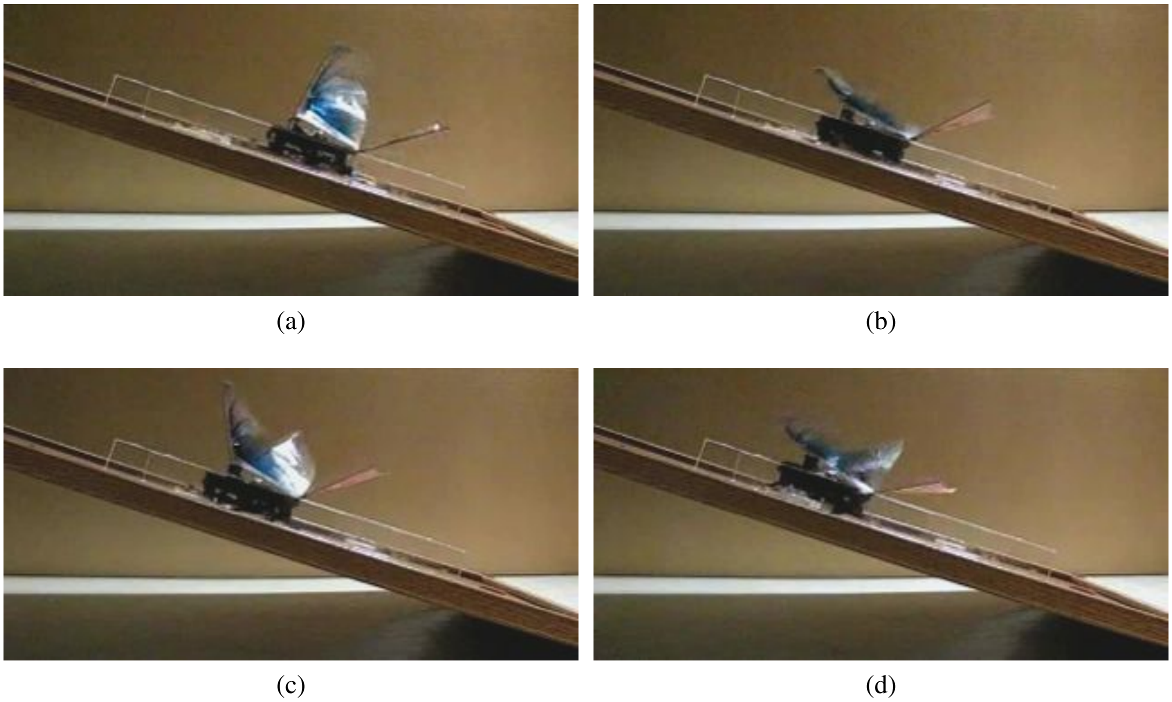
(a) (b) (c) (d)

Figure 7.2: DASH+Wings running up a 16.9° incline using flapping wings.

distance of 25 m and 23 m to the flight path, spaced 7 m apart. To start the robots flight, it runs off a 0.3 m long ledge under its own power. To determine the path of the robot in free flight, we use a basic pinhole camera model. The cameras are set up in a large area with a well-defined background. By measuring the location of points in the backdrop, the intrinsic and extrinsic parameters of each camera can be found. We use MATLAB to perform a least squares regression on the known locations in the frame to determine the parameters in the collinearity equations for camera calibration. By combining the robots location from each camera, the location of the robot in three dimensions can be found. After correcting for perspective, the equilibrium flight speeds and angles relative to horizontal were determined from linear regressions of positional data versus time.

7.2.2 Running Performance

Maximum horizontal running speed of the robot with flapping wings was 1.29 ± 0.07 ms^{-1} [mean ± 1 s.d.; 11 trials), as compared to 0.68 ± 0.07 ms^{-1} (15 trials) for the legs-only configuration (Figure 7.3; ANOVA for overall effect of four treatments: F=653, d.f. 3, 52, $P < 0.0001$). With fixed wings, the maximum attained horizontal velocity was 0.72 ± 0.019 ms^{-1} (16 trials; see Figure 7.3), which was statistically equivalent (Fishers PLSD, mean difference of 0.29 ms^{-1}, $P > 0.05$) to the legs-only condition despite the marginal weight and drag increase associated with

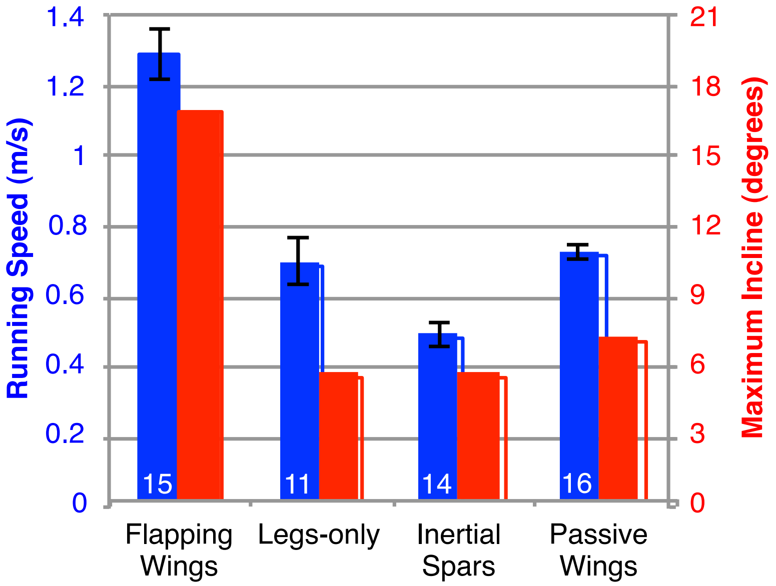

Figure 7.3: Maximum steady-state running speed (left) and maximum traversed incline (right) for DASH+Wings under different mechanical configurations at a stride frequency of 14 Hz. For maximum speed data, error bars indicate one s.d., and the numerical insets indicate the number of trials at each configuration. Standard deviations for maximum incline were zero for each configuration (see text).

the wings. With added inertial spars rather than wings, maximum horizontal speed of the robot dropped substantially to 0.48 ± 0.04 ms^{-1} (14 trials; Figure 7.3), the lowest value for all test cases. All cases except the passive wings and legs-only case were statistically different (Fishers PLSD, $P < 0.0001$).

To examine the intra-stride forces present on the robot, we averaged accelerometer data from the robot for several successive strides when the robot was running at a constant velocity with a smooth gait in each configuration (Figure 7.4). Large accelerations caused by the differential transmission design, evidenced by the high accelerations seen while the robot is in free fall, prevent straightforward analysis of the forces on the center of mass. The effects of the different forces from each configuration are better understood studying the position profile. A clear consequence of the different configurations on the intra-stride motions of the robot can be seen by looking at the horizontal and vertical position of the robot, obtained by twice integrating the accelerometer data (Figure 7.5). From this data, we observe that the amplitude of the vertical oscillations of the robot over the different configurations is inversely proportional to the horizontal speed it is capable of attaining. By directing less energy into vertical oscillations, it is possible that more energy is available for increasing the horizontal speed of the robot.

In ascending an incline, the use of flapping wings increased the maximum attainable incline nearly three-fold, from a value of 5.6° with the legs alone to 16.9° with flapping wings (Figure 7.3).

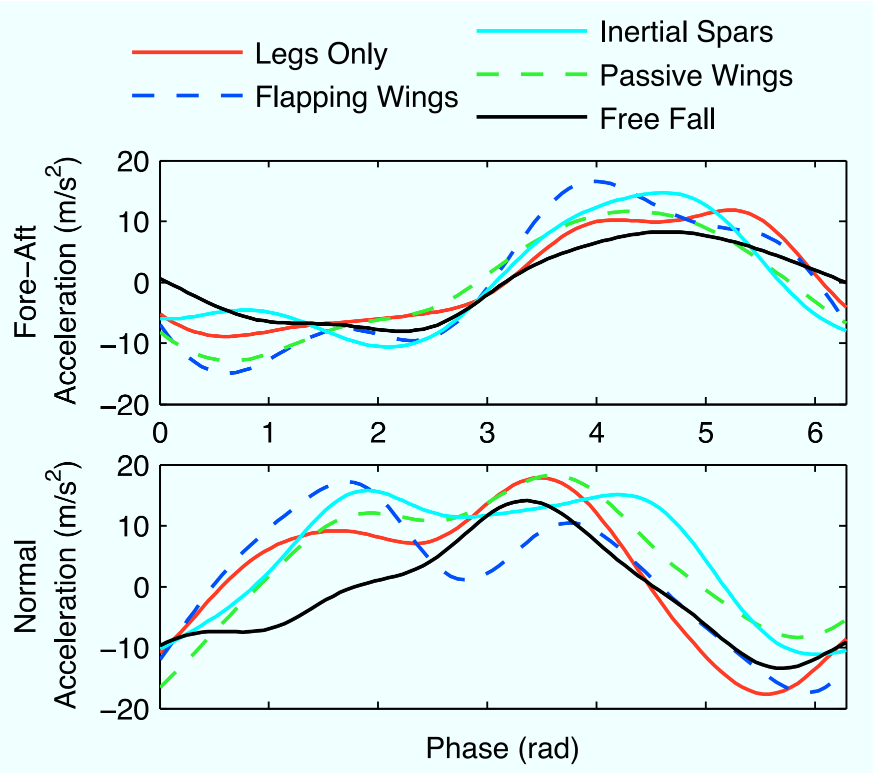

Figure 7.4: Accelerometer measurements of the robot over an average revolution of the motor output gear. The four tested configurations are shown, along with the acceleration while the robot is in free fall. The large sinusoidal signal seen in all five cases is due to the motion of the accelerometer with respect to the center of mass due to the differential drive mechanism.

For the configurations of either inertial spars or passive wings, the maximum slope attained was nearly the same as for the legs-only case: 5.6° and 7.1°, respectively. All cases except for the legs-only and inertial spars case were statistically different (Fishers PLSD following ANOVA, $P<0.0001$ in each case).

7.2.3 Aerial Performance

Lift and drag forces measured on the robot when fixed within a wind tunnel demonstrated strong variation with both airspeed and body (i.e., stroke plane) orientation. At an airspeed of 1.5 ms^{-1}, the flapping wings produce negative drag (or positive thrust) on the robot at lower angles of attack, resulting in the negative coefficients of drag seen in Figure 7.6. At airspeeds of 3 ms^{-1} and above, the drag force from the air-flow overcomes the force produced by the wings, and the coefficient of drag is positive for both flapping and gliding cases. In this scenario, the flapping wings always demonstrated a higher lift-to-drag ratio compared to passive wings (Figure 7.6, Table 7.1). While the flapping wings always show better performance, the margin of improvement decreases as the

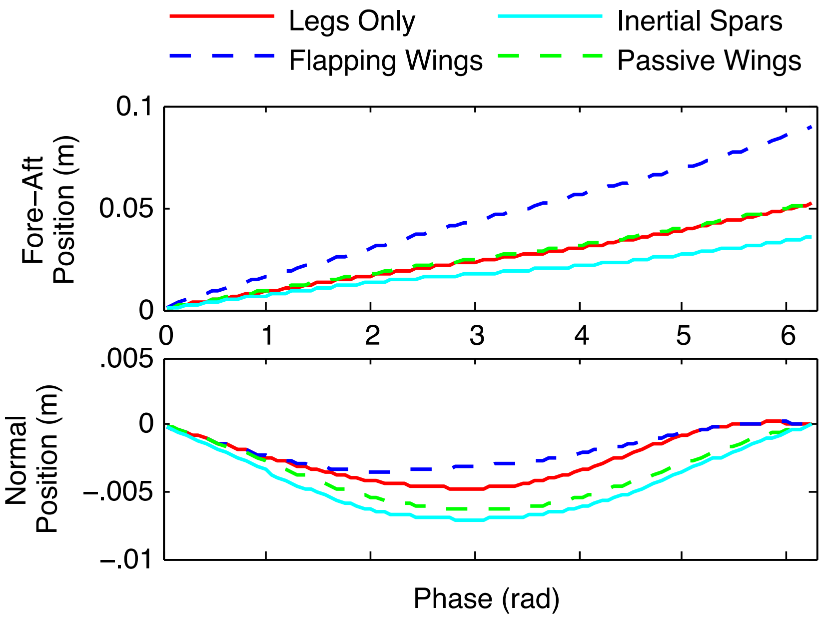

Figure 7.5: Change in the fore-aft and normal position of the robot over one complete stride. The amplitude of the normal variation in position over the four configurations is inversely related to the horizontal speed the robot is capable of reaching.

airspeed and body angle of attack increase. From the measured forces on the robot, the descent angle (γ) of the robot gliding in equilibrium can be predicted. When the robot is moving at constant velocity and orientation, the total forces on the robot must equal zero:

$$mg = F_D \sin\gamma + F_L \cos\gamma \tag{7.1}$$

$$0 = F_D \cos\gamma F_L \sin\gamma \tag{7.2}$$

From these equations the relationship between the magnitude of the lift and drag forces is given by:

$$(F_L^2 + F_D^2)^{\frac{1}{2}} = mg \tag{7.3}$$

For a given angle of attack of the body and use of either flapping or gliding wings, the air speed is increased computationally until the magnitude of the forces meet this equilibrium condition. The descent slope is then found from:

$$\gamma = \tan^1 \frac{F_L}{F_D} \tag{7.4}$$

Based on the wind tunnel measurements, we estimate the lowest attainable descent angle for the gliding wings to be 38.9°, at an airspeed of 6 ms^{-1} and a body angle of attack of 30°. With flapping wings, the estimated descent angle improves to 24.7°, at the slower airspeed of 4.9 ms^{-1} and a body angle of attack of 25°.

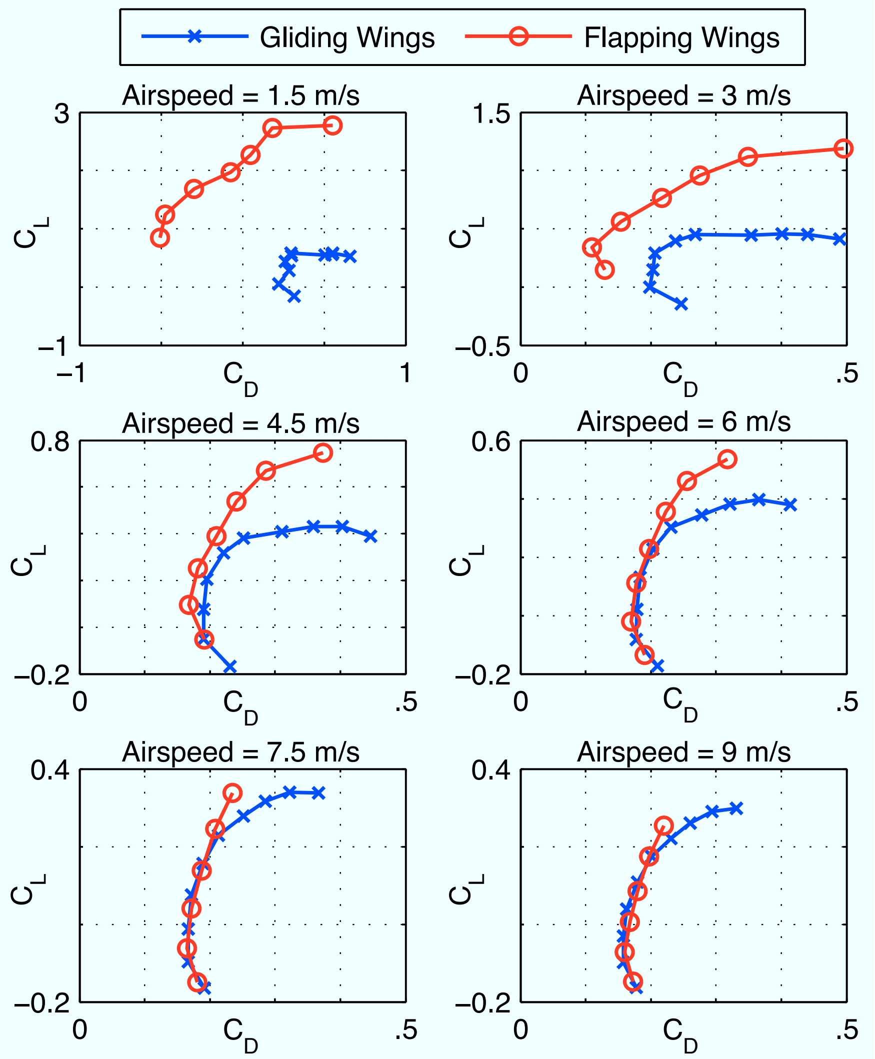

Figure 7.6: Coefficients of lift and drag at different airspeeds with the wings flapping (at 14 Hz) and passive over a range of body angles of attack (5° intervals starting at 0°). Flapping wings show a dramatic advantage at low airspeeds, with the effect diminishing at higher speeds. Advance ratios based on wingtip speed ranged from 2.7 at an airspeed of 1.5 ms^{-1} to 16.3 at 9 ms^{-1}; mean Reynolds number of the wings (based on mean chord length and airspeed) ranged from 6.1×10^3 at 1.5 ms^{-1} to 3.67×10^4 at 9 ms^{-1}. Five trials were performed at each data point, with st. devs. of the lift and drag coefficients on the order of 0.001.

Table 7.1: Selected lift:drag ratios of DASH+Wings measured in wind tunnel[a]

Body angle of attack (α)	Condition	Airspeed		
		3 ms^{-1}	6 ms^{-1}	9 ms^{-1}
10°	Flapping	3.65	0.62	0.03
	Gliding	0.73	0.11	-0.20
20°	Flapping	3.47	1.59	0.88
	Gliding	3.47	1.59	0.88
30°	Flapping	2.40	1.69	N/A[b]
	Gliding	1.26	1.23	0.96

[a] The complete set of wind tunnel measurements can be found in Figure 7.6

[b] The motor cannot produce enough force to flap the wings at this airflow and body angle of attack.

In free flight, the weight distribution of the robot (dependent upon the transmission design and motor position necessary to drive the legs and wings, see [6, 57] for details) precludes gliding at such body angles of attack that would yield the lowest glide angles. Instead, the robot is only capable of approximately a 10° body angle of attack. Nonetheless, direct measurement of descent angles for the robot in free flight demonstrated a value of 68.0 ± 1.8° for passive wings and a substantial decrease to 57.7 ± 2.24° using flapping wings (ANOVA, n = 6, $P < 0.0001$), (Figure 7.7); equilibrium airspeeds averaged 9.8 ms^{-1} and 10.7 ms^{-1} for these two cases, respectively.

7.2.4 Discussion of DASH+Wings performance

For running on level ground, wing flapping creates a significant increase in the horizontal translational velocity of the robot. The additional thrust from the wings allows for a near doubling of the translational speed of the legs-only configuration. The tradeoff for this improvement is the additional power required from the motor to drive the wings as well as the legs. The addition of flapping wings also has important implications for the stability of the robot during terrestrial and aerial locomotion.

The added thrust provided by the wings critically underpins the ability of DASH+Wings to traverse greater inclines relative to DASH alone. Whereas higher friction materials or claws can increase traction of a robot climbing an incline, their efficacy is typically very surface-dependent. In addition, the stiffness and frictional properties of the substrate, along with leg stiffness, greatly affect the center of mass dynamics of a basic legged robot. With greater adhesion to the surface, the robot requires more precise tuning and control to prevent legs from jamming and destabilizing the robot. Whereas running animals can dynamically c[64], this outcome is not possible using a single actuator robot. The added thrust from the wings, in addition to aerodynamic and iner-

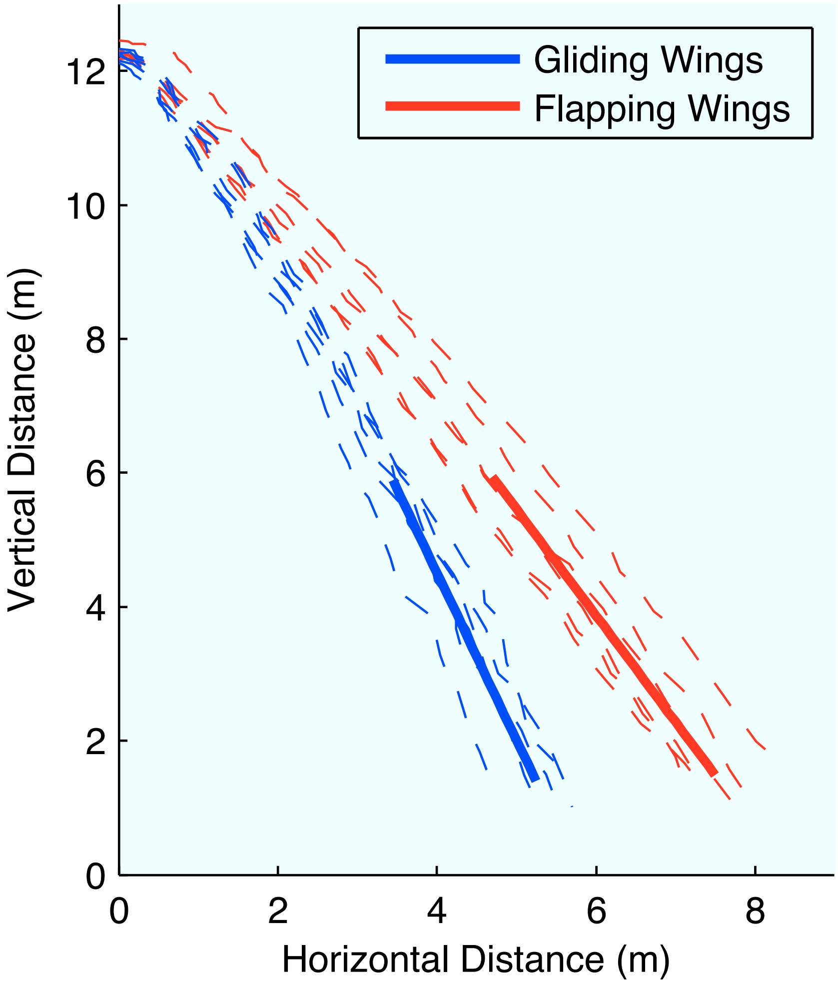

Figure 7.7: Flight trajectories for the passive and flapping wing robot. The dashed lines represent the individual trials, with the solid bold lines representing the average descent slope at the end of the flight, 68.0 ± 1.8° and 57.7 ± 2.24° for gliding and flapping flight respectively.

tial damping, enhances performance by the robot independent of various parameters that directly influence ground reaction forces.

Well-tuned cursorial systems typically exhibit smoothly varying sinusoidal forces on the center of mass from ground reaction forces [24]. In this context, incorrectly tuned legs can result in impulsive foot contact forces, leading to inefficient and potentially unstable gaits [31]. Unstable gaits in a legged platform can excite growing pitch or roll oscillations, which can lead to platform rollover or inversion. The robot in the legs-only configuration requires a narrow range of leg stiffness to achieve stable, high-speed running for a given stride frequency and mass [6]. To examine the effect of flapping wings on stability, we examined the performance of the robot with and without the flapping wings when running on improperly tuned legs. Over fifteen trials with the legs-only robot, the robot exhibited roll instability in ten trials, pitch instability in two trials, and both roll and pitch instability in three trials. Eleven of the fifteen trials ended with failure about the roll axis of the robot. In contrast, when running with flapping wings, the robot experienced no instability or failure over ten trials, running smoothly in each case despite the improper leg tuning.

We hypothesize the addition of flapping wings to DASH reduces the effect of impulses from improperly tuned legs on the dynamics of the robot, with the aerodynamic damping from the wings lessening the sensitivity of the robot to leg tuning. Whereas increasing leg forces can be destabilizing without proper tuning, wing addition is a simple means of increasing locomotor force without compromising stability due to the wings inherent damping. Flapping wings have previously been shown to increase stability about the axis perpendicular to the stroke plane during flight [17]. DASH+Wings shows a similar effect when running along the ground, exhibiting greatly improved roll stability with flapping wings.

Adding wings and a tail to DASH also allowed the robot to attain stable aerial descent, albeit at a fairly high descent angle. It should be emphasized, however, that prior work has demonstrated the robustness of SCM structures when falling from large heights [6]. Stable descent facilitates landing on the legs and the resumption of cursorial locomotion. When combined with stable running and the ability to move up inclines, the performance space of DASH+Wings is dramatically enhanced relative to the original DASH design. By contrast, wind tunnel measurements of aerodynamic performance reveal deficiencies in the current aerial design of the robot. The body angle of attack of the robot in free flight is determined by the relative positions of the center of mass and center of pressure. The transmission design and motor position necessary to drive both legs and wings cause the center of mass to be in a position that gives a low angle of attack when compared to the optimal angles of attack found from the wind tunnel results. This lower angle of attack leads to the higher descent angles and faster velocities seen in the free flight results. Additionally, at low body angles of attack the wing camber was substantially reduced at higher airspeeds because of the intrinsic flexibility of the wing membrane. Lift and the lift:drag ratio were correspondingly reduced for both flapping and passive wings. The motor also reaches power limits at higher airspeeds and angles of attack and is unable to flap the wings.

7.2.5 Functional Insight on Avian Flight Origins

From a paleobiological perspective, these results broaden our understanding of the consequences of wing flapping for avian precursors. An important question concerns the extent to which wing flapping will increase either running or aerial performance. The addition of wings flapping at 14 Hz to the DASH robot increases maximum horizontal running speed by only a factor of 1.88. By contrast, Burgers and Chiappe [12] estimated from a theoretical model that wing flapping by a running Archaeopteryx would require an almost four-fold increase in translational speed to obtain forces sufficient to attain free flight. As mentioned in section 7.1, optimistic aerodynamic assumptions in the model of Burgers and Chiappe [12] may have contributed to excessively high estimates for thrust production. The robot used here is of course hexapedal rather than bipedal, and other features of the platform (e.g., mass, wing structure) do not match those of Archaeopteryx or other early birds. We nonetheless view these results as heuristically important and indicative of the need for continuing interdisciplinary work. DASH+Wings is also capable of wing assisted incline running (WAIR) as documented in multiple extant birds by Dial et. al. [14], although it uses a significantly different mechanism to do so. The chukars observed by Bundle and Dial [10] show a significant increase in performance during WAIR by varying their wing kinematics so as to redirect aerodynamic forces toward the substrate and enhance traction. DASH+Wings simply takes advantage of the added thrust provided by the wings to increase speed and climbing ability. Whereas this method provides a lower degree of performance, it does not require a rotation of the wing stroke with respect to the body, and may have been more easily accomplished by early avian precursors with simple wing kinematics. Wing flapping by DASH+Wings in free flight reduces the equilibrium glide angle by 10.3°, although this enhancement is here limited primarily for reasons of stability of the robotic platform, and would likely be greater for more avian-like body forms. As expected, wing flapping does improve the lift:drag performance relative to static wings at all fixed body orientations of DASH+Wings (see Table 7.1). A progressive evolutionary increase in wing beat frequency in an early bird would thus increase lift relative to drag for a fixed wing geometry, thereby enhancing aerodynamic performance while gliding (see [16, 50]). Low-amplitude wing motions could also serve in maneuvers, perhaps a more important feature than steady-state gliding ability. At present, it is not possible given the kinematics and body planform used here to elucidate further such aerodynamic benefits.

Similarly, the observed increase in horizontal translational speed with wing flapping, together with an 11° increase in attainable incline, suggest associated locomotor advantage, although to a lesser degree than that predicted by previous cursorial models, at least for the kinematics (flapping frequency of 14 Hz; stroke amplitude of 30°) implemented here. Although there are substantial differences in the robot dimensions and mechanical configuration used here relative to those of postulated avian precursors, these values of flapping frequency and amplitude are likely higher than those that characterized incipient fliers, whether terrestrial or arboreal in origin. Recent paleontological findings indicate flight feathers on all four limbs of dinosaur lineages close to the origins of birds [27]. Recent findings have also discovered the existence of small theropod dinosaurs [68], possibly more suited to arboreal and aerial behaviors. If indeed avian flight was characterized by gliding and thus aerial origins, any demonstration of beneficial effects of wing flapping is informa-

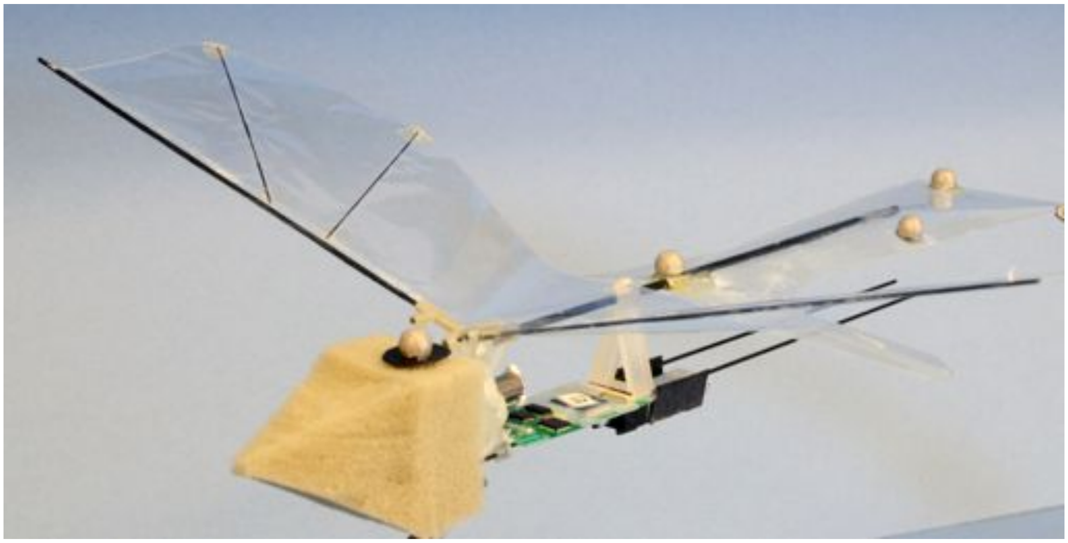

Figure 7.8: Morphologically scaled *Archaeopteryx* model.

tive, although a key goal of future work in this area must be to assess a broader range of kinematics than we have implemented here. Nonetheless, these results suggest that benefits of wing flapping to cursorial performance have been over-estimated. By contrast, even simple wing flapping with a flexible membrane (and no pronation or supination) can improve gliding performance, at least for the relatively high value of wingbeat frequency used here, We accordingly hypothesize that even simplified wing strokes may have yielded aerodynamic advantage to gliding avian precursors.

7.3 Aerodynamic Capabilities of *Archaeopteryx*

The flight performance characteristics of *Archaeopteryx* are widely debated. While most scientists classify *Archaeopteryx* as an early bird, the extent of its aerial abilities is contested. Padian and Chiappe [53] argue that *Archaeopteryx* is not aerodynamically designed for gliding, and likely lived on the ground. However, Yalden [70] believes that it is likely possible that it could fly for short time periods, as well as being arboreal. These divergent conclusions based on the same set of fossil evidence highlight the shortcomings of paleontological analysis; with no way of truly knowing the musculature and behavior of the specimen, it is possible to reach very different conclusions.

To address this issue, a morphologically scaled model of *Archaeopteryx* was built. The model was based on the reconstruction performed by Yalden [70] and Longrich [39]. Table 7.2 shows some critical dimensions of *Archaeopteryx*, and their corresponding scaled dimensions on our model. Morphologically correct physical models of avian precursors have been used previously, both in wind tunnel [32] and free flight experiments [3]. However, these studies examine static models, and do not examine the effects of wing flapping on performance. Our model implements a flapping wing with simplified kinematics and passive aerodynamic rotation of the airfoil. By altering the parameters of the wing stroke (frequency, amplitude), we can investigate their effect

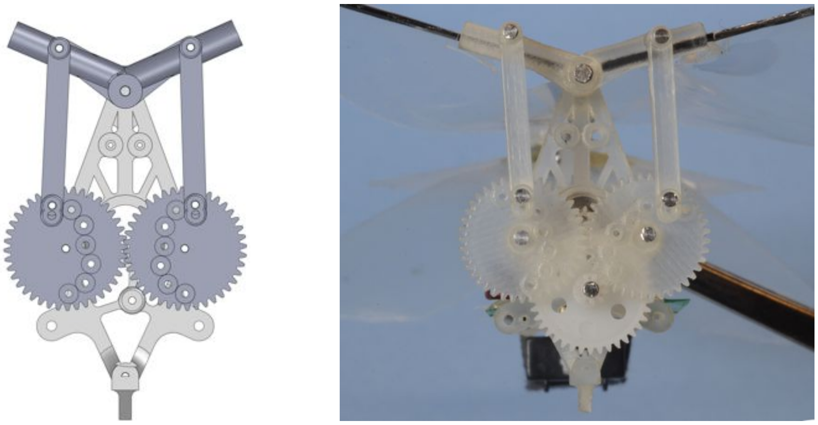

(a) (b)

Figure 7.9: Custom transmission for allowing variable flapping frequency of the *Archaeopteryx* model.

on performance, and draw additional insight into flight evolution.

7.3.1 Design and Experimental Methodology

Our model of the *Archaeopteryx* (Figure 7.8) draws heavily from the design of BOLT, presented in section 3.2. However, several modifications to the design are implemented. The model uses a single custom wing, in contrast with the two-wing flap-and-cling design of BOLT. The wing is reinforced with 0.28 mm carbon fiber spars to provide some rigidity, while still allowing the wing to passively rotate in response to aerodynamic forces. To allow the amplitude of the wing to be altered, a custom transmission and gears are used (Figure 7.9). The custom gears provide different attachment points for the wing drive rod. By changing the length of the crank, the amplitude of the wing can be can be varied from 30° to 70°. Figure 7.10 shows the frames from high speed video of the different wing amplitudes. In addition, the passive rotation of the airfoil is evident. In addition, the wing stroke is limited to 20° above horizontal, regardless of the flapping amplitude. This limitation seeks to accurately capture the hypothesized limitations in the shoulder structure of *Archaeopteryx*.

Table 7.2 shows the scaling parameters and dimensions for creating the aerodynamic surfaces of the model. Figure 7.11 shows a top view of the model, with a scale bar included for reference. Overall, our model has a wingspan of 26 cm, and a total length of 27 cm, including the foam nose cone. This corresponds to a linear scaling factor of $\alpha_L = 0.43$ when compared with an *Archaeopteryx* with wingspan of 60 cm. The remainder of the dimensions are scaled geometrically, with surface areas scaled by α_L^2 and the mass by α_L^3. The tail and hindwings (Figure 7.12) were created by vacuum forming 125 μm PET film on molds created with a 3D printer. This allows for the creation of lightweight airfoils with more complex shapes than a simple flat plate. The shape also add structural integrity, preventing the surface from significant deformation under load.

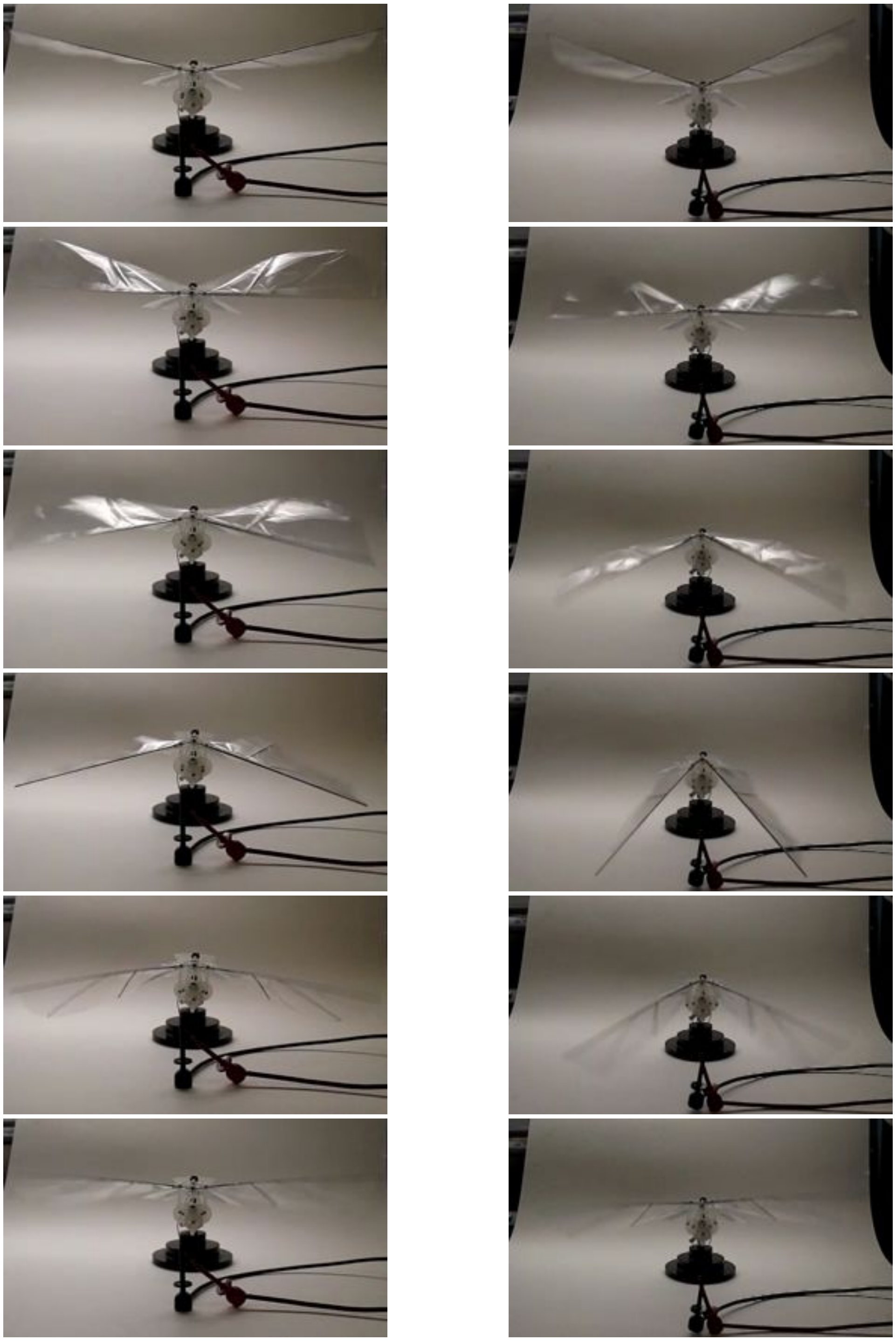

(a) 30° Flapping amplitude (b) 70° Flapping amplitude

Figure 7.10: Flapping motion of the *Archaeopteryx* model. The downstroke begins in the top frame and the upstroke begins in the 4th frame. The flexible wing passively rotates to provide thrust during both the downstroke and upstroke.

Table 7.2: Scaling the model *Archaeopteryx*

Parameter	*Archaeopteryx*	Scale Factor	Model
Wing Span	60 cm	$\alpha_L = 0.43$	26 cm
Aspect Ratio	5.0	1	5.0
Wing & Body Strip Area	720 cm^2	α_L^2	138 cm^2
Hindwing Area	125 cm^2	α_L^2	33.4 cm^2
Length	47.5 cm	α_L	27 cm
Tail Area	245 cm^2	α_L^2	55.5 cm^2
Mass	150 — 250 g	α_L^3	16 g

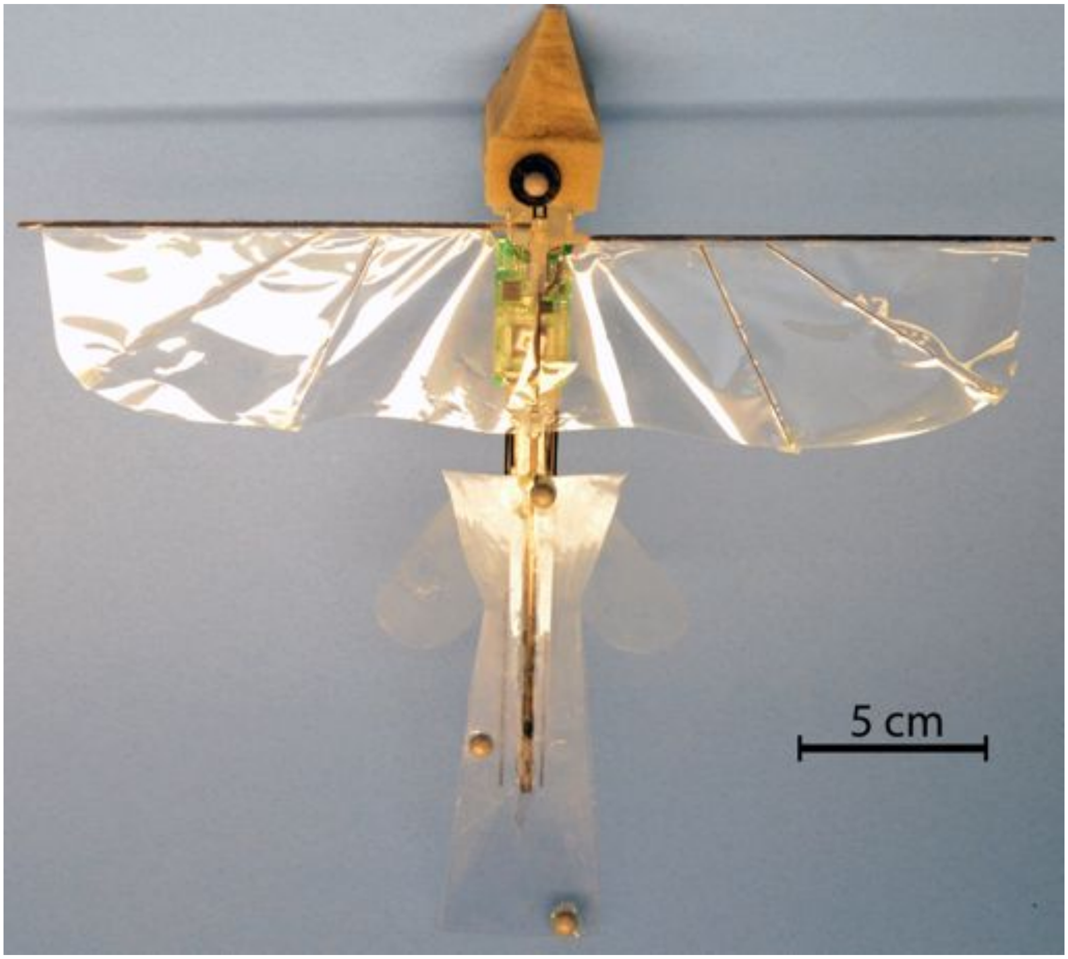

Figure 7.11: Top view of the geometrically scaled *Archaeopteryx* model.

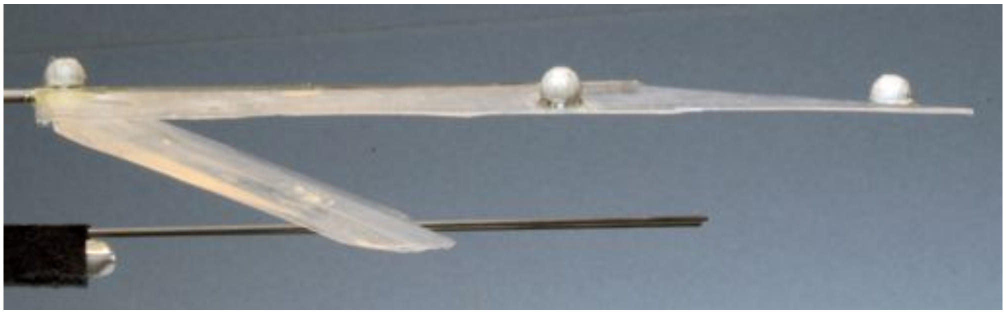

Figure 7.12: Vacuum formed tail and legs for the scaled *Archaeopteryx* model.

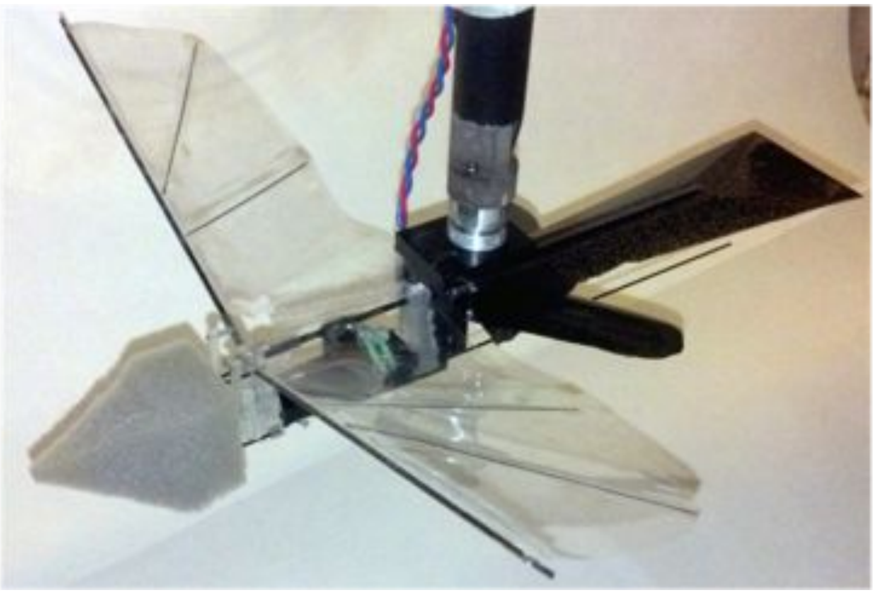

Figure 7.13: Wind tunnel setup. The *Archaeopteryx* model was mounted in a wind tunnel with a force/torque sensor for measuring the lift and drag over variations in wind speed, angle of attack, flapping frequency, and flapping amplitude.

7.3.2 Effect of Flapping Frequency and Amplitude on Performance

Wind Tunnel Experiments

To examine the performance of the model *Archaeopteryx*, we placed the model in a wind tunnel and measured the lift and drag on the system. Figure 7.13 shows the model mounted on a Nano-17 force-torque sensor in a wind tunnel. To examine the performance of the model we vary four different parameters: airspeed, body angle of attack, flapping frequency, and flapping amplitude. In Figure 7.14 and Figure 7.15, the results from the wind tunnel experiments are shown. At lower airspeeds, the flapping wings reduce the drag on the model – creating positive thrust at higher frequencies. Wing flapping also produces higher lift at body angles of attack of 10° and greater.

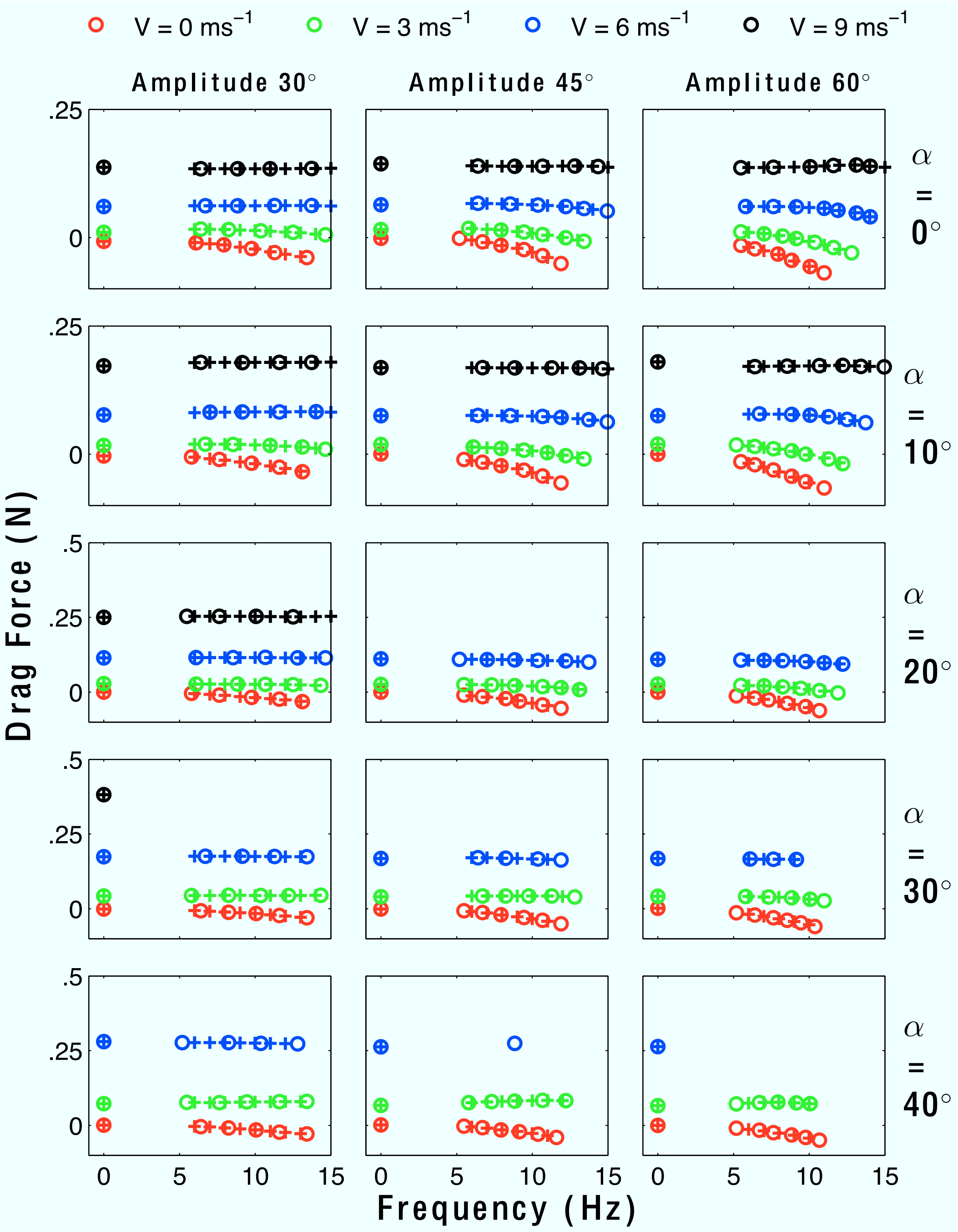

Figure 7.14: Drag forces on the *Archaeopteryx* model measured in a wind tunnel. The circles represent the measured forces from the wind tunnel, while the crosses are evenly-spaced, linearly interpolated values used to generate a model of the forces. Each column shows a different flapping amplitude, with each row a different body angle of attack.

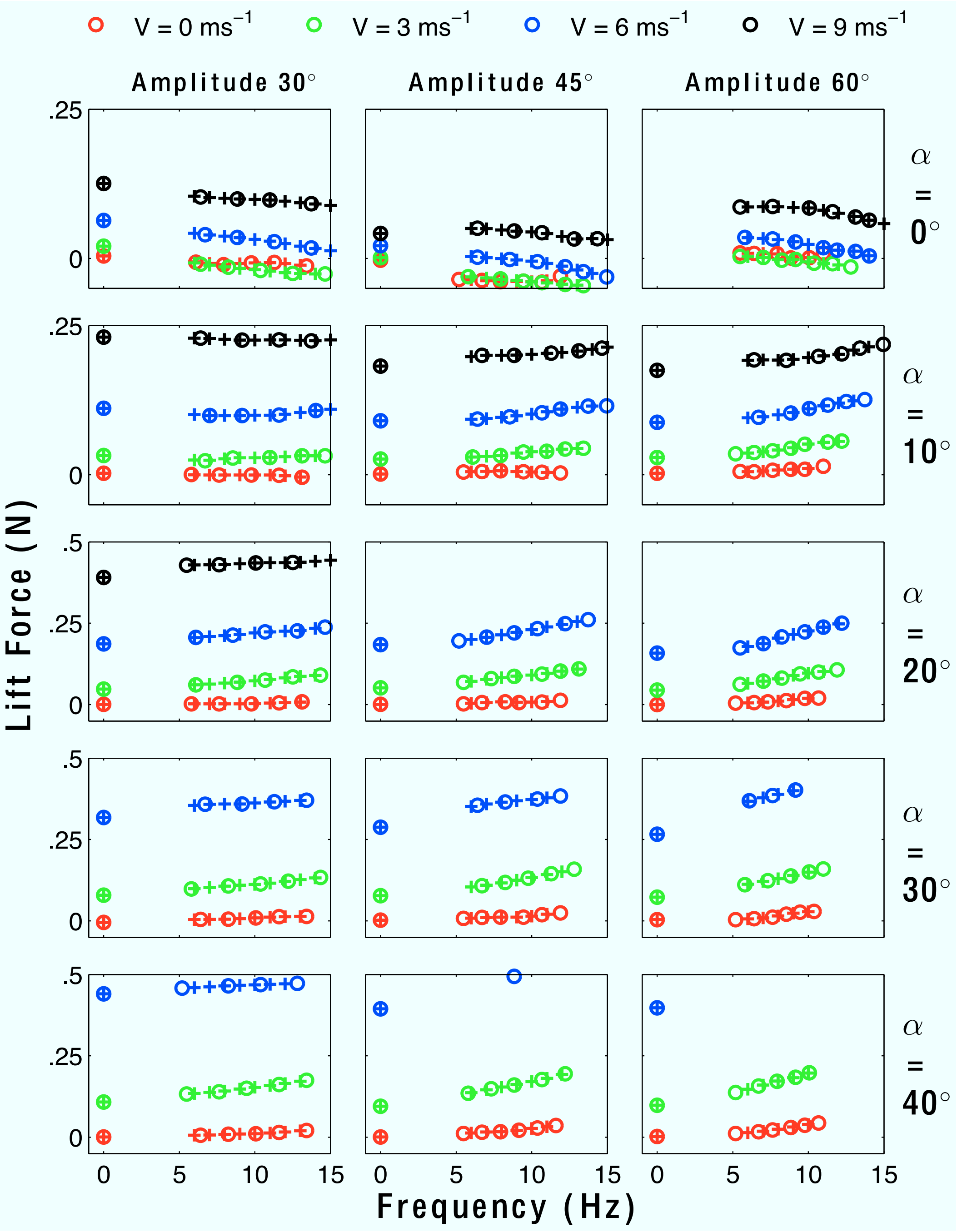

Figure 7.15: Lift forces on the *Archaeopteryx* model measured in a wind tunnel. The circles represent the measured forces from the wind tunnel, while the crosses are evenly-spaced, linearly interpolated values used to generate a model of the forces. Each column shows a different flapping amplitude, with each row a different body angle of attack.

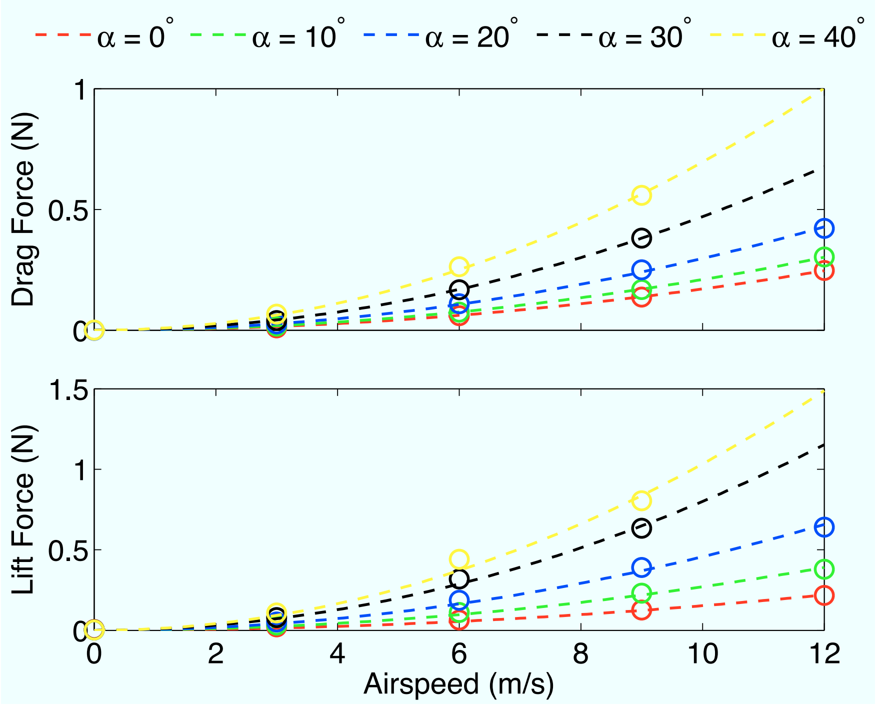

Figure 7.16: Lift and drag forces on the model without flapping. The circles represent the measured values while the lines represent least-squares fit models from Equation 7.5.

As the airspeed, angle of attack, and wing amplitude are increased, the power required by the motor also increases. Eventually the motor reaches a limit and is no longer capable of flapping the wings. All data points up to the limits of the motor are shown. Motor limits also preclude steady flapping at lower frequencies, with the minimum steady motor speed near 5 Hz. Because the motor does not flap at the exact same frequencies across all velocities, angles of attack, and amplitudes, we linearly interpolate to find the intermediate values. This allows the comparison of a single flapping frequency across the other independent parameters.

To examine the performance of the *Archaeopteryx* model, we first examine the steady state case, with no flapping. In this scenario, the forces follow the standard lift and drag equation,

$$F = \frac{1}{2} C \rho A v^2, \tag{7.5}$$

where F is the lift or drag force, C is the lift or drag coefficient, ρ is the density of air, A is the planform area of the model (0.0227 m^2), and v is the airspeed. For each angle of attack, the lift and drag coefficient can be determined using a least-squares fit from the measured force data. Figure 7.16 shows the measured force data along with the model. Comparing the lift to drag ratio at each angle of attack allows the best glide slope to be determined. Table 7.3 and Table 7.4 show the coefficients of drag and lift for each angle of attack. Taking the ratio of lift to drag at each angle of attack, the best glide slope can be found. Without flapping, the best glide slope is 30°at a 30° body angle of attack.

Table 7.3: Drag coefficients and offsets of the *Archaeopteryx* model at selected flapping frequencies, amplitudes, and body angles of attack (α) for Equation 7.5 and Equation 7.6.

		Flapping Amplitude					
		30°		45°		60°	
Frequency (Hz)	α (deg)	F_D^0 (N)	C_D	F_D^0 (N)	C_D	F_D^0 (N)	C_D
0	0	—	0.12	—	0.12	—	—
	10	—	0.15	—	0.15	—	0.16
	20	—	0.21	—	0.22	—	0.22
	30	—	0.34	—	0.33	—	0.34
	40	—	0.51	—	0.53	—	0.53
6	0	-0.0032	0.12	0.0014	0.12	-0.012	0.13
	10	-0.00099	0.16	-0.0082	0.16	-0.01	0.16
	20	-0.0025	0.23	-0.0091	0.24	-0.013	0.24
	30	-0.0038	0.36	-0.0062	0.36	-0.013	0.36
	40	0.0012	0.55	—	—	—	—
8	0	-0.005	0.12	-0.0042	0.12	-0.017	0.13
	10	-0.003	0.16	-0.015	0.17	-0.021	0.18
	20	-0.0057	0.23	-0.015	0.25	-0.025	0.27
	30	-0.0068	0.37	-0.013	0.37	-0.023	0.39
	40	-0.0018	0.56	—	—	—	—
10	0	-0.009	0.12	-0.012	0.13	-0.031	0.14
	10	-0.0064	0.16	-0.024	0.18	-0.037	0.19
	20	-0.0095	0.24	-0.027	0.27	-0.041	0.29
	30	-0.0099	0.37	-0.021	0.38	—	—
	40	-0.005	0.57	—	—	—	—

With the addition of flapping, the standard lift and drag equation no longer adequately describes the force on the model. Because the wing can provide force in the absence of airflow, an additional parameter is necessary in the equation to account for this force offset. With flapping, the forces are now described by

$$F = F^0 + \frac{1}{2}C\rho A v^2, \tag{7.6}$$

where F^0 represents the offset force. The offset force and coefficient can again be found from a least squares fit of the wind tunnel data. Table 7.3 and Table 7.4 show the values of these parameters for drag and lift at multiple flapping frequencies, amplitudes, and body angles of attack. With the flapping wings, a negative drag offset force is observed over frequencies, amplitudes, and angles of attack, implying that the wings are providing positive thrust. In addition, we observe from Table 7.3 that for a given angle of attack, increasing the flapping frequency or amplitude also

Table 7.4: Lift coefficients and offsets of the *Archaeopteryx* model at selected flapping frequencies, amplitudes, and body angles of attack (α) for Equation 7.5 and Equation 7.6.

		Flapping Amplitude					
		30°		45°		60°	
Frequency (Hz)	α (deg)	F_L^0 (N)	C_L	F_L^0 (N)	C_L	F_L^0 (N)	C_L
0	0	—	0.11	—	0.034	—	—
	10	—	0.19	—	0.17	—	0.16
	20	—	0.33	—	0.37	—	0.32
	30	—	0.58	—	0.58	—	0.54
	40	—	0.74	—	0.79	—	0.79
6	0	-0.0098	0.096	-0.032	0.061	0.00076	0.074
	10	0.0031	0.19	0.0069	0.17	0.011	0.16
	20	0.01	0.38	0.012	0.38	0.013	0.34
	30	0.0075	0.69	0.014	0.68	0.014	0.71
	40	0.013	0.9	—	—	—	—
8	0	-0.015	0.097	-0.036	0.064	0.0027	0.059
	10	0.0029	0.19	0.0093	0.17	0.016	0.16
	20	0.014	0.38	0.019	0.4	0.02	0.37
	30	0.011	0.7	0.02	0.69	0.027	0.7
	40	0.018	0.9	—	—	—	—
10	0	-0.017	0.097	-0.039	0.064	-0.0039	0.063
	10	0.0036	0.19	0.012	0.17	0.023	0.16
	20	0.018	0.38	0.02	0.43	0.032	0.4
	30	0.016	0.7	0.028	0.7	—	—
	40	0.024	0.9	—	—	—	—

increases the drag offset force. We also observe positive lift offset forces with the flapping wings (except at $\alpha = 0$), again increasing with flapping frequency and amplitude in Table 7.4.

Using these models, in combination with the equations from subsection 7.2.3, the glide slope can be predicted. Figure 7.17 shows the result of taking the best glide slope across the varying angle of attacks for each flapping frequency and amplitude. This clearly shows the improvement in descent slope with increased flapping frequency and amplitude. With an amplitude of only 30°, the descent slope improves from 30° to 22°. At the higher amplitude of 60°, the slope increases dramatically from 32° to 12°.

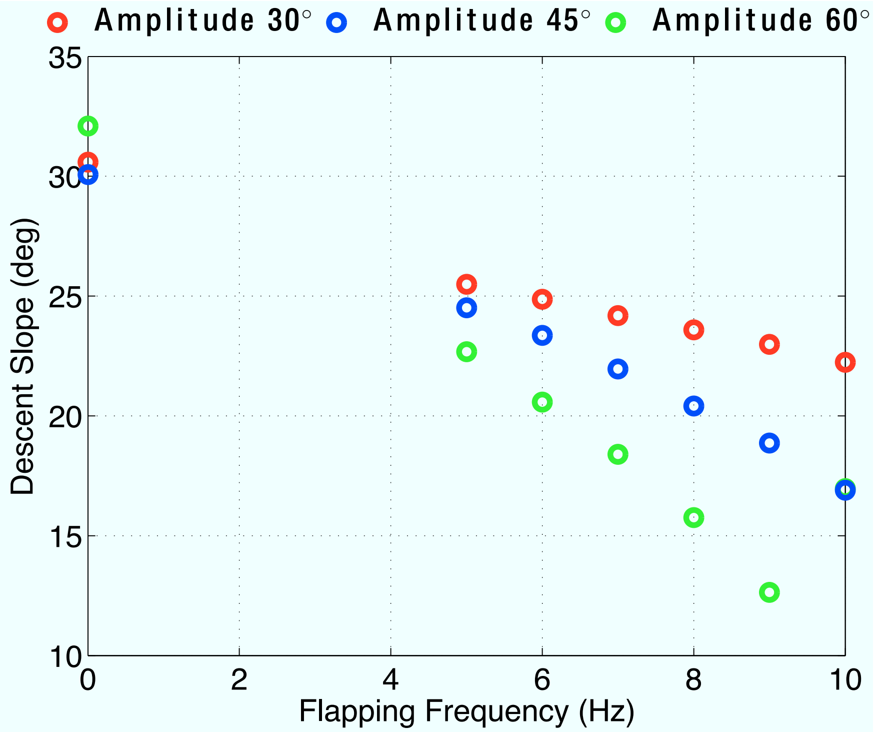

Figure 7.17: Glide slope of the model *Archaeopteryx* as a function of flapping frequency and amplitude.

7.3.3 Discussion of Performance and Implications for Flight Evolution

Our examination of the performance of a scaled *Archaeopteryx* model continue to suggest the utility of flapping wings in an aerial setting. An arboreal dwelling *Archaeopteryx* would derive great benefit from developing flapping, as even the simple kinematics of our scaled model show a dramatic decrease in the descent slope. A key observation from the wind tunnel experiments is the interaction between flapping frequency and amplitude. The glide slope decreases linearly with increasing flapping frequency for each amplitude. However, as the amplitude is increased, the slope of the linear relationship between the flapping frequency and glide slope increases in magnitude. At a higher amplitude, a similar increase in flapping frequency will be more beneficial than the same increase in flapping frequency at a lower amplitude. Similarly, the same applies when increasing the flapping amplitude. At a higher flapping frequency, more benefit is derived from increasing the flapping amplitude than at lower frequencies. This suggests a biomechanical reason for co-evolution of the flapping frequency and flapping amplitude, with each increasing simultaneously.

Chapter 8

Conclusion

This work has explored hybrid legged and winged robots at the meso-scale. The design of two hybrid robots was presented, each with its own abilities. Our initial hybrid robot, DASH+Wings, provided many key insights into hybrid locomotion, and was instrumental in enabling the design of BOLT. DASH+Wings also provided a novel platform for investigating theories on avian flight evolution. Through evaluation of the capabilities of DASH+Wings, we examined the biomechanical likelihood that flight evolved from either a cursorial or arboreal environment. While the flapping wings provided utility during both aerial and terrestrial modes of locomotion, they fell short of the performance increase predicted necessary for the cursorial takeoff of a ground-dwelling avian precursor. We further investigated the aerial performance of a scaled model for *Archaeopteryx*, and showed the utility of increased flapping frequency and amplitude for improving force production towards improved gliding and eventual sustained flight. Taken in context with new fossil discoveries suggesting a four-winged phase for early birds, these experiments suggest that flight likely evolved in an arboreal context.

Our second hybrid robot, BOLT, achieved the goal of being capable of both aerial and terrestrial locomotion, and transitioning between the two in an indoor environment. During dynamic running, BOLT uses a unique method for maintaining passively stable bipedal locomotion, exploiting the aerodynamic effects of its flapping wings. Because of the aerodynamic forces present on the robot, BOLT does not run using a traditional SLIP gait. Despite this fact, the robot is capable of high speed locomotion, "flying" along the ground using a combination of aerodynamic forces and ground reaction forces to propel itself. This mode of locomotion was elucidated through the development of WingSLIP, a hybrid dynamic model incorporating both leg and wing forces. With the addition of wing forces, the legs function mainly as supports keeping the hips off the ground and allowing the wings to propel the system across the ground.

The integration of both legs and wings into the BOLT platform enable a highly capable mobile robot in many environments. The robot is capable of self-righting, and climbing vertical inclines at 0.6 ms^{-1} through the use of magnetic feet. The legs and wings hybrid configuration is also particularly adept at crossing low obstacles placed in its path without needing to resort to aerial locomotion. While not the first hybrid aerial/terrestrial robot, BOLT is currently the smallest. Its ability to transition from terrestrial locomotion to aerial locomotion in a small space enables it to take advantage of both modes of transportation, especially in a confined environment. The key contribution setting BOLT apart is the integration of a smart electronics package capable of measuring the dynamics of a fully capable hybrid platform. BOLT has begun to provide insights into the dynamics of wing assisted locomotion, and allows the interactions between legs and wings to be examined.

8.1 Future Work

While this thesis has explored the capabilities of hybrid robots, there are still many rich questions on the interaction of legs and wings where this concept can be extended further. The use of hybrid robots shows great potential in both expanding the utility of small mobile robots as well as further investigating the theories of avian flight evolution.

8.1.1 Hybrid locomotion

While BOLT utilizes its legs and flapping wings to enable a variety of novel locomotion abilities, its use in terrestrial locomotion is limited by its high cost of transport. Further analysis of the WingSLIP model alongside BOLT can investigate ways to improve the performance while also increasing the efficiency of the system as well. Additionally, a transmission capable of selectively driving the legs or wings would allow further improvement to the efficiency of the robot. By turning off the wings at low terrestrial speeds, or disengaging the legs when flying, the robot can minimize the power lost to unnecessary appendages.

From a biologically inspired perspective, flapping wings allow remarkable maneuverability in insects and birds through within-wingbeat adjustments and among-wingbeat variations. Using flapping wings enables scaling and increased maneuverability of future robots, as biological understanding increases and actuator technologies advance. Future work will harness these advancements to create flying and crawling platforms that begin to push the boundaries seen in the locomotion abilities of animals.

8.1.2 Avian Flight Evolution

DASH+Wings showed the power of using a small legged and winged robot to investigate theories on avian flight evolution in a biomechanical context. While not morphologically correct, the platform was capable of directly evaluating the consequences of adding wings to a cursorial platform in both aerial and terrestrial modes of locomotion. Our scaled *Archaeopteryx* model enabled the investigation of the aerial benefits of increased flapping frequency and amplitude on a morphologically correct platform. The cursorial benefits on this platform remain unknown. The addition of lightweight legs, similar to those used for BOLT, can enable a comprehensive investigation of the utility of flapping wings in an early avian precursor.

Bibliography

[1] (2011). [Online]. Available: http://www.avinc.com/nano

[2] D. E. Alexander, E. Gong, L. D. Martin, D. A. Burnham, and A. R. Falk, “Model tests of gliding with different hindwing configurations in the four-winged dromaeosaurid microraptor gui,” *Proceedings of the National Academy of Sciences*, vol. 107, no. 7, pp. 2972–2976, 2010.

[3] ——, “Model tests of gliding with different hindwing configurations in the four-winged dromaeosaurid microraptor gui,” *Proceedings of the National Academy of Sciences*, vol. 107, no. 7, pp. 2972–2976, 2010. [Online]. Available: http://www.pnas.org/content/107/7/2972.abstract

[4] R. J. Bachmann, F. J. Boria, R. Vaidyanathan, P. G. Ifju, and R. D. Quinn, “A biologically inspired micro-vehicle capable of aerial and terrestrial locomotion,” *Mechanism and Machine Theory*, vol. 44, no. 3, pp. 513 – 526, 2009, special issue on Bio-Inspired Mechanism Engineering.

[5] S. Baek, F. G. Bermudez, and R. Fearing, “Flight control for target seeking by 13 gram ornithopter,” in *IEEE International Conference on Intelligent RObots and Systems(IROS)*, September 2011.

[6] P. Birkmeyer, K. Peterson, and R. Fearing, “DASH: A dynamic 16g hexapedal robot,” in *IEEE/RSJ International Conference on Intelligent Robots and Systems*, October 2009, pp. 2683–2689.

[7] R. Blickhan and R. J. Full, “Similarity in multilegged locomotion: Bouncing like a monopode,” *Journal of Comparative Physiology A: Neuroethology, Sensory, Neural, and Behavioral Physiology*, vol. 173, no. 5, pp. 509–517, November 1993.

[8] F. Boria, R. Bachmann, P. Ifju, R. Quinn, R. Vaidyanathan, C. Perry, and J. Wagener, “A sensor platform capable of aerial and terrestrial locomotion,” in *IEEE/RSJ International Conference on Intelligent Robots and Systems*, August 2005, pp. 3959–3964.

[9] I. E. Brown and G. E. Loeb, “A reductionist approach to creating and using neuromusculoskeletal models,” in *Biomechanics and neural control of posture and movement*, J. M. Winters and P. E. Crago, Eds. New York: Springer, 2000.

[10] M. Bundle and K. Dial, “Mechanics of wing-assisted incline running (WAIR),” *Journal of Experimental Biology*, vol. 206, no. 24, pp. 4553–4564, 2003.

[11] S. Burden, J. E. Clark, J. Weingarten, H. Komsuoglu, and D. E. Koditschek, “Heterogeneous Leg Stiffness and Roll in Dynamic Running,” *IEEE Int.Conf. on Robotics and Automation*, pp. 4645–4652, Apr. 2007.

[12] P. Burgers and L. M. Chiappe, “The wing of archaeopteryx as a primary thrust generator,” *Nature*, vol. 399, no. 6731, pp. 60–62, 1999.

[13] J. G. Cham, S. A. Bailey, J. E. Clark, R. J. Full, and M. R. Cutkosky, “Fast and robust: Hexapedal robots via shape deposition manufacturing,” *International Journal of Robotics Research*, vol. 21, no. 10, 2002.

[14] K. P. Dial, B. E. Jackson, and P. Segre, “A fundamental avian wing-stroke provides a new perspective on the evolution of flight,” *Nature*, vol. 451, no. 7181, pp. 985–989, 2008.

[15] K. P. Dial, R. J. Randall, and T. R. Dial, “What use is half a wing in the ecology and evolution of birds?” *BioScience*, vol. 56, no. 5, pp. 437–445, 2006.

[16] R. Dudley, G. Byrnes, S. P. Yanoviak, B. Borrell, R. M. Brown, and J. A. McGuire, “Gliding and the functional origins of flight: biomechanical novelty or necessity?” *Annu. Rev. Ecol. Evol. Syst.*, vol. 38, pp. 179–201, 2007.

[17] I. Faruque and J. Sean Humbert, “Dipteran insect flight dynamics. part 1 longitudinal motion about hover,” *Journal of Theoretical Biology*, vol. 264, no. 2, pp. 538–552, 2010.

[18] A. Feduccia, “Evidence from claw geometry indicating arboreal habits of archaeopteryx,” *Science*, vol. 259, no. 5096, pp. 790–793, 1993.

[19] R. Full and M. Tu, “Mechanics of rapid running insects: two-, four-, and six-legged locomotion,” *Journal of Experimental Biology*, vol. 156, pp. 215–231, 1991.

[20] R. J. Full and D. E. Koditschek, “Templates and anchors: neuromechanical hypotheses of legged locomotion on land,” *Journal of Experimental Biology*, vol. 202, no. 23, pp. 3325–3332, 1999.

[21] C. Georgiades, A. German, A. Hogue, H. Liu, C. Prahacs, A. Ripsman, R. Sim, L. Torres, P. Zhang, M. Buehler *et al.*, “AQUA: an aquatic walking robot,” in *IEEE/RSJ International Conference on Intelligent Robots and Systems*, vol. 4, September 2004, pp. 3525–3531.

[22] D. Haldane, K. Peterson, F. Bermudez, and R. Fearing, “Animal-inspired design and aerodynamic stabilization of a hexapedal millirobot,” in *IEEE Int. Conf. on Robotics and Automation*, May 2013.

[23] J. Harshman, E. L. Braun, M. J. Braun, C. J. Huddleston, R. C. Bowie, J. L. Chojnowski, S. J. Hackett, K.-L. Han, R. T. Kimball, B. D. Marks *et al.*, "Phylogenomic evidence for multiple losses of flight in ratite birds," *Proceedings of the National Academy of Sciences*, vol. 105, no. 36, pp. 13 462–13 467, 2008.

[24] P. Holmes, R. J. Full, D. Koditschek, and J. Guckenheimer, "The dynamics of legged locomotion: Models, analyses, and challenges," *SIAM Review*, vol. 48, no. 2, pp. 207–304, 2006.

[25] A. Hoover, S. Burden, X. Fu, S. Sastry, and R. Fearing, "Bio-inspired design and dynamic maneuverability of a minimally actuated six-legged robot," in *3rd IEEE RAS and EMBS International Conference on Biomedical Robotics and Biomechatronics (BioRob)*, September 2010, pp. 869–876.

[26] A. Hoover and R. Fearing, "Fast scale prototyping for folded millirobots," *IEEE International Conference on Robotics and Automation*, pp. 886–892, May 2008.

[27] D. Hu, L. Hou, L. Zhang, and X. Xu, "A pre-archaeopteryx troodontid theropod from china with long feathers on the metatarsus," *Nature*, vol. 461, no. 7264, pp. 640–643, 2009.

[28] B. E. Jackson, P. Segre, and K. P. Dial, "Precocial development of locomotor performance in a ground-dwelling bird (alectoris chukar): negotiating a three-dimensional terrestrial environment," *Proceedings of the Royal Society B: Biological Sciences*, vol. 276, no. 1672, pp. 3457–3466, 2009.

[29] B. E. Jackson, B. W. Tobalske, and K. P. Dial, "The broad range of contractile behaviour of the avian pectoralis: functional and evolutionary implications," *The Journal of Experimental Biology*, vol. 214, no. 14, pp. 2354–2361, 2011. [Online]. Available: http://jeb.biologists.org/content/214/14/2354.abstract

[30] A. Jusufi, D. Kawano, T. Libby, and R. Full, "Righting and turning in mid-air using appendage inertia: reptile tails, analytical models and bio-inspired robots," *Bioinspiration & biomimetics*, vol. 5, no. 4, p. 045001, 2010.

[31] S. Kim, J. E. Clark, and M. R. Cutkosky, "isprawl: Design and tuning for high-speed autonomous open-loop running," *International Journal of Robotics Research*, vol. 25, no. 9, pp. 903–912, 2006.

[32] M. A. R. Koehl, D. Evangelista, and K. Yang, "Using physical models to study the gliding performance of extinct animals," *Integrative and Comparative Biology*, vol. 51, no. 6, pp. 1002–1018, 2011. [Online]. Available: http://icb.oxfordjournals.org/content/51/6/1002.abstract

[33] N. Kohut, A. Pullin, D. Haldane, D. Zarrouk, and R. Fearing, "Precise dynamic turning of a 10 cm legged robot on a low friction surface using a tail," in *IEEE Int. Conf. on Robotics and Automation*, 2013.

[34] M. Kovac, J. Zufferey, and D. Floreano, “Towards a self-deploying and gliding robot,” *Flying Insects and Robots*, 2009.

[35] M. Kovaç, J. Germann, C. Hrzeler, R. Siegwart, and D. Floreano, “A perching mechanism for micro aerial vehicles,” *Journal of Micro-Nano Mechatronics*, vol. 5, pp. 77–91, 2009.

[36] D. Lachat, A. Crespi, and A. Ijspeert, “Boxybot: a swimming and crawling fish robot controlled by a central pattern generator,” in *The First IEEE/RAS-EMBS International Conference on Biomedical Robotics and Biomechatronics (BioRob)*, February 2006, pp. 643–648.

[37] D. Lentink, S. Jongerius, and N. Bradshaw, “The scalable design of flapping micro-air vehicles inspired by insect flight,” *Flying Insects and Robots*, p. 185, 2009.

[38] T. Libby, T. Y. Moore, E. Chang-Siu, D. Li, D. J. Cohen, A. Jusufi, and R. J. Full, “Tail-assisted pitch control in lizards, robots and dinosaurs,” *Nature*, vol. 481, no. 7380, pp. 181–184, 2012.

[39] N. Longrich, “Structure and function of hindlimb feathers in archaeopteryx lithographica,” *Paleobiology*, vol. 32, no. 3, pp. 417–431, 2013/04/22 2006. [Online]. Available: http://www.psjournals.org/doi/abs/10.1666/04014.1

[40] J. R. Lovvorn, “Upstroke thrust, drag effects, and stroke-glide cycles in wing-propelled swimming by birds,” *American Zoologist*, vol. 41, no. 2, pp. 154–165, 2001. [Online]. Available: http://icb.oxfordjournals.org/content/41/2/154.abstract

[41] A. Lussier Desbiens, A. Asbeck, and M. Cutkosky, “Landing, perching and taking off from vertical surfaces,” *The International Journal of Robotics Research*, vol. 30, no. 3, p. 355, 2011.

[42] R. D. Maladen, Y. Ding, C. Li, and D. I. Goldman, “Undulatory swimming in sand: subsurface locomotion of the sandfish lizard,” *Science*, vol. 325, no. 5938, pp. 314–318, 2009.

[43] O. C. Marsh, *Odontornithes: a monograph of the extinct toothed birds of North America*. Government printing office, 1880.

[44] A. M. Mehta and K. S. Pister, “Warpwing: A complete open source control platform for miniature robots,” in *Intelligent Robots and Systems (IROS), 2010 IEEE/RSJ International Conference on*. IEEE, 2010, pp. 5169–5174.

[45] J. M. Morrey, B. Lambrecht, A. D. Horchler, R. E. Ritzmann, and R. D. Quinn, “Highly mobile and robust small quadruped robot,” in *IEEE/RSJ International Conference on Intelligent Robots and Systems*, October 2003, pp. 82–87.

[46] N. Neville, M. Buehler, and I. Sharf, “A bipedal running robot with one actuator per leg,” in *IEEE International Conference on Robotics and Automation*, May 2006, pp. 848 –853.

[47] B. F. Nopcsa, "On the origin of flight in birds," in *Proceedings of the Zoological Society of London*, vol. 93, no. 2. Wiley Online Library, 1923, pp. 463–477.

[48] F. Nopcsa, "Ideas on the origin of flight," in *Proceedings of the Zoological Society of London*, 1907, pp. 223–236.

[49] R. L. Nudds and G. J. Dyke, "Forelimb posture in dinosaurs and the evolution of the avian flapping flight-stroke," *Evolution*, vol. 63, no. 4, pp. 994–1002, 2009.

[50] ——, "Narrow primary feather rachises in confuciusornis and archaeopteryx suggest poor flight ability," *Science*, vol. 328, no. 5980, pp. 887–889, 2010.

[51] J. Ostrom, "Some hypothetical anatomical stages in the evolution of avian flight," *Smithsonian Contributions to Paleobiology*, vol. 27, pp. 1–21, 1976.

[52] J. H. Ostrom, "Archaeopteryx and the origin of birds," *Biological Journal of the Linnean Society*, vol. 8, no. 2, pp. 91–182, 1976.

[53] K. Padian and L. M. Chiappe, "The origin and early evolution of birds," *Biological Reviews*, vol. 73, no. 1, pp. 1–42, 1998.

[54] D. S. Peters and E. Görgner, "A comparative study on the claws of archaeopteryx," *Papers in avian paleontology. Honoring Pierce Brodkorb*, vol. 36, pp. 29–37, 1992.

[55] K. Peterson, P. Birkmeyer, R. Dudley, and R. Fearing, "A wing-assisted running robot and implications for avian flight evolution," *Bioinspiration & Biomimetics*, vol. 6, no. 4, p. 046008, 2011.

[56] K. Peterson and R. S. Fearing, "Experimental dynamics of wing assisted running for a bipedal ornithopter," in *IEEE/RSJ International Conference on Intelligent Robots and Systems (IROS), 2011.* IEEE, 2011, pp. 5080–5086.

[57] K. C. Peterson, "Running with flapping wings," Master's thesis, University of California, Berkeley, 2010.

[58] J. Ruben, "Paleobiology and the origins of avian flight," *Proceedings of the National Academy of Sciences*, vol. 107, no. 7, pp. 2733–2734, 2010.

[59] U. Saranli, M. Buehler, and D. E. Koditschek, "Rhex: A simple and highly mobile hexapod robot," *International Journal of Robotics Research*, vol. 20, no. 7, pp. 616 – 631, July 2001.

[60] A. Sato and M. Buehler, "A planar hopping robot with one actuator: design, simulation, and experimental results," in *Intelligent Robots and Systems, 2004. (IROS 2004). Proceedings. 2004 IEEE/RSJ International Conference on*, vol. 4, Sept.-2 Oct., pp. 3540–3545 vol.4.

[61] P. J. Schaeffer and S. L. Lindstedt, "How animals move: Comparative lessons on animal locomotion," *Comprehensive Physiology*.

[62] J. Seipel and P. Holmes, “A simple model for clock-actuated legged locomotion,” *Regular and chaotic dynamics*, vol. 12, no. 5, pp. 502–520, 2007.

[63] ——, “Three-dimensional translational dynamics and stability of multi-legged runners,” *The International Journal of Robotics Research*, vol. 25, no. 9, pp. 889–902, 2006. [Online]. Available: http://ijr.sagepub.com/content/25/9/889.abstract

[64] A. J. Spence, S. Revzen, J. Seipel, C. Mullens, and R. J. Full, “Insects running on elastic surfaces,” *The Journal of Experimental Biology*, vol. 213, no. 11, pp. 1907–1920, 2010.

[65] B. W. Tobalske and K. P. Dial, “Aerodynamics of wing-assisted incline running in birds,” *Journal of Experimental Biology*, vol. 210, no. 10, pp. 1742–1751, 2007.

[66] S. Williston, “Are birds derived from dinosaurs,” *Kansas City Review of Science*, vol. 3, pp. 457–460, 1879.

[67] R. Wood, S. Avadhanula, R. Sahai, E. Steltz, and R. Fearing, “Microrobot design using fiber reinforced composites,” *Journal of Mechanical Design*, vol. 130, p. 052304, 2008.

[68] X. Xu, Z. Zhou, and X. Wang, “The smallest known non-avian theropod dinosaur,” *Nature*, vol. 408, no. 6813, pp. 705–708, 2000.

[69] X. Xu, Z. Zhou, X. Wang, X. Kuang, F. Zhang, and X. Du, “Four-winged dinosaurs from china,” *Nature*, vol. 421, no. 6921, pp. 335–340, 2003.

[70] D. Yalden, “The flying ability of archaeopteryx,” *Ibis*, vol. 113, no. 3, pp. 349–356, 1971.

[71] ——, “Forelimb function in archaeopteryx,” *The beginnings of birds, Eichstätt: Freunde des Jura-Museums Eichstätt*, pp. 91–97, 1985.

[72] ——, “Climbing archaeopteryx,” *Archaeopteryx*, vol. 15, pp. 107–108, 1997.

[73] D. Zarrouk and R. S. Fearing, “Compliance-based dynamic steering for hexapods,” in *Intelligent Robots and Systems (IROS), 2012 IEEE/RSJ International Conference on*. IEEE, 2012, pp. 3093–3098.